Microphysical Properties of Dynamically Forced Cirrus Associated with Strong Jet Streams and Their Relation to the Synoptic Scale Flow

By
John M. Haynes and Graeme L. Stephens

Department of Atmospheric Science
Colorado State University
Fort Collins, Colorado

Research supported by DOE grant DE-FG03-94ER61748, and NASA grant NAS5-99237.
PI: G. Stephens

Colorado State University

Department of Atmospheric Science

Paper No. 722

MICROPHYSICAL PROPERTIES OF DYNAMICALLY FORCED CIRRUS ASSOCIATED WITH STRONG JET STREAMS AND THEIR RELATION TO THE SYNOPTIC SCALE FLOW

John M. Haynes and Graeme L. Stephens

Research supported by Department of Energy
Grant #DE-FG03-94ER61748,
NASA Grant NAS5-99237

Principal Investigator: Graeme L. Stephens

Department of Atmospheric Science

Colorado State University

Fort Collins, CO

March, 2002

Atmospheric Science Paper No. 722

ABSTRACT

MICROPHYSICAL PROPERTIES OF DYNAMICALLY FORCED CIRRUS ASSOCIATED WITH STRONG JET STREAMS AND THEIR RELATION TO THE SYNOPTIC SCALE FLOW

Cirrus are known to play an important role in the radiative budget of the earth-atmosphere system, yet the connection between the properties of mid-latitude cirrus clouds and the large scale flow that supports them is still to a large degree unknown. This study seeks to better quantify and understand this relationship through two interrelated investigations.

First, a composite was performed over fourteen cases of strong jet streams that occurred over the eastern United States, relative to the location of maximum 300 hPa wind within the jet. The composite consisted of both a dynamical composite of ECMWF reanalysis data and a cloud composite of ISCCP-derived parameters. The dynamical composite revealed many familiar synoptic-scale features, including upward vertical motion that was maximized in the right-entrance and left-exit region of the jet.

The cloud composite showed the greatest cirrus coverage in the accelerating region of the jet. Other regions with cirrus were located above the comma cloud and another just to its southeast, featuring a sharp northern boundary aligned with the jet axis. Sporadic cirrus coverage was located in the warm air in advance of the surface front. ECMWF-derived vertical motion at cloud-level was weakly ascending in the comma region, but near neutral or weakly subsiding on the order of 0.1 Pa s^{-1} in the other regions.

In the second portion of the study, a relatively new radar retrieval algorithm that is set in an optimal estimation framework was applied to six case studies of jet stream cirrus over the ARM site in Oklahoma. This retrieval used vertical profiles of radar reflectivity and cloud optical depth to retrieve ice particle effective radius, size distribution, and ice water content within these clouds.

While the retrieved microphysical properties of these clouds varied greatly (for example, time-averaged ice water path varied between 3.2 and 44.9 g m^{-2}), mean vertical motion assessed by the ETA/EDAS model was uniformly weak at cloud level, varying from -0.20 to 0.10 Pa s^{-1}, and just as often ascending as descending. It is concluded that the small scale motions responsible for the growth and decay of these clouds are not currently easily resolved in numerical models, and synoptic scale motions within the jet are not alone sufficient to explain the occurrence and distribution of jet stream cirrus.

John M. Haynes
Department of Atmospheric Science
Colorado State University
Fort Collins, CO 80523
Spring 2002

ACKNOWLEDGEMENTS

There are several people who deserve thanks and acknowledgement for helping to make this work possible. My advisor, Graeme Stephens, provided great assistance in steering me toward a relevant topic and providing direction and guidance throughout the research and writing process. I also with to thank my committee, William Cotton and Chiao-Yao She, for their input and review of the thesis.

Several of my colleagues in the department provided invaluable assitance in completion of this research. Much thanks goes to Angela Benedetti for sharing the work she had done with the radar algorithm that is used in this study, and for much useful advice and support. The rest of the Stephens group also contributed to this work in some part through many useful discussions over the last two years. I wish to thank Quilong Min and Dave Turner for providing optical depth estimates, and Alice Cialella for spending so much time debugging the ETA/EDAS datasets.

This page intentionally blank.

CONTENTS

LIST OF FIGURES

LIST OF TABLES

Chapter 1

1. INTRODUCTION

1.1 Cirrus and their Significance

Cirrus clouds are known to be of critical importance in the radiative budget of the atmosphere. Realization of the radiative importance of these clouds, however, eluded scientists until the mid-to-late twentieth century. The importance of these clouds has only recently been acknowledged by the scientific community. Traditionally, cirrus were for the most part seen as dull and insignificant since they were located so far above the earth's surface, and rarely directly associated with the type of inclement weather that would command the attention of people. They garnered the attention only of observant weather forecasters and shipping merchants, who noted that the appearance of a layer of cirrus often preceded the arrival of a surface storm system.

Today, the reason for this correlation is known; mid-latitude cirrus are often associated with jet streams, or fast moving currents of air found in the upper troposphere. The cirrus clouds associated with jet streams are often observed to have a sharp northern boundary, as is shown in the infrared satellite image of Figure 1-1. This boundary is often found to be coincident with the axis of maximum winds at jet level (Figure 1-2).

Previous studies have noted the tendency of strong jet streams to contain large expanses of cirrus. Menzel et al. (1992) found that in the winter months, when jet winds are typically strongest, 40% to 60% of the cirrus found over the continental United States were located in the jet stream. In the summer months when jet winds are weaker, this figure reduced to 6% to 29% (Table 1-1).

Season	Fraction of CONUS under jet (%)	Fraction of cirrus in jet (%)	Fraction of CONUS under cirrus (%)
Winter			
January–February 1986	42	40	29
January 1988	51	60	28
Spring			
April 1986	46	47	26
April 1988	60	58	26
Summer			
July 1986	13	13	26
July 1987	15	14	25
July 1988	23	29	23
July 1988	8	12	25
Fall			
October 1986	5	6	23
October 1987	48	55	24

Table 1-1: Fraction of satellite-observed cirrus within jet stream. From Menzel et al. (1992).

These jet stream cirrus clouds are not typically associated with precipitation; in fact, they often occur with no underlying cloud deck. Menzel et al. found that the occurrence of cirrus in January over the continental U.S. was approximately the same as in June, but only about one-fifth of these cirrus were associated with precipitating convection in the winter, compared to one-half in the summer. It can therefore be inferred that the processes responsible for cirrus near a strong jet stream are probably different from those responsible for summertime cirrus. Much of the cirrus that occurs in the summer over the U.S. is associated with high-level detrainment from convection. The

wintertime cirrus are more closely associated with the jet and the strong dynamical processes that accompany it.

1.2 Motivation for the Study

Relatively little work has been done in the investigation of the relationship between mid-latitude cirrus properties and the synoptic scale features they are associated with. This is the case despite our current knowledge of the radiative importance of cirrus clouds, and the fact that these radiative properties are determined by the microphysical properties. Though these clouds can be optically thin, and at times sub-visible from both the surface and satellite observing platforms, they occur in the upper troposphere at some of the lowest temperatures found anywhere in the Earth's atmosphere. This means that they radiate at relatively cold temperatures, and therefore act to reduce the net radiation leaving the top of the atmosphere. Put another way, cirrus are associated with radiative flux convergence in the atmosphere; they lead to a net warming of the troposphere (Stephens 1994).

Clearly, cirrus are an essential component of the atmosphere's radiative budget and therefore closely linked to the Earth's hydrologic cycle and everyday weather. Correctly diagnosing these clouds is essential for both the numerical weather prediction models that produce short-term weather forecasts and the global climate models that predict the state of the atmosphere years into the future. Unfortunately, cirrus are some of the most difficult cloud-types to predict using numerical models (Wylie, 2002). This is because the dynamics that support them are weak, and verification of the microphysical content of these clouds is sparse.

This study seeks to gain a better understanding of jet stream cirrus clouds and their location and properties relative to synoptic-scale jet stream features. It also seeks to quantify some of the microphysical properties of these clouds, such as ice particle size distribution, number concentration, and ice water content. The research goal is to contribute to the community's knowledge of cirrus associated with strong jet streams and the characteristics of these clouds.

1.3 Jet Streak Dynamical Background

A jet streak is a localized region of maximum wind that propagates through a larger jet stream. They are associated with both strong vertical and horizontal shear. The classical model of motions within jet streaks is described by Uccellini and Johnson (1979), who describe the importance of ageostrophic motions in generating circulations within the accelerating and decelerating regions of the jet streak. As a simplified but useful example, consider the inviscid zonal momentum equation evaluated on an f-plane, with a Coriolis parameter of f_0. The time rate of change of the zonal geostrophic wind, u_g, is related to the meridional ageostrophic wind, v_{ag}, by:

$$\frac{Du_g}{Dt} = f_0 v_{ag} \tag{1.1}$$

Therefore, westerly wind accelerating into the jet stream requires southerly ageostrophic flow, and wind decelerating in the jet exit region requires northerly ageostrophic flow. This is depicted schematically in Figure 1-3. Air parcels entering the jet experience a sudden increase in the pressure gradient force, while the Coriolis force acts on longer timescales and thus remains relatively constant. This deflects parcels to

the left of their original path. Similarly, air parcels exiting the jet experience a sudden decrease in the pressure gradient force, and are deflected to the right by the stronger Coriolis force. This sets up two ageostrophic circulations, one that is thermally direct in the jet entrance region and one that is thermally indirect in the jet exit region. The resulting mid-level upward motion occurs in the right entrance region and left exit region of the jet streak.

Given the strong shear and ageostrophic motions surrounding the jet streak, it is not surprising that a wide variety of wave phenomenon are also associated with vertical motion in the jet. Ciesielski et al. (1989) sited the possibilities that gravity waves, barotropic instabilities, and inertial instabilities may lead to vertical motion in the vicinity of jet streaks. Vertical shear can lead to Kelvin-Helmholz instabilities and neutrally propagating internal gravity waves. Gravity waves are also produced in the geostrophic adjustment process, which is constantly at work when ageostrophic motions are present; the energy carried in these waves acts to bring the large-scale flow back toward geostrophic balance.

Barotropic instabilities can develop in areas of horizontal shear when the gradient of absolute vorticity in the mean flow goes to zero, as can sometimes be observed within jets. Inertial instabilities occur when the absolute vorticity of the flow is less than zero, which is most common on the anticyclonic side of the jet stream. Ciesielski et al. (1989) demonstrated that inertial instability can lead to formation of cirrus "wavelets" that propagate through the flow; in the case that was studied, the wavelets appeared in the right-entrance region of the jet streak but very near the jet streak core. Inertial instabilities act to reduce the shear and bring the absolute vorticity back toward zero.

With all these dynamical processes acting to produce vertical motions, locating areas of ascent that may be associated with cirrus within a jet system is not trivial. Durran and Weber (1988) suggested that the sharp poleward boundary that is often observed with jet stream cirrus is caused by horizontal gradients of moisture. Their modeling study suggested that differential vertical motions within the jet streak act to concentrate the humidity gradient near the jet core. This humidity front then experiences a relatively uniform lifting, leading to cirrus formation in the more humid air to the south of the jet axis. One goal of this study is to quantify the vertical motion within various parts of the jet, and determine to what extent this corresponds to the observed location of cirrus.

1.4 Nature of the Study and Principle Findings

This study is divided into two parts, a composite study of the dynamical and cloud features associated with strong jet streams, and six case studies of jet stream cirrus clouds that occurred over northern Oklahoma during 1998 and 1999.

Chapter 2 introduces a composite study that seeks to place the location of these clouds relative to the relevant dynamics. A composite of dynamical and cloud fields was performed over the location of the maximum 300 hPa wind in several independent cases of strong wintertime jet streams over the eastern United States. This follows the general technique used in a study of synoptic-scale cloud systems by Lau and Crane (1995). However, the application of this technique relative to the polar jet stream structure is new, and the findings add to the currently slim body of knowledge concerning the relation of mid-latitude cirrus to the dynamical structures that support them. In

particular, it was found that the primary cirrus coverage in the system was in the accelerating region of the jet, with another areas of high and cold but thicker cirrus-like clouds in the right-exit region of the jet. Vertical motion assessed in these regions was always found to be weak at cloud level, but the sign of the vertical motion depended on position within the jet.

Chapter 3 and 4 introduce a radar-based retrieval that is set in an optimal estimation framework as described by Rogers (1976, 1990). Retrieval of cloud properties via active sensors is common, but fashioning the problem in terms of optimum estimation is something fairly new to the radar community. An algorithm is described that retrieves vertical profiles of cloud microphysical properties based on a profile of radar reflectivity and an estimate of column optical depth. One of the principle benefits of optimal estimation techniques is the ability to diagnose uncertainties in the retrieved quantities. Quantifying these uncertainties is of critical importance, but is ignored in many studies or estimated by less reliable techniques.

This application of the algorithm to observations of jet stream cirrus is described in Chapter 5. Six cases of cirrus passing over the cloud radar at the Atmospheric Radiation Program Southern Great Plains site were identified. These included cirrus in formative and dissipative stages of development. Microphysical and environmental conditions surrounding the cirrus growth were described and summarized. It was once again found that these clouds occurred in regions of very weak vertical motion, which was just as often ascending as descending.

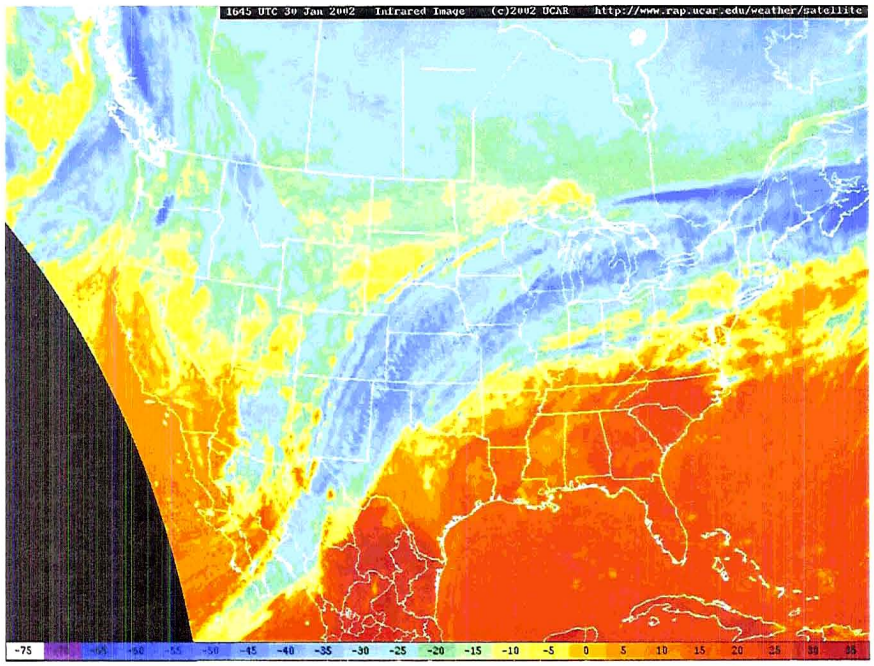

Figure 1-1: Infrared satellite image from 30 January 2002. Shows the abrupt northern boundary of the cirrus shield, generally coincident with the axis of the jet stream maximum. Courtesy of University Corporation for Atmospheric Research.

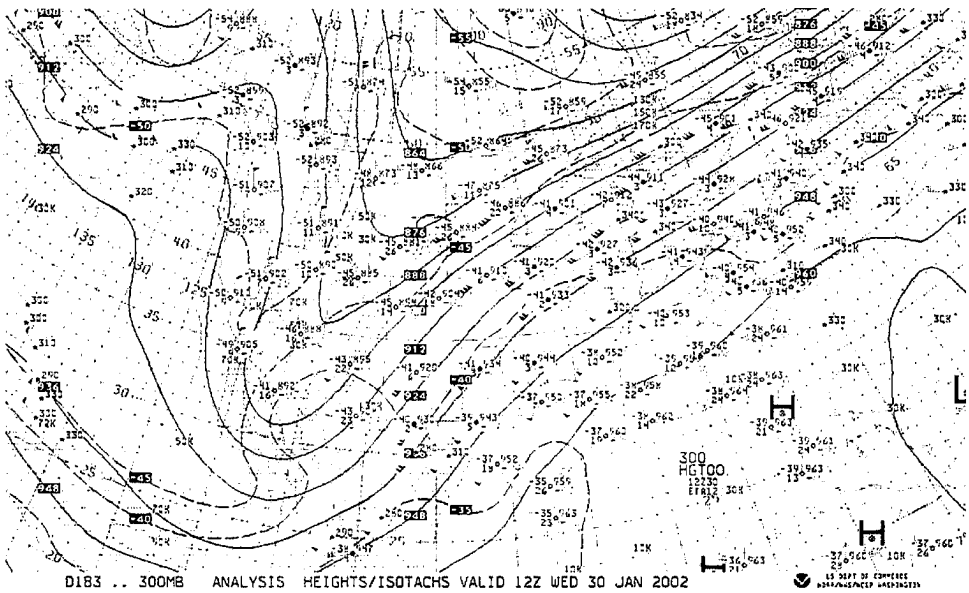

Figure 1-2: 300 hPa wind analysis for 12 UTC on 30 January 2002. Shows the alignment between the northern edge of the cirrus shield and the jet core.

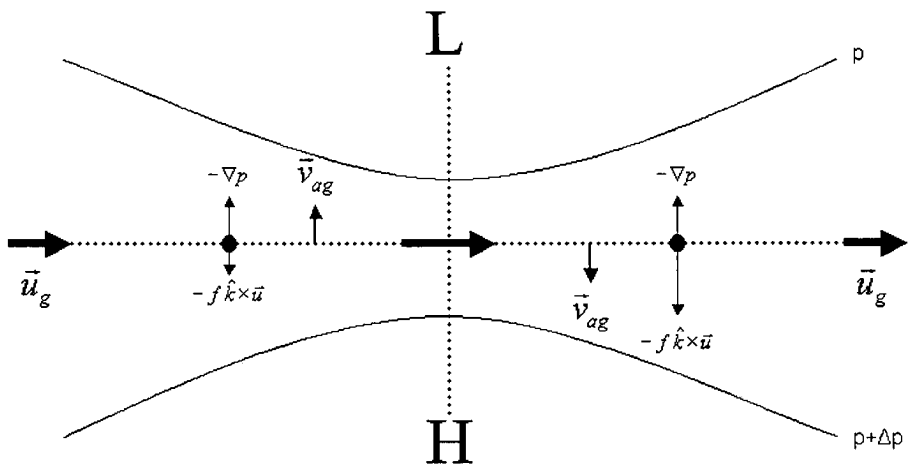

Figure 1-3: Schematic of force balance of a symmetrical jet streak with inviscid flow. Pressure contours are shown as solid lines, with low pressure at the top of the figure and high pressure at the bottom at the bottom of the figure. The force balance of parcels is shown at two locations represented by dots.

This page intentionally blank.

Chapter 2

2. COMPOSITE STUDY OF JET STREAM CIRRUS

2.1 Introduction to Composite Method

Composite studies of synoptic scale weather phenomenon have been employed in many past studies in the atmospheric sciences, and have been used to understand systems such as tropical cyclones, frontal systems, mesoscale convective complexes, and extratropical cyclones. The basic tenant of the method is to take many independent examples of some reoccurring, coherent phenomenon, and combine these cases together in such a way that an "average," or composite, event is created that is representative of the gross characteristics of any individual case. This combination is achieved by establishing a coordinate system with respect to some constant feature.

The purpose of this composite study is to apply a composite technique to strong North American jet stream events. Jet streams are deemed to be a suitable application since they occur on a large scale, are periodic, and have a synoptic structure that is closely tied to the dynamics of the system. The macroscopic and microphysical properties of the cirrus that are often observed near strong jet streams, and their connection to the large-scale dynamics have not, to date, been well documented.

The connection between the cloud properties of a system and the large-scale dynamics seems intuitive, but our knowledge is lacking in the area of cirrus clouds. Mace et al. (2001) write, "We are unable at the present time to define with quantifiable certainty a mean and standard deviation of any fundamental cirrus property, valid over a GCM grid box, given a set of resolved-scale dynamic and thermodynamic properties."

Two key characteristics that describe necessary conditions for performing a composite study of this type are the phenomenon must be both reoccurring and coherent. The phenomenon must be reoccurring because a large number of cases to produce a statistical significance composite. The phenomenon must also have a coherent structure; in other words, this repeating event must show some persistent structure between independent events, and there must be temporal coherence of each independent case over the time period of study (Lau and Crane 1995).

Jet stream cloud structures meet both of these requirements. The mid-latitude jet stream, as observed in this study, has a consistent structure that is observed over and over again in the continental United States. Strong, southwest to northeast-oriented winter jet streams dive across the U.S. numerous times each winter, with horizontal lengths on the order of 1000 to 2000 km and jet core widths of 100 to 300 km. Jet core winds of a strong system may exceed 80 ms^{-1} at 300 hPa. This structure, as these results will show, is associated with mid-latitude extra-tropical cyclones. The strong ageostrophic horizontal motion within the jet works in conjunction with other processes such as vorticity advection to drive vertical motion within the system.

The structure of this jet is also fairly coherent as it develops and moves eastward. A typical system may strengthen and develop in the favorable region on the lee side of

the Rocky Mountains. The characteristics of the systems change as it matures and moves east; for example, the upper level height gradient strengthens, the jet core tilts further westward with height and develops stronger winds, and the associated surface features also become more vigorous. However, these changes are not drastic enough to change the structure of the jet stream and associated cyclone in any dramatic way; qualitatively, the system is recognizable as the same phenomenon in all stages of its life cycle.

Before discussing the application of this method to the current study, one particularly successful example of the use of this method will be discussed.

2.2 Previous Studies Using Composite Method

As discussed previously, the use of the compositing has several strengths. It has been used to study various phenomena from squall lines (Johnson 1983) to tropical cyclones (Gray 1981) and mesoscale convective complexes (Fritsch and Maddox, 1981).

One of the primary advantages of using this technique is in situations where the data network is sparse or irregular, such as the infrequent upper-air observations within hurricanes. By combining several independent data sets, such data limitations can be partially overcome.

Composite studies of synoptic scale weather phenomenon have had considerable previous success. This composite study is loosely based on a recent study by Lau and Crane (1995), who examined North Atlantic extratropical cyclones using the composite technique. Using the C1 level cloud data set from the International Satellite Cloud Climatology Project (ISCCP), Lau and Crane focused their study on the space-time

variability of different cloud types within both extratropical cyclones and tropical circulations.

To examine North Atlantic extratropical cyclones, Lau and Crane chose to focus on one particular point on the earth that lies in the winter-season North Atlantic storm track, 46° N latitude, 46° W longitude. In each six-month cool season in their seven year sample, they identified nine dates that had the largest value of optical depth at this point, as determined from the ISCCP C1 data product. This lead to 63 "key dates" which formed the focus of the composite. These key dates corresponded to events whose optical depth was greater than 95% of optical depths in the total data set. A composite was then created from these key dates, using the location of maximum optical depth as a common reference point. These data are shown in Figure 2-1.

Figure 2-1 shows composite data for the key dates in the middle panel, with P_0 and N marking the locations of local maximum and minimum optical depth, respectively. The data represents deviation from a background level, obtained by averaging of ±1 and ±2 day lags relative to the key dates. The top and bottom panels are shown to delineate the temporal progression of the optical depth anomaly. This optical depth pattern has a southwest to northeast orientation, resembling the cloud pattern of a baroclinic leaf (Carlson, 1980). The baroclinic leaf is the name given to the cloud pattern that includes the surface cyclone and associated cold front, so named because the shape resembles a leaf when viewed on a visible satellite image. Propagation speed of the pattern is approximately 15 m s^{-1}.

To enhance the representativeness of their study, Lau and Crane then chose an array of 20 closely spaced reference sites in the North Atlantic. These reference sites

spanned approximately 15 degrees latitude and 20 degrees longitude over the North Atlantic, encompassing a region frequently affected by cyclones exiting the North American continent, and centered near the original 46° N latitude, 46° W longitude. These locations were chosen because they lie in the path of a coherent optical depth signal, as demonstrated in A composite chart was created at each of these grid points, and each composite was averaged together to form a final composite dataset.

Lau and Crane classified the composite cloud type using the same system that was employed to complete this current study of jet stream cloud patterns. A simple classification scheme was used, where cloud type was a function of only cloud-top pressure and optical thickness (see Table 1). This system uses descriptive qualifiers like "high top/thin" and "middle top/thick" to avoid confusion with officially recognized World Meteorological Organization cloud types.

European Center for Medium Range Weather Forecasting (ECMWF) reanalysis data was used to provide dynamical analysis. The ECMWF data was also composited over the key dates.

Figure 2-2 shows contours of geopotential height and horizontal wind vectors at 1000 hPa, as well as the presence and relative abundance of various cloud types. Their results clearly show a baroclinic leaf with the highest, thickest clouds leading the low pressure center. Southerly flow dominates in the high cloud-top shield, while most of the low clouds are found in the northerly flow behind the system.

In fact, the Lau and Crane results are consistent with many ideas of traditional extratropical cyclone structure. Figure 2-3 shows a similar analyses for three vertical levels. Contours of 200 hPa vorticity advection, 500 hPa vertical motion and 1000 hPa

temperature advection are shown in panels (a), (b), and (c), respectively. Panel (a) shows positive vorticity advection coincident with rising motion east of the upper-level trough. Panel (c) demonstrates that the comma cloud region is coincident with low-level warm-air advection, and subsidence in the region behind the comma is associated with cold-air advection and lower top clouds. The comma cloud is the classic hook-shaped cloud pattern of a synoptic-scale low pressure system.

In addition to serving as a model for the current study, the work of Lau and Crane served to substantiate that it is possible to combine independent dynamical and cloud-climatological datasets in such a way as to produce results that are consistent with the well-documented classical understanding of synoptic scale systems. Lau and Crane write that their study offers "strong confirmation of the reliability of the cloud detection algorithms used in producing the ISCCP analyses."

2.3 Data Sets

Dynamical reanalysis data were provided by the European Center for Medium Range Weather Forecasting (ECMWF). Data were obtained for the period 1984-1987. Reanalysis data were provided on a 2° latitude by 2° longitude grid, with seventeen vertical levels extending from 1000 to 10 hPa. The three-dimensional variables obtained for all points in this grid were temperature, geopotential, zonal wind, meridional wind, vertical pressure velocity (omega), and specific and relative humidity. It is noted that the ECMWF reanalysis data set are not pure observations, but an assimilation of observations with a model first-guess. This first-guess is a model prediction from the previous 6-hour forecast (Newman et al., 2000). Reanalysis data are therefore a mix of model forecasts

and observations, which has the benefit of spatial and temporal continuity but comes at the cost of modification of the observations.

The ISCCP DX dataset provided the satellite cloud data for this study. The DX dataset is a three hourly, 30 km by 30 km global dataset. Unlike the D1 and D2 datasets, DX is not a merged data set; individual platforms are not combined into a single set of variables. The observing platform chosen for this project was GOES-6, an operational geostationary satellite that was well-situated to view the central and eastern U.S. over the period of consideration. GOES-6 was chosen since data coincided temporally with the reanalysis data described above.

2.3.1 ISCCP Cloud Retrievals

Variables relevant to this study include cloud optical depth, cloud top temperature and pressure, visible radiance, and infrared brightness temperature. ISCCP cloud top temperature and pressure are calculated by assuming that the cloud has an emissivity of unity, meaning that the cloud is opaque to infrared radiation. This method will be referred to as the blackbody assumption, or Method 1. The satellite zenith angle is then interpolated to a lookup table of pre-calculated values of infrared brightness temperature at three zenith angles. A match can then generally be obtained at some pressure level, and the temperature is retrieved as the physical temperature from a nearby TOVS (TIROS Operational Vertical Sounder) vertical profile (Rossow 1996). Exceptions occur where the observed brightness temperature falls outside the range of known physical values from the TOVS profile, and handling of these exceptions is described in some detail in the ISCCP technical documentation.

Visible cloud optical depth for liquid clouds is obtained by comparing observed visible radiances with those in a lookup table. These were pre-calculated from a radiative transfer model under the assumption that all clouds consist of liquid drops with a radius of 10 μm. This lookup table relates the optical depth to the viewing geometry, surface reflectance, and cloud-top pressure. Rossow reports that interpolation errors in this process are less than 10%. The DX analysis techniques further reduce error at low optical depths by using an interpolation that is linear in the logarithm of optical depth.

Ice cloud optical depth is calculated using a similar lookup table method. Here, ice polycrystal clouds with an effective radius of 30 μm are assumed. This product is available for all cloudy pixels where ice cloud temperature is less than 273 K.

It has been stated that these methods assume that the cloud is opaque to infrared radiation, but this is a poor assumption for many types of clouds, especially cirrus. Following these calculations, the derived parameters are tested to see if, in fact, the cloud is adequately represented as a black body. If not, then a correction can then be applied where necessary. This correction, as applied to ice clouds, is referred to as Method 2. Mie scattering code is used to calculate the 10.7 μm optical depth, τ_{IR}, of a liquid cloud consisting of 10 μm radius spherical drops, and an ice cloud consisting of spherical particles of 30 μm radius. Note that this assumption of spherical particles is sufficient, since infrared scattering is insensitive to particle shape (Minnis et al. 1993). This calculation allows the transmission of the cloud to be calculated:

$$T = \exp(-\tau_{IR} / \mu) \tag{2.1}$$

where μ is the cosine of the solar zenith angle. If the transmission, T, is less than 0.05 (such that τ_{IR}/μ is greater than 5.5) , then the assumption that the cloud is opaque to infrared radiation is taken to be sufficiently accurate. Otherwise, a correction is applied.

For this correction, the observed infrared radiance is assumed to be the sum of contributions from the cloud layer and the underlying surface (Figure 2-4). Water vapor absorption below the cloud is accounted for by assuming the radiation coming from the surface and lower atmosphere can be simply represented by the clear-sky radiance, B_{TS}. If the cloud emits radiance B_{TC}, then the observed radiance at the top of the atmosphere is simply:

$$B_{TOBS} = (1-T)\,B_{TC} + T\,B_{TS} \tag{2.2}$$

This allows the following simple correction to be applied:

$$B_{TC} = \frac{B_{TOBS} - T\,B_{TS}}{1-T} \tag{2.3}$$

where B_{TC} is the corrected radiance emitted by the cloud, from which corrected cloud brightness temperature directly follows. The corrected cloud top pressure is then obtained from the known temperature profile. Known problems with this method, especially with extremely thin clouds, are discussed further in the ISCCP technical documentation.

Differences between cloud top temperatures and pressures obtained from Method 1 and Method 2 will be explored further in the results section. It should also be noted that the radiative transfer model used to obtain optical depth and cloud top information requires visible reflectance, so only daytime cases are considered in this study.

One final correction worth noting is related to the viewing angle-dependent effects of infrared scattering. Mie scattering code is used to calculate the scattering

effect, which tends to cause a small increase in brightness temperature when a cloud is viewed at angles approaching nadir.

2.3.2 ISCCP Data Gridding

ISCCP DX data were provided on an equal area grid, so it had to be transferred to a latitude/longitude grid for purposes of comparison with the ECMWF reanalysis data. Each pixel was assigned to the appropriate 1° latitude by 1° longitude grid box, then averaging was performed over all pixels to obtain a single value for each grid box. On average, three to eight pixels were averaged in each 1° by 1° grid box. Though this averaging procedure degraded the resolution of the dataset, it was certainly a reasonable solution given the averaging that would be applied during compositing.

2.4 Methodology

This section describes the method by which the composite analysis of jet stream cloud structures was accomplished. Mid-latitude mean winds and the strength of weather systems are known to be more vigorous in summer, owing to a generally greater winter baroclinicity in mid-latitudes and the need for latent heating provided by precipitation to balance the negative wintertime energy budget. For this reason, only cold season events, those that occurred in October through April, were considered. The years considered for this case study were 1984 through 1987. The former corresponds to the beginning of the ECMWF reanalysis data set, and the latter corresponds to the last year GOES-6 was operational. To prevent compatibility problems between different platforms in the DX dataset, only GOES-6 data were used in this study.

The 18 UTC ECMWF reanalysis data for these months were scanned for jet stream events that met the following criteria:

1. The jet stream core occurred in the area of eastern North America defined in Figure 2-5. This area roughly defines an area frequented favored for cyclone development, given its position in the lee of the Rocky Mountains.
2. The jet stream had a general southwest to northeast orientation. This ensures that jet structures are selected that are typically associated with cyclogenesis. The poleward branch of the jet, to the east of the mean upper level trough, is associated with low level cyclonic flow and upward motion, and thus is the most likely location to find dynamically-forced cirrus that are of interest.
3. 300 hPa wind speed in the jet core was at least 70 m s^{-1}. Though wind speeds have been observed to be considerably higher in a strong wintertime jet core, 70 m s^{-1} winds are almost always associated with strong systems.

These criteria ensured that only the strongest events, those most likely to be associated with a well-defined cirrus shield, were selected in the years when data were available. Examining the ECMWF reanalysis data, approximately 40 potential cases were identified using these criteria.

However, not all of these events were established as "key dates". Since the jet stream structure is often temporally coherent from day to day, many of the events occurred on consecutive days. To ensure that independent systems were considered, only the strongest of multiple-day events were selected for key dates. After filtering, fourteen key dates were left to be used in the composite. The 300 hPa wind reanalysis is shown

for six selected dates in Figure 2-6, and the GOES-6 ice-cloud optical depth are shown for these same dates in Figure 2-7.

Figure 2-6 demonstrates the large variability between the cases. The location of maximum wind varies from off the east coast of Florida on 11 November 1987, to as far north as the upper Great Lakes on 7 March 1985. Although the jet orientations vary widely, all exhibit the general southwest to northeast orientation as required by the selection criterion.

To perform a composite, a common coordinate system was established and all data were transferred to this system. In this case, the location of maximum wind (LWM) at the 300 hPa level within the jet has been used to anchor separate cases to a common origin. For each of the key dates, dynamical and cloud information was shifted such that the LWM was located at the origin, hereafter referred to as 0° latitude, 0° longitude. After establishing a common coordinate system, data for the key dates were averaged to provide a composite jet stream event, with averaged dynamical and cloud fields.

Though it will be shown that this technique produces a fairly realistic composite event, it should be noted that several factors can cause errors in the analysis. It is obvious from Figure 2-6 that no two events are alike. Jet streams differ in length, width, orientation, and position of maximum upper level wind. It is hoped that by choosing only southwesterly jet streams with a maximum winds at or above 70 ms^{-1}, the composite technique will average over events that have similar structure; it is this repeating structure, of course, that is the focus of this study.

2.5 Composite Results

The dynamical composite results will be discussed separately from the cloud composite results, and then the two will be combined in terms of several cross sections taken through the system.

2.5.1 Dynamical Composite

First, results will be presented from the dynamical portion of the composite; that is, those results obtained from compositing the ECMWF reanalysis data. The composite 300 hPa wind speed and vectors are presented in Figure 2-8. Note that these figures are presented with respect to the LWM, which is always located at the origin (0° latitude, 0° longitude). The analysis shows the composite jet stretching southwest to northeast, with a maximum core wind of 79.4 m s^{-1} at the origin. Flow is generally southwesterly along the jet streak axis, consistent with the individual cases. Cyclonic flow is evident to the northwest of the jet, with anticyclonic flow southeast of the jet.

At first glance, this 300 hPa pattern could be mistaken for a weather chart at any instantaneous time. The spatial scale, intensity, and wind vectors within the composite case are similar to what may many expected from any strong winter system. There are exceptions to this, of course; for example, the shear zone on the cyclonic side of the jet streak may be stronger than one would observe on a weather map, but overall the pattern is fairly consistent with expectations.

The 500 hPa and 1000 hPa height fields are shown in Figure 2-9. The 500 hPa trough is located approximately 6° longitude west of the 300 hPa jet core at the latitude of the origin.

The 1000 hPa height may be regarded as a proxy for the surface pressure since 1000 hPa is very close to the earth's surface, and hydrostatic balance dictates that height contours on a constant pressure surface are identical to pressure contours on a constant pressure surface. A closed low pressure center is evident at 4° latitude , 6° longitude, to the northeast of the jet core center. Convergence of the cyclonic 1000 hPa wind vectors also reveal the location of this low pressure center. This location, several degrees east of the 500 hPa trough, is indeed where one would expect to find a surface low pressure center since upper level ageostrophic divergence is maximized in the same vertical column where low-level convergence occurs. Thus, the composite systems tilts westward with height, a characteristic shared with observations of mid-latitude cyclones in accordance with the requirements of hydrostatic balance.

A pressure trough extends southward from the low pressure center. This is the location of a front in the composite system, as has been marked in Figure 2-9. It is also readily located by observing convergence and directional shear of the 1000 hPa wind in the region surrounding the trough. As is typically observed in mid-latitude systems, the front drops south from the low pressure center, bows southeastward, and then curves back to the southwest at lower latitudes.

Figure 2-10 shows composite 500 hPa height and horizontal relative vorticity. Relative vorticity reaches a maximum value of 8.7×10^{-5} s^{-1} at about two degrees northwest of the origin. Assuming quasi-geostrophic flow, it is evident that relative vorticity advection is maximized in the region to the northeast of the vorticity maximum. This coincides with the location of the surface pressure center. Since positive advection

of relative vorticity at 500 hPa is known to generally coincide with upward motion, these fields are consistent with observations.

The composite 1000 hPa temperature advection is shown in Figure 2-11, expressed in Kelvin per day. For reference, the location of the surface front, as determined by location of the 1000 hPa trough, has been superimposed on the figure. The pattern of temperature advection clear supports the positioning of this front and demonstrates the connection between the mass and thermal fields in the composite. Cold advection is occurring behind the front, with a maximum value of -8.8 K day^{-1}, while warm advection with a maximum of about two thirds this magnitude is occurring in advance of the front. The front follows the zero temperature advection contour fairly closely within about 7° latitude either side of the origin. Farther from the origin, the variability between the cases that were averaged to perform the composite become more apparent; thus, it is not surprising that the quality of the composite degrades with increasing horizontal distance from the LWM.

Next, vertical motion within the system is analyzed. Figure 2-12 shows the composite 700 hPa pressure velocity, ω, superimposed on the 300 hPa wind field. Two broad centers of low-level upward motion are evident. One is located in the right entrance region of the jet streak (near -8° latitude, -2° longitude) and the other is co-located with the surface low pressure center, below the left exit region of the jet streak (near 7° latitude, 3° longitude). Subsidence is occurring in the left-entrance region (-2° latitude, -7° longitude).

This result is fairly consistent with current knowledge of jet stream dynamics. The classical model of motions within jet streaks is described by Uccellini and Johnson

(1979) and in Chapter 1.3. It is noted that the composite system shown in Figure 2-12 clearly demonstrates ascent in the right-entrance region and left-exit region, as well as descent in the left-entrance region. However, a broad region of ascent is located in the right-exit region where classic models like that of Uccellini and Johnson (1979) would diagnose subsidence.

It is concluded from these analyses that the composite technique employed produces a dynamically reasonable representation of a strong jet stream. The composite system tilts westward with height. Upper and lower-level troughs are positioned in locations that are consistent with our observations of mid-latitude systems. The composite has a surface frontal system with reasonable cold advection behind the front and warm advection in advance of the front. Mid-level vorticity advection leads to upward motion in expected locations. Further examples of the dynamical consistency of the system are given in Section 2.5.3.

2.5.2 ISCCP Composite

Next, the results of the ISCCP cloud properties composite are presented. First, however, it is prudent to discuss a key limitation to the ISCCP composite. As is apparent from Figure 2-7, data gaps, represented by black pixels, exist in the data and are especially prevalent over the northeastern corner of the figure for key dates in 1987 and 1988. This is a result of the failure of GOES-5 in July of 1984, and the subsequent movement of GOES-6 to a more central 108° W longitude.

Such spatial and temporal inhomogeneities in the data set can lead to a distortion of the composite ISCCP results. This is not an issue for the dynamical reanalysis data, since

the reanalysis scheme produces output for all grid boxes within each time step. Figure 2-13 presents the total number of key dates that contribute to each 1° by 1° grid box of the cloud composite (left panel) and the total number of original ISCCP DX pixels contributing to the same (right panel). The largest contribution comes from data in the southwestern part of the system, with all 14 key dates and up to 140 pixels contributing to each composite grid box. Data availability generally decreases toward the northeast, with only a few contributing key dates and DX pixels. Note, however, that the number of contributing cases diminishes more slowly than the total pixels, since in theory only one DX pixel is needed to form the grid that constitutes a key date.

It is not immediately clear what effect this inhomogeneity should have on the composite results. Certainly, if only a few pixels are averaged to form a grid box value on any key date, one must question whether how representative this average is of a 'typical' system. The cumulative probability function of the number of contributing DX pixels for the 1° by 1° composite system is shown in Figure 2-14. The median value of the number of contributing pixels, N, is 52.0, indicating that half the grid boxes have 52.0 or less contributing pixels while half have more. Though it would be desirable for the median to be larger, the composite results will now be considered but with the inherent limitations in mind.

Figure 2-15 shows the composite visible albedo and longwave infrared brightness temperature. The visible albedo is a composite of the GOES-6 Channel 1 (0.55 – 0.75 μm) product, and the longwave infrared is a composite of the Channel 4 (10.2 – 11.2 μm) product.

GOES-6 Ch. 1 is located near the center of the solar emission spectrum, as seen from the spectral response function of Figure 2-16, and is at short enough wavelengths that terrestrial emission is negligible. This, of course, is the reason that Ch.1 data are available only during the daytime when solar radiation reflected off the earth is received by the satellite sensor. This channel is located in an atmospheric window, meaning that absorption by atmospheric gases is minimized in this region. Since nearly all clouds have a higher albedo than the underlying surface, this channel is useful in identifying cloud types and cloud systems. Observations of visible radiance in the ISCCP analyses are used in the derivation of cloud optical depth.

Ch. 4, the so-called longwave infrared channel, is also located in an atmospheric window. This channel sees almost entirely terrestrial radiation (Figure 2-16), and provides a direct measurement of cloud infrared brightness temperature. It is used in the ISCCP analyses in the determination of cloud-top temperature and pressure.

The cloud structure of a mid-latitude cyclone is clearly evident in the composite fields of Figure 2-15. This cloud structure will be examined from southeast to northwest. In the far southeast, there is a region of low albedo and high brightness temperature. This can be interpreted as a clear region associated with synoptic-scale subsidence in advance of the frontal region. Continuing to the northwest, the next feature is the frontal cloud band.

The visible composite reveals this covers an extensive horizontal area surrounding the low pressure region and to the southwest along the cold front where some of the brightest, and presumably thickest, clouds are found. The cloud shield extends to the east, as well, centered roughly on 0° latitude. This may reveal the location of a composite

warm front; this assertion is supported by the 1000 hPa temperature advection (Figure 2-11), which shows warm advection maximized at 4.8 K day^{-1} in this location, and the eastward extension of upward 700 hPa vertical motion (Figure 2-12). A region of colder brightness temperatures extends along the same area, although the coldest cloud tops are present over a smaller horizontal area than the deeper, brighter clouds. A dry intrusion is present behind the front and wrapping into the low pressure center, characterized by lower albedos and higher brightness temperatures.

Further to the northwest, the infrared channel shows the signature of a comma cloud. This relatively large region to the north of the origin has an average brightness temperature of about 245 K.

The left side of Figure 2-17 shows the Method 1, or uncorrected, cloud top pressure and cloud top temperature. A broad region of enhanced optical depth is evident stretching from roughly -15° latitude, -15° longitude to 5° latitude, 20° longitude. It is not surprising that the visible cloud optical depth has the same characteristic shape as the Ch. 1 composite, since the latter can be used as a proxy for the former. This region is roughly aligned with, but several degrees ahead of, the jet streak core; this is consistent with the previously observed westward tilt of the system with height. An area of enhanced optical depth, with a maximum value of 60.5, is located in the southwestern part of the system. Another noteworthy enhancement of optical depth extends from the main region at the origin, north-northwestward to about 15° latitude, 5° longitude. This region is coincident with the western portion of the comma cloud.

The blackbody-derived cloud top pressure and temperature panels of Figure 2-17 quantify some of the qualitative assertions that have been made by analysis of the Ch. 1

and Ch. 4 composites. The coldest and highest clouds are located from about 10° to 25° longitude east of the origin, with a minimum cloud top pressure of 331 hPa and temperature of 232 K in this region. This region of potential cirrus is along or just east of the jet axis, and nearly 10° east of the surface front.

The composite ice-cloud cloud top temperature and pressure are shown on the right side of Figure 2-17. At first glance, the composite is far less recognizable that the uncorrected version. There is, for example, a large area of warm clouds with tops in the middle troposphere centered just northwest of the origin. This is inconsistent with both conventional knowledge of synoptic scale systems and previous results. However, it should not be particularly surprising that an algorithm which is tuned for ice clouds does not perform well in warmer regions.

Recall that clouds with emissivities that depart considerably from unity (such as optically thin ice clouds) should be better characterized by this technique than by Method 1, since these clouds emit less radiation that a black body at the same temperature. With this in mind, there are a several locations in the Method 2 composite that contain both cold and high clouds. Pixels with cloud top pressure and temperature less than 400 hPa and 240 K, respectively, and optical depths less than 15 are shown as dark blue pixels in Figure 2-18. Those regions that meet the first two criteria but have optical depths greater than 15 are shown as lighter blue pixels.

Several potential regions with cirrus clouds are evident. One such region, in the northeast portion of the system, is located primarily to the northwest of the jet maximum in the comma clouds region. Further southeastward there is a transition to higher but somewhat thicker clouds, oriented parallel to the jet max and just to its south. Note that

this region is coincident with the coldest and highest clouds found in the Method 1 composite, and may be associated with the higher tops of convective clouds rather than pure cirrus. However, given the large area covered by this region, it is also possible that this area consists of cirrus on top of brighter, lower clouds. Another region of high, cold, and optically thin clouds occurs on the southwest side of the system, just along and behind the jet axis. The prevailing cloud top pressure in this region is 300 to 400 hPa with cloud-top temperatures between 210 and 230 K. These clouds are concentrating on the southern end of the jet, split approximately two-thirds to the left of the jet axis and one-third to the right. Finally, high clouds are sporadically located throughout the lower-left corner of the plot.

Although it is uncertain that these regions of the composite actually contain significant cirrus coverage, there are a priori reasons to expect that they may. Menzel et al. (1992) examined the distribution of cirrus around strong jet streams for three winter months in 1986 and 1988. Figure 2-19 shows the distribution they observed. Cirrus clouds were present along all quadrants of the jet, but most prevalent in the accelerating region, or entrance region. In particular, in the divergent right-entrance region cirrus accounted for 23% of all clouds. Note that this is inconsistent with the classical model of Uccellini and Johnson (1979). The cirrus cloud fraction in the convergent left-entrance region was only 6% in the three months considered. Cirrus fraction in each of the jet exit regions was 10%.

The composite results, like the study of Menzel et al, show significant coverage in the accelerating region, roughly aligned with the jet axis and within 5 to 10 degrees of the jet core. The present composite shows some consistency with this earlier study and there

is reason to believe that the Method 2 composite does in fact outline areas that consistently produced cirrus, at least in the fourteen cases considered. Given the different orientations of the various cases, it is difficult to express a certainty that the cirrus actually occurred in the quadrants in which they are portrayed by the composite. However, the southwestern region is near the core but split between the left and right-entrance regions, and the thin cirrus in the vicinity of the comma cloud are located in the left-exit regions of the jet. The region of higher but thicker clouds, which may contain cirrus above thicker clouds, are in the right-exit region and have a sharp boundary against the jet core to the north. It is noted that this is significantly more localized than the large expanses of cirrus that are often observed.

This is further examined in terms of the dynamical composite. Figure 2-20 shows the 300 hPa vertical motion field. Synoptic-scale vertical motion in the region of the cirrus in the southwest is nearly neutral, although there is weak rising motion on the east side closer to the jet core and weak subsidence on the west side. The cirrus in the northeast portion of the system also border on the neutral vertical velocity region. This near-neutral vertical motion field is consistent with the case studies presented in Chapter 5.

Some statistical information about the composite will now be presented. Standard deviation of the composite system is shown in Figure 2-21. The top panels show the standard deviation of the Method 1, or uncorrected, composite. Some of the lowest values are found ahead of the front, where the composite tends indicate the sky is more or less cloud-free. Typical values of the standard deviation of cloud top pressure in the cloud band are 150 to 250 hPa, and for cloud top temperature a typical standard deviation

is 20 to 30 K. The Method 2, or corrected, standard deviations are shown in the bottom panels. These values, like the composites themselves, show less intuitive organization.

Probability density functions of these standard deviations are shown in Figure 2-22. These plots are useful to conceptualize the typical spread in standard deviations for the composite system, and at least hints at the quality or usefulness of the composite technique. All four plots are, to some degree, skewed toward lower values.

2.5.3 Cross Sections: Dynamical and Cloud Features

In an attempt to synthesize the dynamical and cloud composites, several cross sections of dynamical and cloud fields across the jet have been created. The locations of these cross sections are shown in the top left panel of Figure 2-17. Two were chosen to cross the jet in an east-west direction, and one crosses north-south.

In the plots of the cross sections, temperature is shown in the left panel and vertical pressure velocity in the right panel. The vectors show the component of the flow along the cross-section, although the component in the vertical direction has been amplified by a factor of 15 such that the motion is visible in the plot. The location of the cloud tops derived from the ISCCP composite are shown by solid dots every 5 degrees of latitude or longitude. The black dots correspond to the Method 1, or uncorrected, values and the blue dots correspond to the Method 2, or ice-cloud corrected values.

The cross-section across AB is shown in Figure 2-23. AB is an east-west cross section taken across the southern portion of the jet, intersecting the optical depth maximum in the composite. Subsidence is evident in the colder air behind the system while strong rising motion, greater than -1.5 μb s^{-1}, is occurring ahead of the system.

The westward tilt of the system with height, consistent with synoptic knowledge, is also apparent. Significant differences between the Method 1 and Method 2 cloud tops are again visible, and at times exceed 200 hPa. The largest differences are in the cold air behind the front and the upper-level jet, a location that has been singled out for potential occurrence of jet stream cirrus. As has been previously discussed, if high, relatively thin clouds are present over a cloudless underlying sky, then the Method 2 technique is likely to provide a better representation of the scene.

Cross section CD (Figure 2-24) is taken across the northern portion of the system, parallel to the location of the warm front. Here, even stronger sinking motion is occurring in the cold air to the west of the system, with a rapid transition to rising motion just before crossing the jet axis. The composite cloud top analysis shows very closely agreement between Method I and Method II. Cloud tops are lowest with the cold air and subsidence and highest in the warm air in advance of the cold front. The westward tilt of the system is again apparent.

The third cross section, EF, is taken north-south across the jet. Upward motion is occurring in the warmer air to the south, which crosses the jet axis and rises along the frontal slope, finally descending in the colder air to the north. The cloud top pressure difference between Method 1 and Method 2 exceeds 500 hPa at -15° latitude, but gradually reduces to between 100 and 200 hPa at latitudes north of -12.5° latitude.

All three cross sections reveal a dynamical structure to the composite that is remarkably consistent with synoptic knowledge, and enhance the credibility of the composite method used in this study. Overlay of the cloud-top heights reveal some

differences between the methods used to derive this quantity, but fit generally well with observations of strong mid-latitude cyclones.

2.6 Conclusions from Composite Study

The composite technique used, based on the location of maximum 300 hPa wind, has been explored in terms of the dynamical and cloud properties of the composite. The composite system has been shown to exhibit features that are consistent with traditional observations of mid-latitude cyclones. Synoptic scale mid-level vertical motion is maximized in the right-entrance and left-exit region of the jet streak maximum, generally consistent with conceptual models, except ascent is also present in the composite in the right-exit region. Cloud optical depths are enhanced in these regions, associated with deep convection in the right-entrance region. The ISCCP Method 1 composite, based on simple lookup tables of cloud-top temperature and pressure for clouds that emit as black bodies, shows a synoptic scale cloud band with a cold front and surface lower pressure and associated baroclinic leaf cloud features. The Method 2 composite, including a correction to the cloud-top pressure and temperature fields that is most useful for clouds that consist entirely of ice crystals, shows three main regions of high, cold clouds. One is in the jet streak exit region, in the northeast part of the system. The second is associated with high, cold clouds to the southwest of the jet maximum but roughly aligned with the jet axis, and the third is sporadic cirrus coverage in the southeast part of the system, in advance of the cold front. Vertical motion at cloud level diagnosed by the ECMWF reanalyses is ascending in the region of the comma cloud, nearly neutral in the somewhat thicker high clouds to the southeast of the comma, and neutral or split between weak

ascent and weak subsidence in the accelerating region of the jet. Since jet stream cirrus clouds must be supported by the expansion and cooling of rising air parcels, this suggests that either the dynamical lift is very weak or too shallow to be represented by the ECMWF reanalysis data, or alternately is not resolved at all by in the data set.

The finding that cirrus occur preferentially in only certain parts of the system requires explanation given the large expanses of cirrus that are often observed, as demonstrated in Figure 1-1. The composite shows significant cirrus coverage only in those portions of the system that consistently have high thin clouds relative to the 300 hPa wind maximum. Although cirrus may well occur in other regions of the jet, it is possible that they do not occur consistently enough to avoid being averaged with lower, warmer clouds in the composite. Furthermore, it is difficult to separate high clouds from lower clouds when they occur simultaneously in a given pixel.

In the remainder of this study, a technique will be described that is used to remotely determine the microphysical parameters of these cirrus clouds, and several case studies will be examined in this context. Results from this composite study will then be tied to information learned in the case study to provide a broad view of jet stream cirrus clouds, their properties, and the environment in which they form.

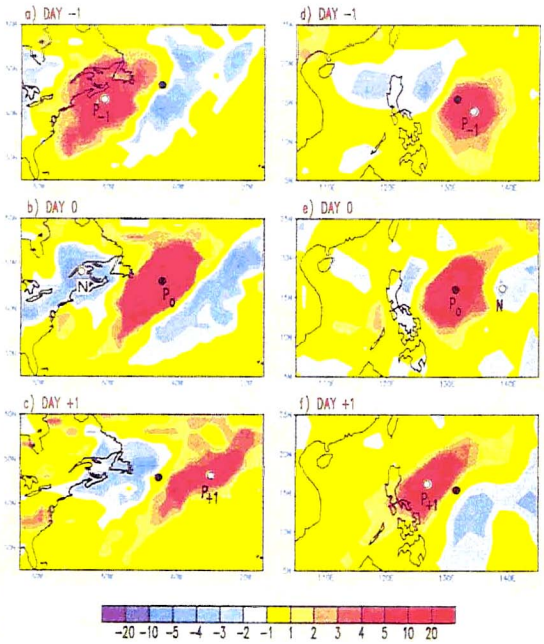

Figure 2-1: Composite charts of cloud optical thickness during the cool season. Color shading represents optical depth deviations from a background level obtained by averaging over ±1 and ±2 lag days relative to the key dates. From Lau and Crane (1995).

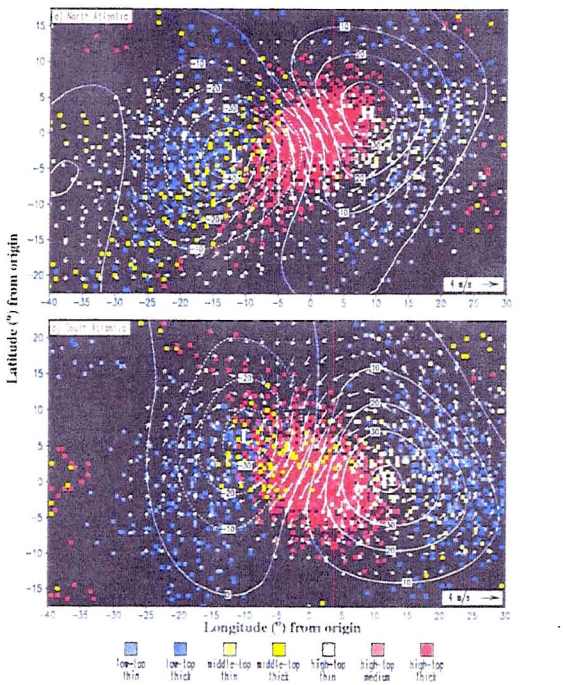

Figure 2-2: Distribution of horizontal winds and geopotential height (10 m interval) and various cloud types for the composite. From Lau and Crane (1995).

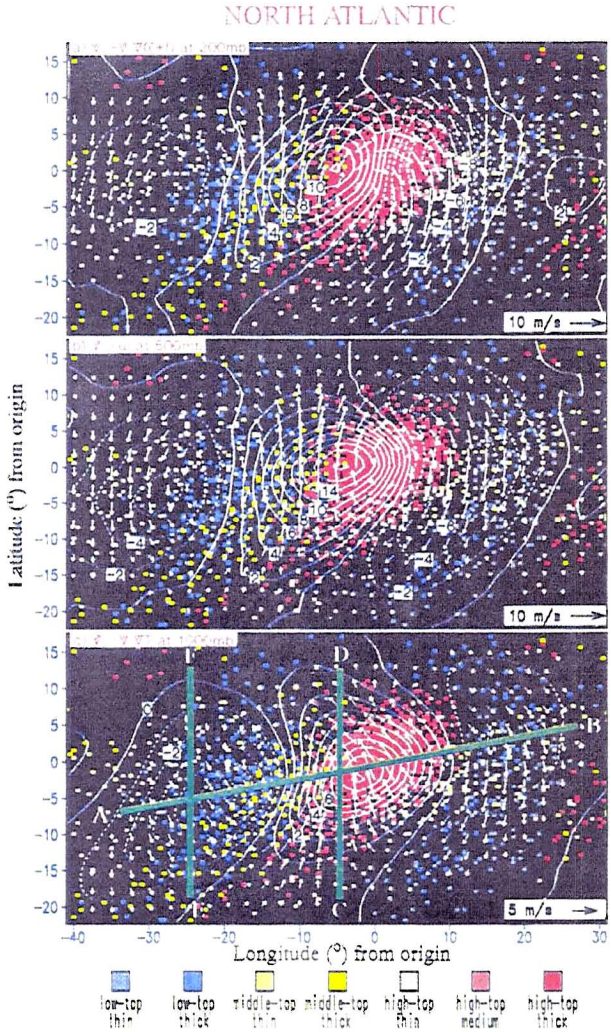

Figure 2-3: As in Figure 2-2, but for (a) 200 hPa absolute vorticity advection, $-\vec{u}\cdot\nabla(\zeta+f)$ (interval of 2 x 10^{-10} s^{-2}), (b) 500 hPa negative pressure velocity, $-\omega$ (interval of 2 x 10^{-2} Pa s^{-1}), and (c) 1000 hPa temperature advection, $-\vec{u}\cdot\nabla T$ (interval of 1 x 10^{-5} °C s^{-1}). Horizontal winds are also show at these levels. From Lau and Crane (1995).

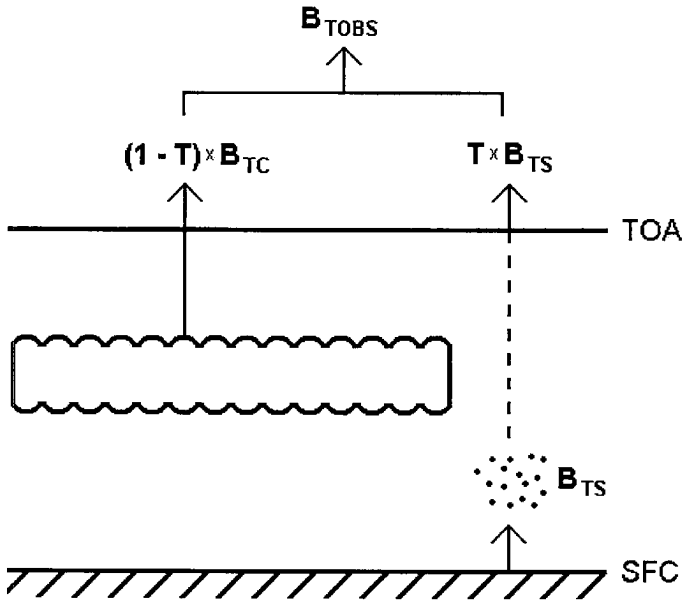

Figure 2-4: Simple model used in calculation of the outgoing radiance at the top of the atmosphere (TOA), represented by B_{TOBS}. The clouds emits radiance of B_{TC}. B_{TS} represents emission from below the cloud, with contributions from water vapor and the surface (SFC).

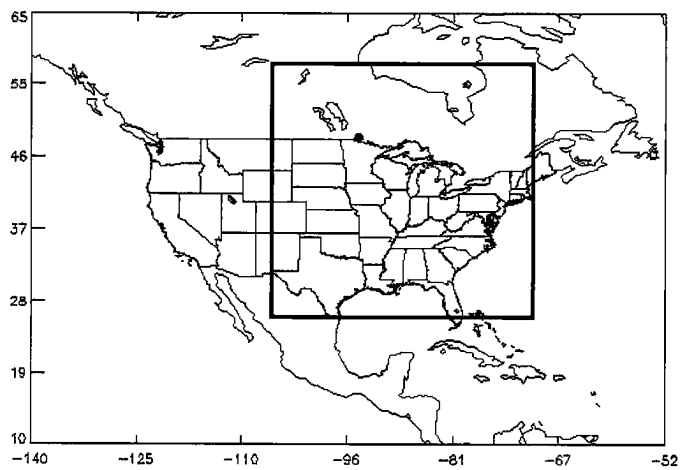

Figure 2-5: Sample area considered for strong jet stream events. To meet the criteria in the text, it was required that the jet stream maximum be located in the box shown.

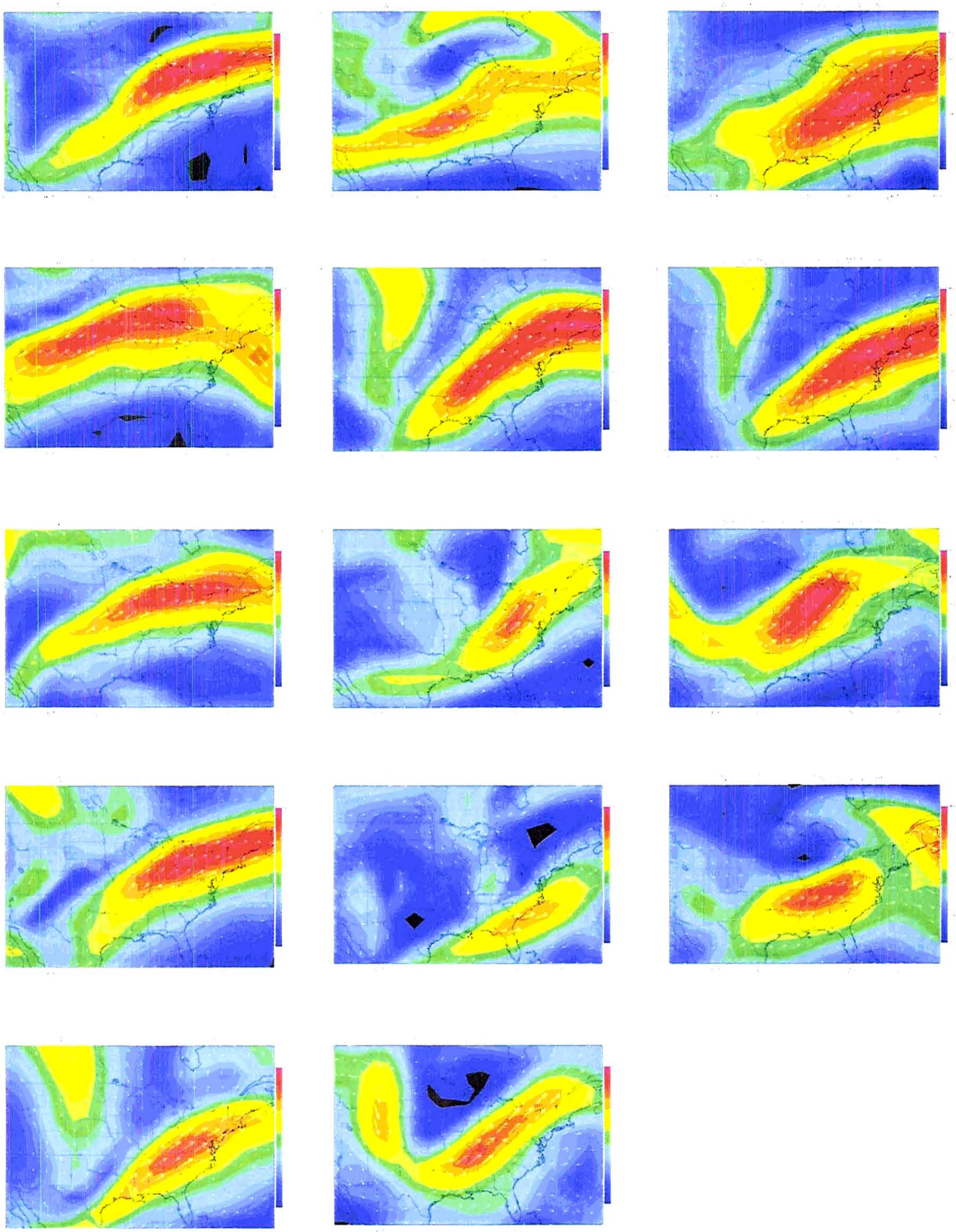

Figure 2-6: 300 hPa winds in m s^{-1} for the 14 key dates. The selection clearly shows that each event has a unique jet structure and orientation.

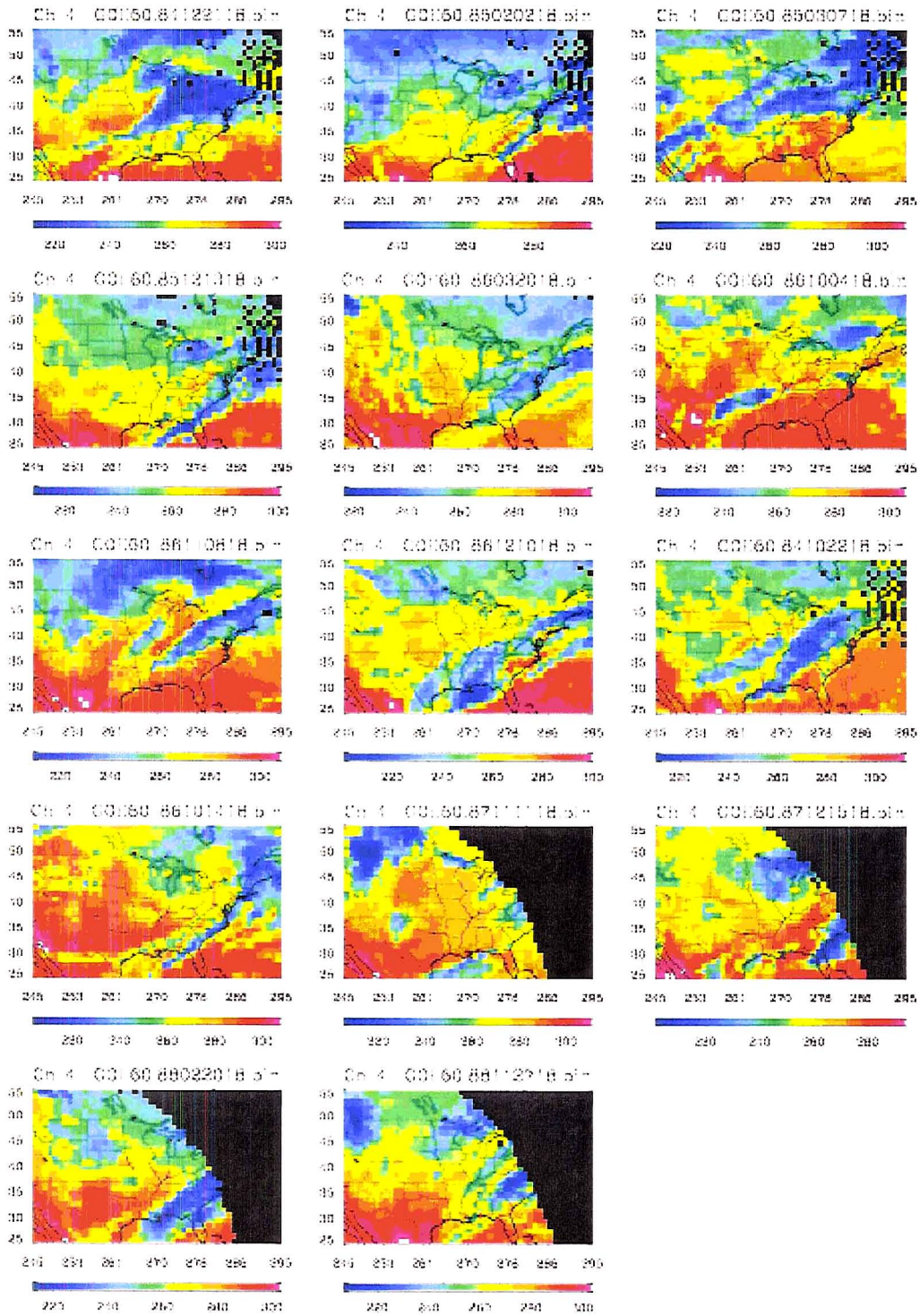

Figure 2-7: GOES-6 infrared brightness temperature in degrees Kelvin for the 14 key dates.

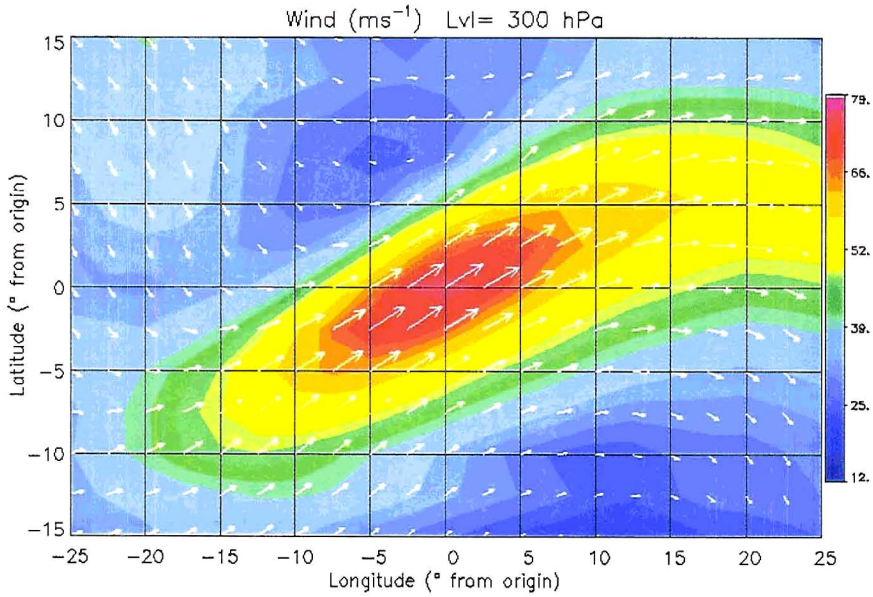

Figure 2-8: Composite 300 hPa winds in ms^{-1} with wind vectors. Latitude and longitude are represented with respect to the location of maximum wind (LMW).

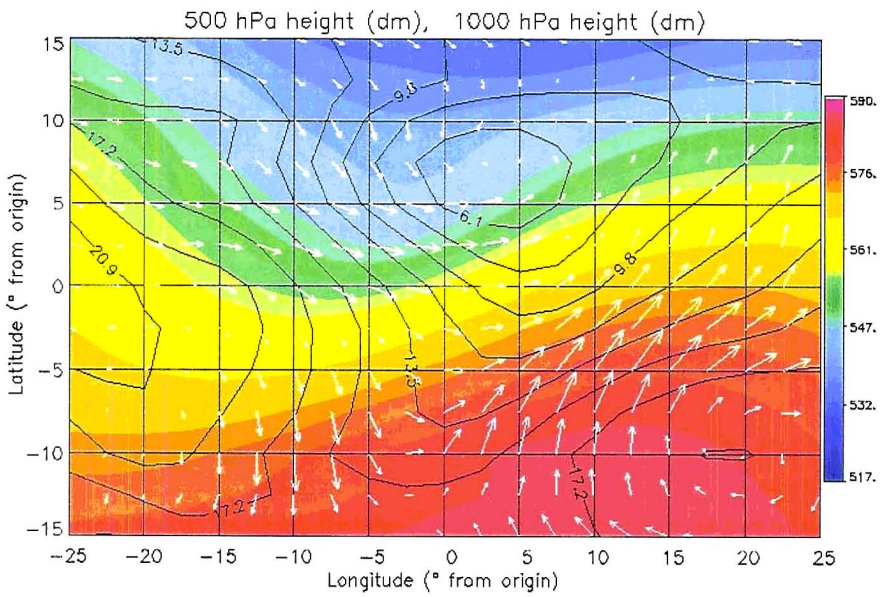

Figure 2-9: Composite 500 hPa height (colored contours) and 1000 hPa height, both in dm. The 1000 hPa height may be regarded as a proxy for surface pressure. Wind vectors are 1000 hPa wind.

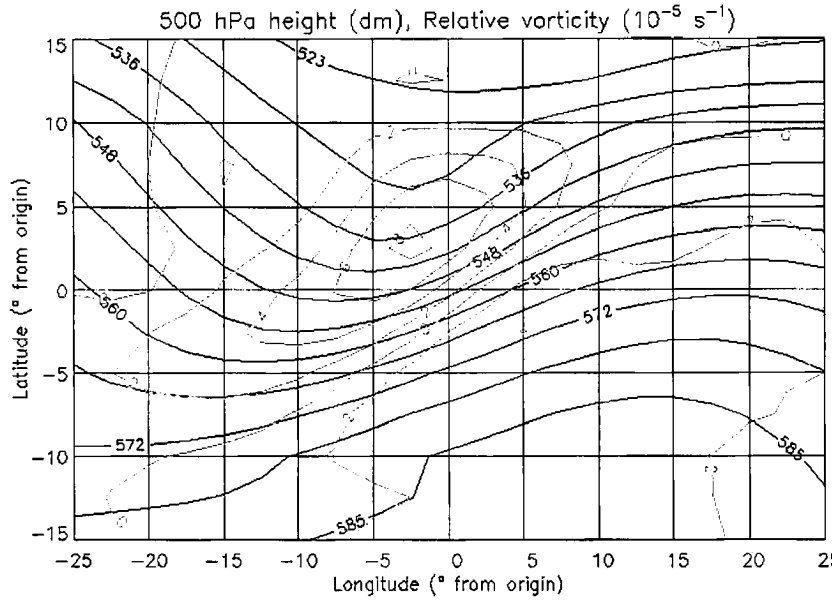

Figure 2-10: Composite 500 hPa height in dm and horizontal relative vorticity in 10^{-5} s^{-1}.

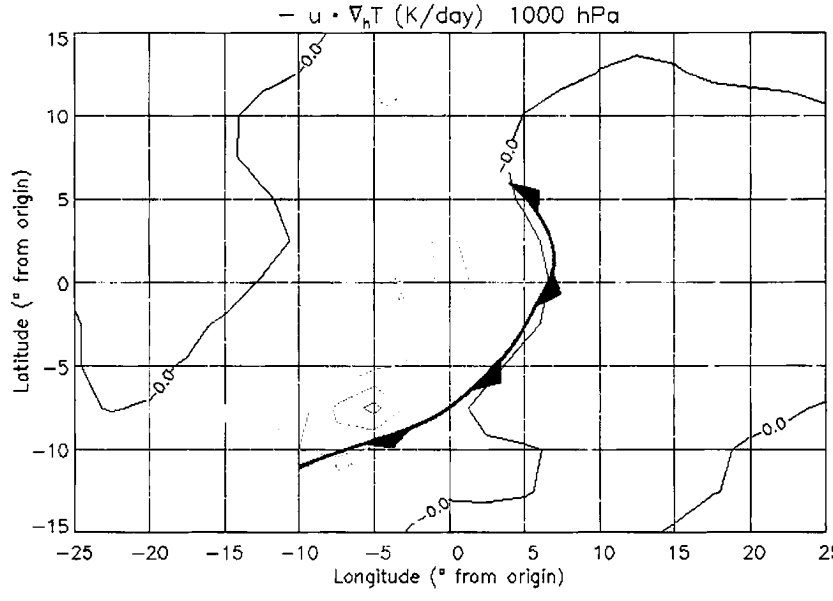

Figure 2-11: Composite 1000 hPa temperature advection ($-\vec{u} \cdot \nabla_h T$) expressed in Kelvin per day. Cold advection is shown in shades of blue, and warm advection is shown in shades of red. The superimposed front is derived from the 1000 hPa height field and is derived independent of temperature advection.

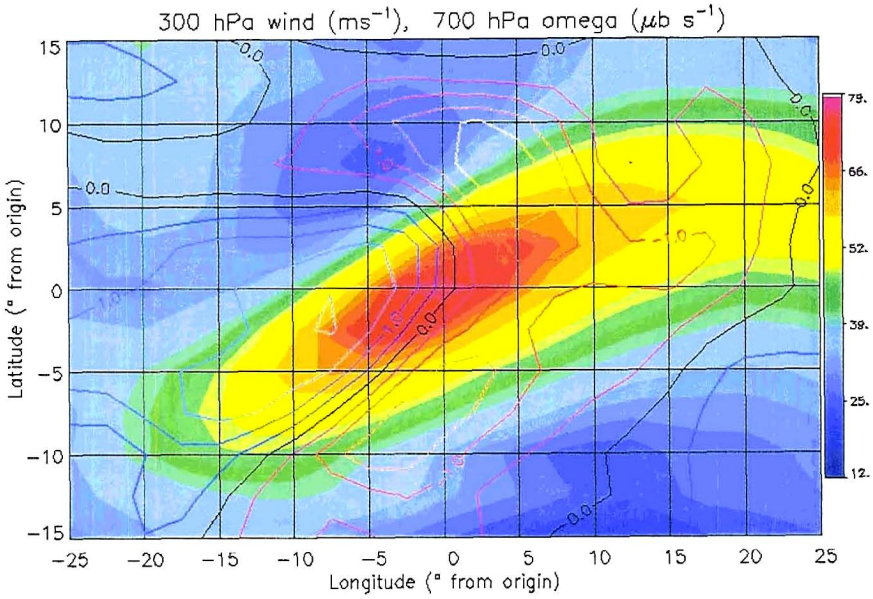

Figure 2-12: Composite 700 hPa pressure velocity, ω, in μb s^{-1} superimposed on the 300 hPa wind field in ms^{-1} (shaded contours). Upward motion is shown in shades of red, and downward motion is shown in shades of blue.

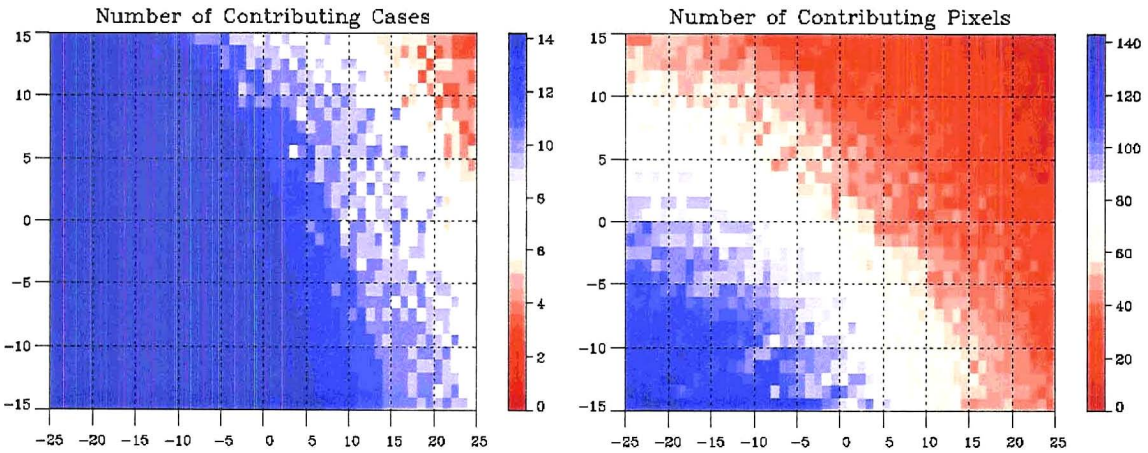

Figure 2-13: Total number of key dates contributing to each 1° by 1° pixel in the composite case (left panel), and total number of ISCCP DX pixels contributing to the same (right panel). Note that a maximum of 14 key dates can contribute to the composite case.

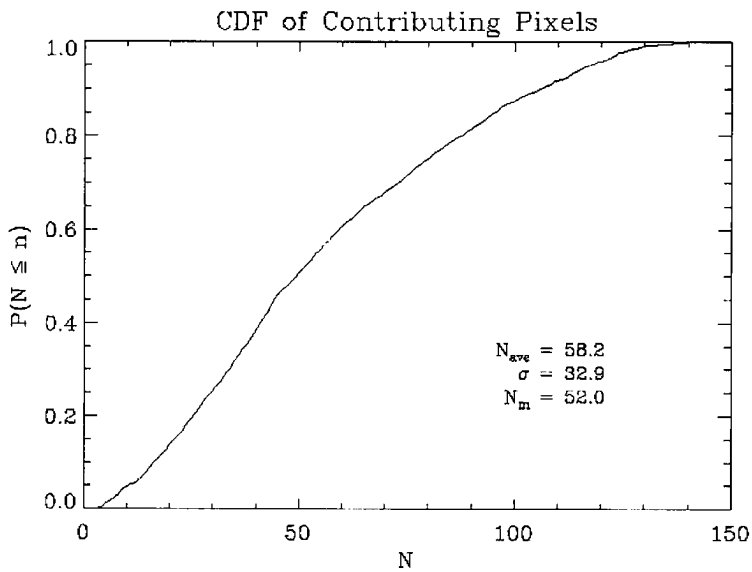

Figure 2-14: Cumulative probability function of total number of DX data set pixels that contribute to the final composite.

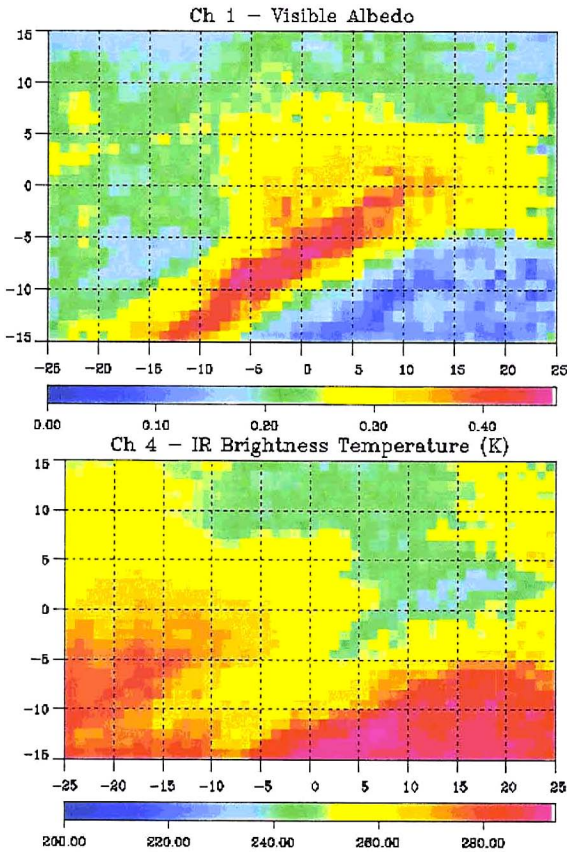

Figure 2-15: Composite visible albedo (channel 1, top panel), and longwave infrared brightness temperature in K (channel 4, bottom panel).

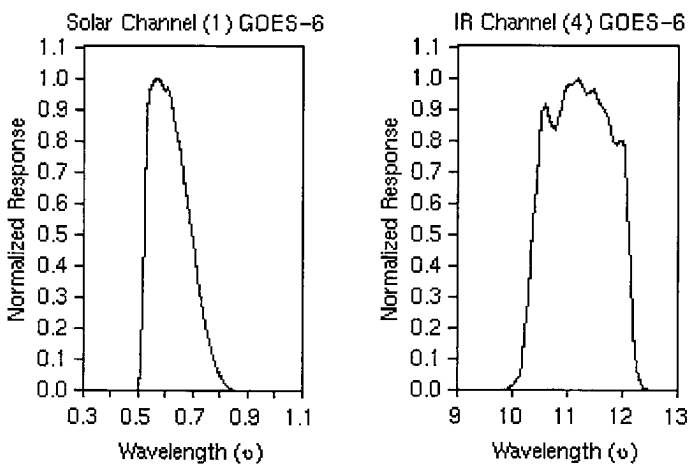

Figure 2-16: Spectral response functions of GOES-6 channel 1 (visible) and channel 4 (longwave infrared). From ISCCP GOES-6 documentation.

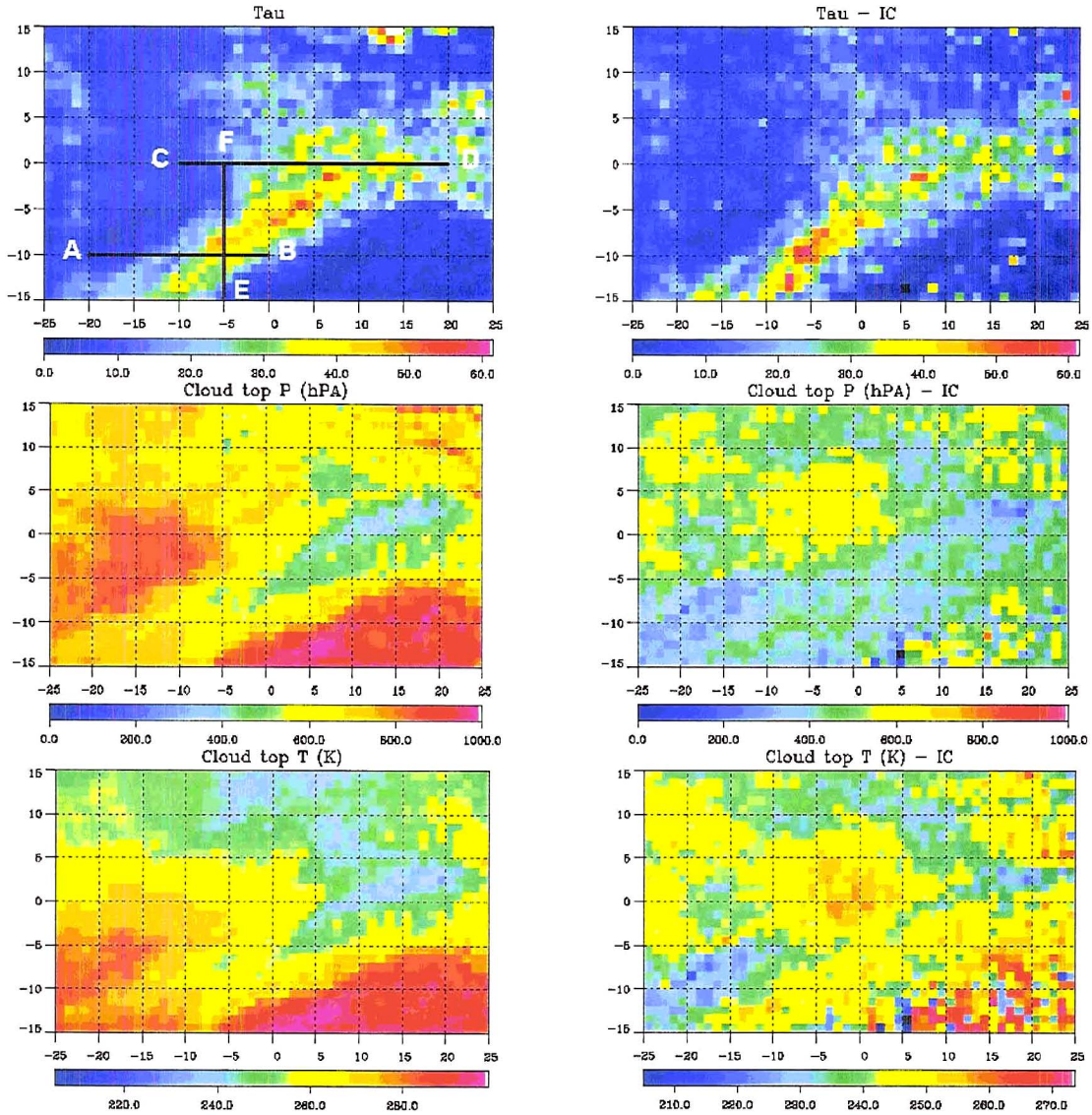

Figure 2-17: Composite pattern of optical depth (top panel), cloud top pressure in hPa (middle panel), and cloud top temperature in K (bottom panel). The left are Method 1, or uncorrected, quantities. The right are Method 2, with the ice cloud correction. In addition, the top left figure shows the location of cross sections referenced in Section 2.5.3.

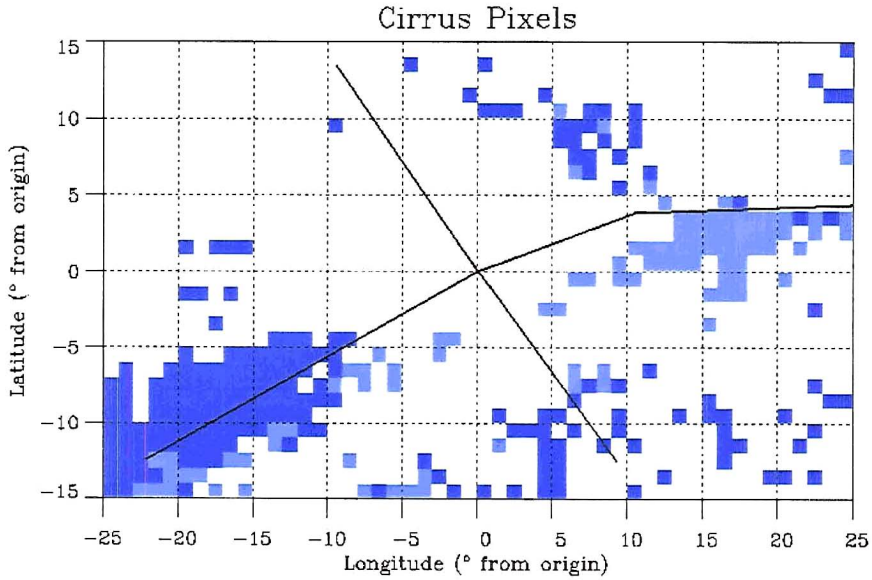

Figure 2-18: Cirrus location from the Method 2 composite. Highlighted areas have cloud top pressure and temperature less than 400 hPa and 240 K, respectively. Darker blue pixels have a Method 2 optical depth of less than 15, while lighter blue pixels have an optical depth of 15 or greater. Solid lines show approximate location of jet axis and division between accelerating and decelerating regions.

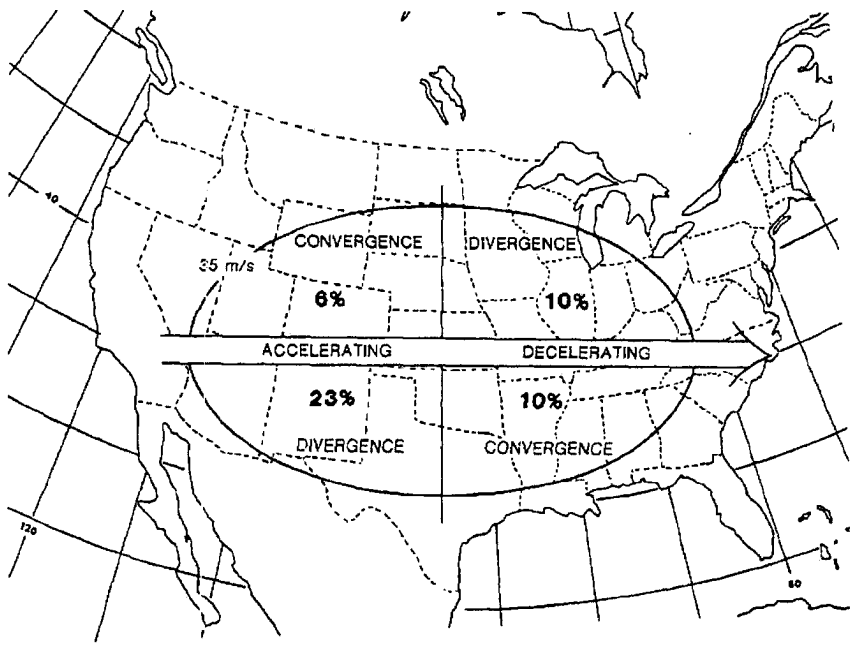

Figure 2-19: From the study by Menzel et al. (1992), provided for comparison. The distribution of cirrus around jet cores for January-February 1986 and January 1988. Percentages indicate the fraction of all cirrus inside each quadrant based on the total amount of cirrus both inside and outside the jet.

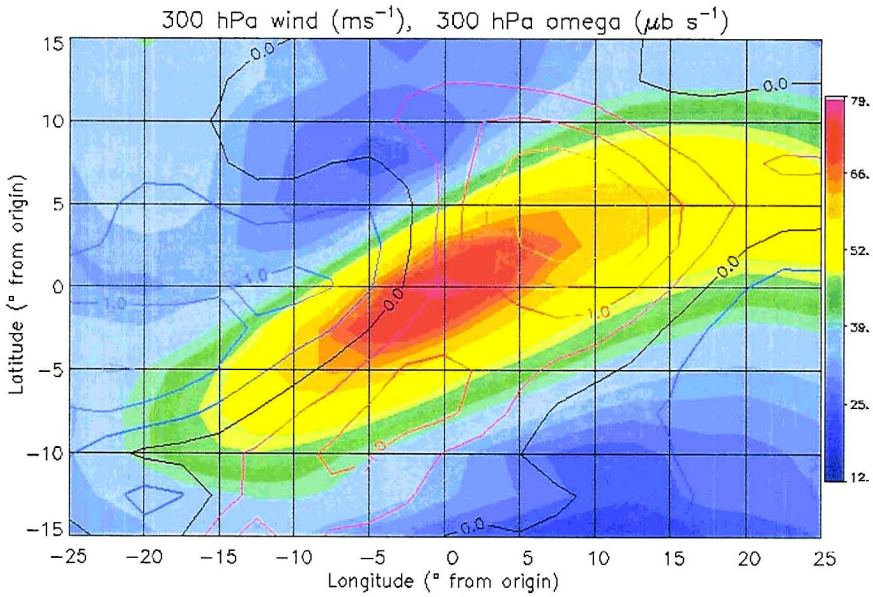

Figure 2-20: Composite 300 hPa pressure velocity, ω, in μb s^{-1} superimposed on the 300 hPa wind field in ms^{-1} (shaded contours). Upward motion is shown in shades of red, and downward motion is shown in shades of blue.

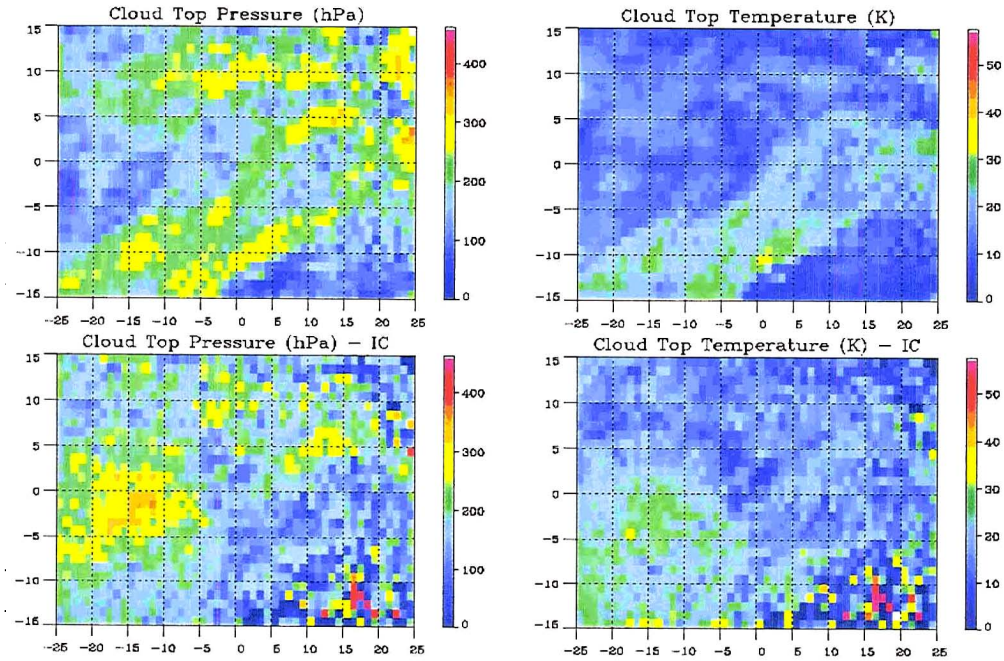

Figure 2-21: Standard deviation of composite cloud top pressure (hPa) (left) and cloud top temperature (hPa) (right). Method 1, or uncorrected at top and Method 2, or corrected values at bottom.

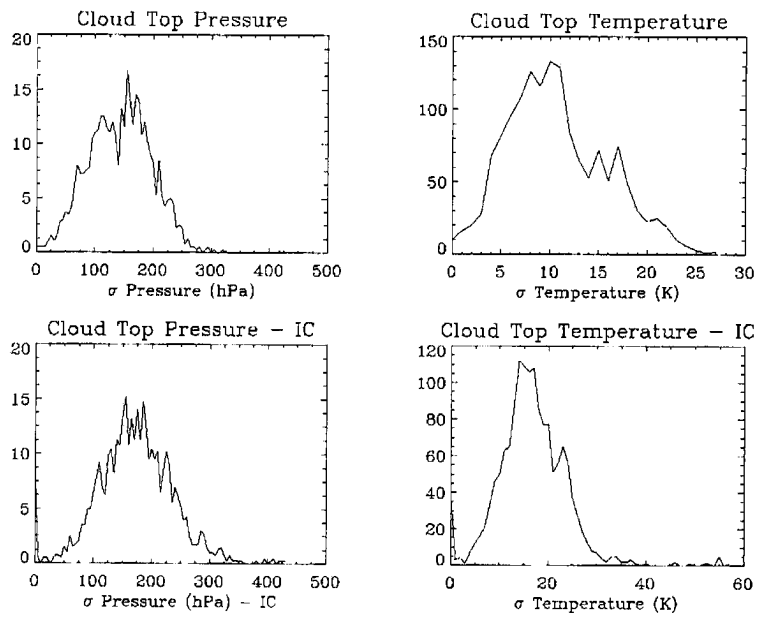

Figure 2-22: Probability density function of standard deviations of cloud top pressure (hPa) (left) and cloud top temperature (hPa) (right). Method 1, or uncorrected at top and Method 2, or corrected values at bottom.

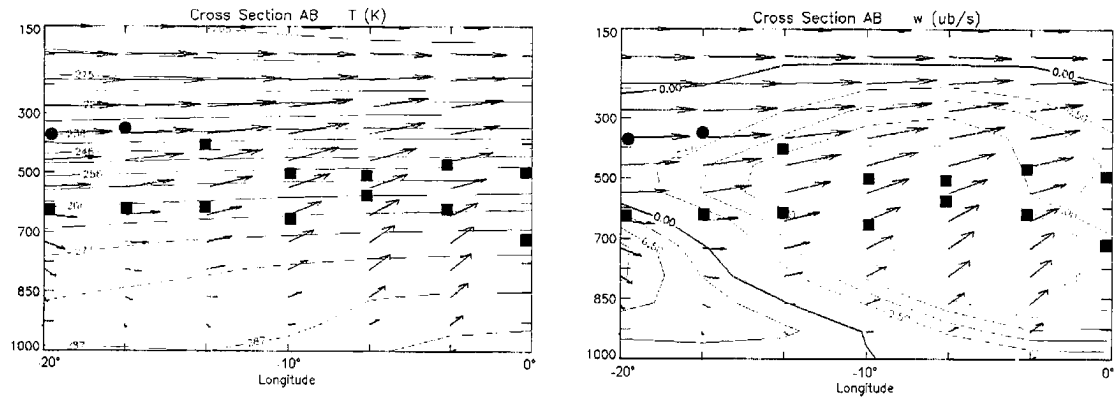

Figure 2-23: Cross section across AB along –10° latitude (see Figure 2-17). Contours of temperature (K) at left and vertical pressure velocity (μb s^{-1}) at right. ISCCP-derived cloud tops are shown as black dots (Method 1) and blue dots (Method 2). Vectors depict flow in the plane that is parallel to the cross section.

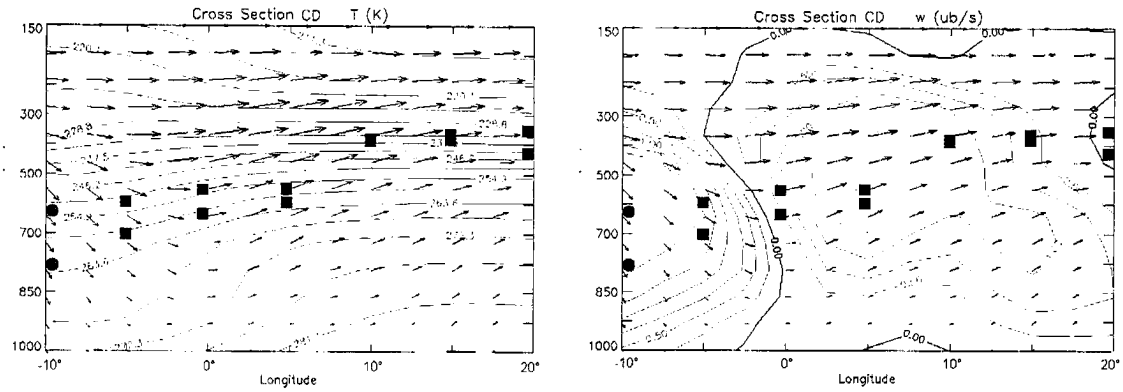

Figure 2-24: As in Figure 2-23, except for cross section CD along 0° latitude.

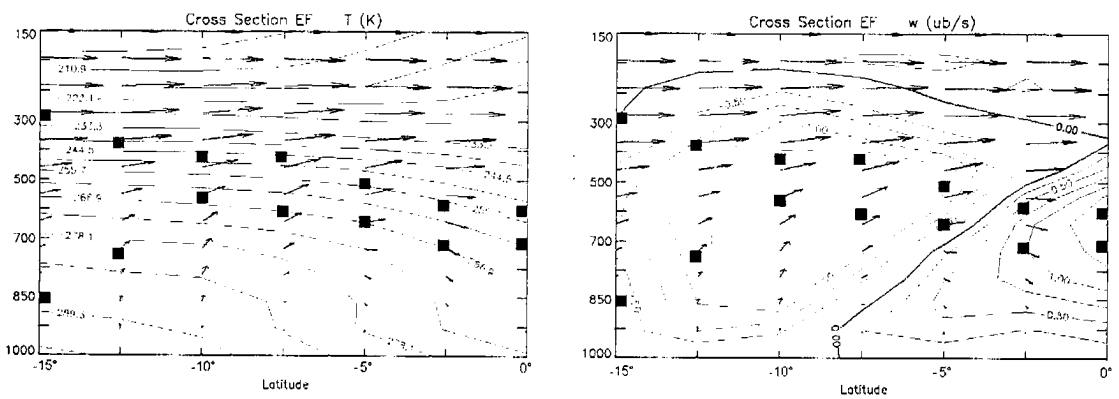

Figure 2-25: As in Figure 2-23, except for cross section EF along –5° longitude.

This page intentionally blank.

Chapter 3

3. CLOUD RADAR AND ASSOCIATED PRODUCTS

3.1 Introduction

The focus thus far has been on obtaining a large scale picture of the cloud system and dynamics that surround a strong southwest to northeast oriented jet stream over the continental United States. Having painted the bigger picture in the previous chapter, the second portion of the study will now focus more closely on the jet stream cirrus shield itself and its microphysical properties. The principle tool used in this investigation is the Ka-band cloud radar located at the Atmospheric Radiation Measurement (ARM) program's Southern Great Plains (SGP) site. This radar has sufficient sensitivity for detection of even tenuous cirrus cases over the SGP site.

Following this study of cloud structure and microphysics, there will be further investigation of the connection between cloud structure revealed by the cloud radar and the large-scale dynamics.

3.2 MMCR Radar Description

The cloud radar used in this study is the Millimeter Wave Cloud Radar (MMCR), operational near the Kansas-Oklahoma border at ARM's SGP site since 1996. The MMCR is a vertically pointing coherent radar that operates at a frequency of 35 GHz (8.66 mm). This operating frequency presents a balance between the competing ideals of observing cloud-sized particles and minimizing radar attenuation (Clothiaix et al., 1999). Radar targets are best observed using a radar wavelength comparable to the intended target, but beam attenuation by hydrometeors increases significantly toward smaller wavelengths. This is an example of one of many tradeoffs faced by radar meteorologists, such as maximum unambiguous range versus maximum unambiguous velocity. The choice of 35 GHz is a common one for cloud radars, another common choice being 94 GHz, and represents a reasonable tradeoff between these two competing effects.

In normal operation, the radar cycles through four operating modes (Clothiaux et al., 2000). Each of these modes slightly varies the primary radar operating parameters; the synthesis of these modes provides a more detailed view of cloud structure than any individual mode. Parameters that are varied as the radar cycles between modes include the number of range sample volumes, range sample volume spacing, pulse width, interpulse period, number of coded bits, number of coherent averages, number of spectra averaged, number of fast Fourier transform points, and radar receiver downtime.

Mode 1, the stratus mode, has high sensitivity and vertical resolution for observing boundary-layer clouds. Mode 2, the cirrus mode, has the highest sensitivity, and is the best suited for observing high, tenuous cirrus clouds. Mode 3, the general mode, is used for detecting a wide variety of hydrometeors. Mode 4, the robust mode,

has the lowest sensitivity, but is virtually free of radar artifacts. The higher sensitivity of modes 1 and 2 is provided by a phase-coded pulse compression method.

Pulse compression is a well-established technique, originally used in military applications, that results in a finer range resolution and improved hydrometeor detection over a traditional system (Mudukutore et al., 1998). The beamwidth of the transmitted pulse is increased by coding it in either phase or frequency. The peak power of the coded pulsed is increased by a factor of the compression ratio:

$$C = B\,T = \frac{T}{\tau} \tag{3.1}$$

where B is the waveform bandwidth, T is the transmitted pulse length, and τ is the effective compressed pulse length. In the case of MMCR Mode 2 operation, 32 phase-coded bits are employed for each radar pulse. One tradeoff with use of pulse compression is the tendency to detect radar sidelobes which tend to blur the returns from neighboring range gates.

This study makes use of Mode 2 data (the cirrus mode). Mode 2 is best suited for cirrus studies because of the use of phase-coded pulse compression and a relatively large pulse length (600 nm). The combination of these parameters yields a minimum detectable reflectivity of –50 dBZ up to approximately 8 km, and –45 dBZ up to approximately 15 km. The useful range of the radar in this mode allows hydrometeor detection for altitudes of approximately 3.0 to 15.0 km above the radar.

3.3 MMCR Data Sets

Radar data obtained from the ARM data archive include the first three radar moments: equivalent reflectivity factor (hereafter referred to as reflectivity for simplicity), Doppler velocity, and Doppler spectral width. These data are placed onto a grid with 90 m vertical resolution and approximately 1.5 min temporal resolution.

One significant problem with the use of phase-coded pulses is the beam sidelobe artifacts that often results. These data are cleaned using an algorithm developed by Clothiaux et. al 1999) to remove radar noise and other artifacts. This method makes use of radar data from all four modes to detect those features that are likely to be artifacts. For example, features that do not appear in the Mode 4 (robust mode) data but occur within the lower 10 km of the atmosphere may be flagged as clutter. The result is typically the elimination of clutter surrounding cloud edges, as well as removal of non-meteorological targets within the boundary layer.

3.4 Bulk Properties from Power Law Relations

A cloud radar is, in its stand-alone form, a useful research tool. Reflectivity data can be used to detect cloud edges and examine the structure of clouds and precipitation. Reflectivity alone can be used to estimate other quantities of meteorological interest. Relationships exists, mostly in power-law form, that describe the relationship between reflectivity and quantities such as liquid water content, ice water content, and particle diameter. These relationships are all of the general form:

$$R = a\, Z^{b} \tag{3.2}$$

where R is the quantity to be estimated, and a and b are coefficients that are determined from observations or models. This is a simple linear relation when the logarithm is taken:

$$\log R = \log a + b \log Z \tag{3.3}$$

Here, the slope of the line is b and the R-intercept is given by the logarithm of a. Determining a best-fit line to this equation determines these coefficients.

Since quantities like liquid water content, ice water content, and drop diameter tend to follow the form of Equation 3.2, much work has been done to determine the coefficients a and b by fitting of in situ observations. Several examples of common IWC-Z relationships, which are of particular interest in cirrus cloud research, are given in Table 3-1.

Table 3-1: Common IWC-Z relationships of the form IWC = a Z^b from various publications.

Publication	IWC-Z Relationship
Sassen et al. (1987) (I)	IWC = 0.12 $Z^{0.696}$
Sassen et al. (1987) (II)	IWC = 0.037 $Z^{0.7}$
Liu and Illingsworth (2000)	IWC = 0.097 $Z^{0.59}$
Sassen and Liao (1996)	IWC = 0.027 $Z^{0.78}$
Atlas et al. (1995)	IWC = 0.064 $Z^{0.58}$

These relations are plotted in Figure 3-1. It is clear that the spread of IWC for a given reflectivity can be an order of magnitude, or even two orders of magnitude for small reflectivities, using IWC-Z relations alone. For example, at a reflectivity of –20 dBZ, the estimated ice water content for the five relationships shown in Figure 3-1 varies from 7.4 x 10^{-4} to 6.4 x 10^{-3} g m^{-3}. This is generally too wide a variance for research purposes;

further, no uncertainties can be assigned to these values of ice water content. The challenge of selecting a IWC-Z relation from the list, when each relationship is specific to a specific case or set of cases, is no trivial matter.

IWC-Z relationships are derived from certain climatologies or cloud regimes, and application of one relationship to a different subset of clouds can introduce large inaccuracies in the estimation. Sometimes, these relations fail to produce reasonable results even when applied to what seems to be a nearly identical case for which the relation was derived. Some of these discrepancies are due to differences in the assumed ice particle density and the radar wavelength used, as noted by Liao and Illingworth (2000). Variation of the ice crystal habits and fall orientation can also cause discrepancies. Liao and Illingworth attempted to classify radar returns according to temperature, and noted a modest improvement in the quality of IWC-Z relations.

For more advanced studies, it seems, it is necessary to look beyond radar-only methods of cloud property determination, an incorporate other measurements. Several such methods have emerged in the last decade. Matrosov (1999) describes a method to retrieve IWC and cloud particle sizes using a K_a-band Doppler radar and a narrowband infrared radiometer, whereby the coefficients of the Z-IWC relationship are tuned for each radar profile. This tuning is a function of cloud ice-water path, determined from independent estimates of cloud optical depth and radar reflectivity. Mace et al. (1998) have developed a method that combines radar reflectivity and infrared emission spectra derived from an interferometer to retrieve similar parameters.

This study makes use of another new technique, based on a combination of radar reflectivity and an estimate of column optical depth. This algorithm, introduced in the

next chapter, is formulated in an optical estimation framework, and therefore provides estimates of uncertainties in the quantities that are retrieved, as well as diagnostics that evaluate the performance of the retrieval.

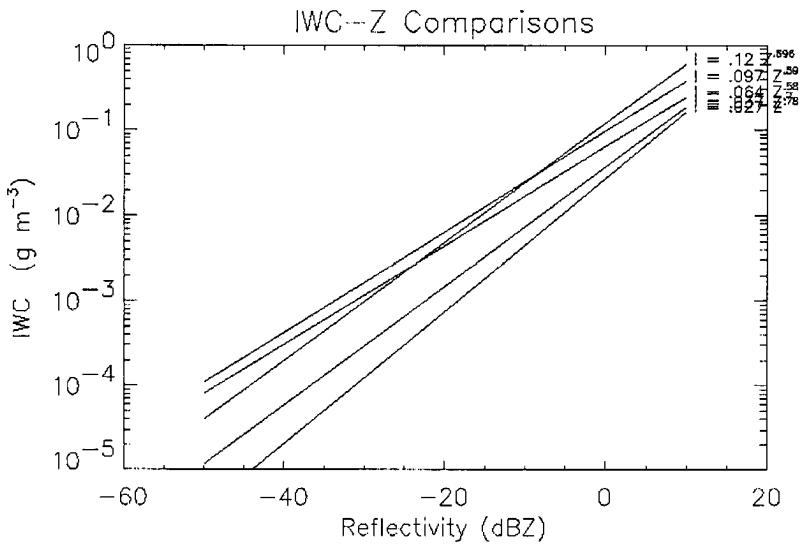

Figure 3-1: IWC-Z relationships of Table 3-1. Demonstrates the variability of these relationships.

This page intentionally blank.

Chapter 4

4. RADAR RETRIEVAL OF CLOUD PROPERTIES

4.1 Introduction to the Tau-Z Retrieval

It is clear that power law relations alone are insufficient to characterize the microphysical properties of the clouds of interest in this study. These power law relations have been derived for specific regimes, and one could easily derive a new relation for each cloud regime that is observed. Variations of these relations for a specific set of conditions can also be large. The problem, of course, is that the system has more variables than can be easily accounted for in such a simple relation.

This study makes use of and expands upon the proposed Cloudsat algorithm for retrieval of cloud microphysical parameters. Cloudsat, a research satellite scheduled to be launched in 2004, will fly a 94 GHz cloud radar that will be capable of viewing a wide variety of clouds, from thin cirrus to precipitating thunderstorms. The input parameters to the algorithm are cloud reflectivity, which is a function of radar range gate and time, and an estimate of column cloud visible optical depth.

Information on the nature of the cloud reflectivity and optical depth data, as used in this study, is presented in the next chapter which deals with the case studies.

4.2 Fundamentals of the Retrieval

The basis of this retrieval is the work of Rodgers (1976, 1990) and Marks and Rodgers (1993). These fundamental papers are widely credited for bringing the mathematical concept of estimation theory, as it applies to the inversion problem, to the atmospheric science community.

The inverse problem is essentially a problem of detective-work: given a set of outcomes, or observations, is it possible to determine the set of conditions that led to these outcomes? Consider a deer that leaves a set of tracks in the forest. A hunter happens across the tracks and wonders what kind of animal left them. This is the nature of the inverse problem; given a set of observations (the animal tracks), the inverse problem seeks to determine what set of physical conditions (the deer) contributed to what has been observed. By carefully examining the characteristics of the tracks, the hunter may be able to determine that a deer, and not an elk or wolf, left behind the tracks that they have observed.

However, suppose our hunter, for reasons of poor vision or incomplete knowledge of the problem, is not able to distinguish between the tracks of a deer and an elk. He will need to rely on some other information about the problem. This information is called a priori information, and it is used to constrain the solution to a set of values that might reasonably be observed in nature. If the hunter discovers the tracks in Louisiana, he knows that there are no elk to be found nearby, and this information allows him to focus his search on deer and other animals with similar tracks. An example of the use of a priori information in an atmospheric retrieval is the determination of the vertical tropospheric water vapor profile from satellite measurements; the a priori information

might be a nearby radiosonde profile or climatic values of water vapor in the troposphere for the region of interest.

Formulated mathematically, the problem can be expressed in terms of a forward model, F:

$$y = F(x,b) + \varepsilon_y \tag{4.1}$$

The forward model relates the parameter to be retrieved to the measurements or observations that are made. Here, y is a vector that represents the measurements and x is the vector of parameters to be retrieved, sometimes referred to as the state vector. The vector b includes parameters that affects this relationship but are not themselves retrieved, and ϵ_y represents the error in the forward model and the measurements.

Thus, accurate characterization of the forward model, which relates the parameters to be retrieved to the observations, is essential. The forward model will always be an approximation to *nature's forward model*, the actual physical laws that govern the system of interest. This is one source of error introduced into the retrieval. Furthermore, there is always some error associated with the measurements. As will become apparent, although minimization of the error is important where possible, it is equally important to characterize the errors that are a necessary component of the problem as it is posed. Using Bayes theorem and Gaussian statistics, the retrieval seeks to find the most probable state of the atmosphere given the measurements and a priori information. This most probable solution is expressed mathematically by the minimization of a quadratic cost function, J (Rogers, 1990):

$$J = (x - x_a)^T S_a^{-1} (x - x_a) + (y - F(x,b))^T S_y^{-1} (y - F(x,b)) \tag{4.2}$$

A priori information is introduced in the terms x_a and S_a. Here x_a is a vector of a priori values that are used to constrain the solution to a set of physically realistic values. The a priori covariance matrix is given by S_a, whose diagonal elements contain the uncertainty (variance) in the a priori values. The off-diagonal elements contain covariances between the various a priori values. The matrix S_y characterizes the uncertainties in the measurements, and covariance between the measurements. The values of these vectors and matrices in terms of the tau-Z retrieval will be more fully developed in Section 4.3.

The cost function, J, is minimized via an iterative solution given by:

$$x^{i+1} = (S_a^{-1} + K^{iT} S_y^{-1} K^i)^{-1} [S_a^{-1} x_a + K^{iT} S_y^{-1} (y - F(x^i) + K^i x^i)] \tag{4.3}$$

where K represents the partial derivative of the forward model with respect to the retrieved quantity:

$$K = \frac{\partial F(x,b)}{\partial x} \tag{4.4}$$

The matrix quantity A, also called the averaging kernel, is given by:

$$A = S_x (K^{iT} S_y^{-1} K^i) \tag{4.5}$$

The significance of this diagnostic quantity is discussed below. Using this definition, Equation 4.3 can be written as follows:

$$x^{i+1} = x^i + A K^{i-1} (y - F(x^i)) + (I - A)(x_a - x^i) \tag{4.6}$$

where I is the identity matrix. The error covariance matrix relative to the retrieved quantities is then given by:

$$S_x = (S_a^{-1} + K^T S_y^{-1} K)^{-1} \tag{4.7}$$

Clearly, these errors are dependent on errors in the a priori assumptions and the errors in the measurements and forward model.

Looking at Equation 4.6, it is evident that the A matrix provides information as to how heavily the final optimum solution,

$$\hat{x} = x^{i+1} \mid i_{final\ value}, \tag{4.8}$$

relies on the a priori information. When the A matrix equals the identity matrix, I, the final term in Equation 4.6 goes to zero, meaning that x_a does not contribute to the estimate of x. In other words, in a perfect retrieval, A would approach the identity matrix, indicating that the retrieved parameter x relies only on the measurements and not on the a priori information. The more A departs from I, the more the retrieved quantity depends on the a priori assumptions. The sensitivity of the retrieval to changes in the a priori parameter is sometimes expressed as the diagnostic parameter D_a:

$$D_a = I - A \tag{4.9}$$

Though the best possible retrieval would be the true values of the parameters of interest, this is not an attainable goal in the real world. A priori information must be included in the problem to constrain our best estimate of x to reasonable values. The inclusion of a priori information ensures greater stability by constraining the solution and "pulling" the retrieval toward more physically realistic values (Rodgers, 1976). This is especially useful when there are not enough measurements, or the measurements are not of high quality.

The solution as given by Equation 4.6 is determined iteratively by repeating the calculation until the solution converges, as given by some convergence criteria. The convergence criterion used in this retrieval is that given by Marks and Rodgers (1993):

$$\Delta x^T S_x^{-1} \Delta x \quad << \quad n \tag{4.10}$$

where $\Delta x = x^{i+1} - x^i$ and n is the number of dimensions of the state vector. In the rare instances when the solution space and model space do not intersect, no estimate of x any better than the a priori can be obtained by this method.

4.3 The Forward Model

The size spectra of ice crystals is assumed to follow the gamma distribution, with the ice crystals considered as spheres of diameter D (Tripoli et al., 1988):

$$n(D) = N_t \frac{1}{\Gamma(\nu)} \left(\frac{D}{D_n} \right)^{\nu-1} \frac{1}{D_n} \exp\left(-\frac{D}{D_n} \right) \tag{4.11}$$

where D_n is the characteristic diameter, N_t is the total number of ice crystals of all sizes in a given volume, and ν is the width parameter of the gamma distribution. The assumptions that ice particles are spheres and follow this single-peaked distribution are arguably the greatest contributors to the error into the forward model.

A useful property of the gamma distribution in this form is the characterization of the moment p in terms of the following integral using the gamma function, Γ:

$$\int_0^\infty D^p n(D) dD = \frac{\Gamma(\nu + p)}{\Gamma(\nu)} N_t D_n{}^p \tag{4.12}$$

The three parameters of the gamma distribution, number concentration, characteristic diameter, and distribution width, are in principle functions of both height and time. If each radar data time step consisted of m height gates, then 3m measurements would be needed to perform the retrieval (one corresponding to each of these parameters).

In this case, however, only m + 1 measurements are available for each time step, consisting of m reflectivity measurements and one inferred estimate of cloud visible optical depth. This means that some assumptions must be made to reduce the number of unknowns in the problem such that it does not exceed the number of measurements.

To this end, it is assumed that the width of the distribution is constant with height, and ν is set equal to 2 following Dowling and Radke (1990) who derived this value from in situ cirrus measurements. Furthermore, the ice crystal number concentration is assumed to be constant with height and is set to the mean value of column-averaged number concentration, $\overline{N}_t$. This value of $\overline{N}_t$ is then retrieved along with ice crystal characteristic diameter at each radar height gate. The assumption that the ice crystal number concentration is constant with height is likely to be poor when microphysical processes, such as ice crystal nucleation or aggregation, occur preferentially at one vertical level over another. It also is likely to lead to spreading the vertical gradients of particle size and concentration, as is demonstrated in Chapter 4.4.

For the purpose of mathematical simplification, it is actually the logarithm of these quantities that is retrieved, making the state vector:

$$x = \begin{bmatrix} \log D_{n,1} \\ \log D_{n,2} \\ \vdots \\ \log D_{n,m} \\ \log \overline{N}_t \end{bmatrix} \tag{4.13}$$

The vector of measurements is given by:

$$y = \begin{bmatrix} Z_1 \\ Z_2 \\ \vdots \\ Z_m \\ \tau \end{bmatrix} \tag{4.14}$$

with reflectivity expressed in dBZ.

4.3.1 Basic Quantities of the Retrieval

Four basic quantities that form the basis of the retrieval must be defined: radar reflectivity, volume extinction coefficient, ice water content, and optical depth. In this study, it is assumed that all targets are Rayleigh scatterers, or can be scaled to act as Rayleigh scatterers through Mie calculations, as will be discussed below. This assumption demands that the following condition is met:

$$x = \frac{\pi D}{\lambda} \ll 1 \tag{4.15}$$

The size parameter, x, is defined in terms of some characteristic particle diameter, D, and the radar wavelength, λ. Since the MMCR radar wavelength is 8.66 mm, this requires that the characteristic particle size be much less than 1.33 mm. This condition, as will be shown, is generally met for the case of jet stream cirrus, which are often quite thin and tenuous. In cases where this condition is not met, a Mie correction is applied to make the particles "effective" Rayleigh scatterers.

As Rayleigh scatters, ice crystals obey the radar equation as defined by:

$$Z_{ray} = \int_0^\infty D^6 n(D) dD \tag{4.16}$$

where Z_{ray} is the Rayleigh radar reflectivity factor. Radar reflectivity is related to the sixth moment of drop diameter. To accommodate those cases when scattering falls outside the Rayleigh regime, code provided by Bohren and Huffman (1983) is used to calculate an equivalent Mie reflectivity, Z_{Mie}. Figure 4-1 shows the ratio of Z_{Mie} to Z_{Ray} as a function of size parameter (solid line) along with a Gaussian analytical fit (dotted line). For small size parameters, Z_{Mie} is equivalent to Z_{Ray}; this is the Rayleigh regime. For larger values of size parameter, however, the Z_{Mie} is considerably less than Z_{Ray}. The analytical fit is given by:

$$f_{Mie}(x) = c_0 \exp^{-0.5((x-c1)/c2)^2} + c_3 + c_4 x + c_5 x^2 \tag{4.17}$$

where c_0, c_1, c_2, c_3, c_4, and c_5 are coefficients of the fit. This complete Mie solution is represented by an infinite series whose coefficients are Bessel functions. They can thus be expressed as polynomials in x and fitted with the functional form of Equation 4.17. Thus, the new expression for reflectivity, including Mie scattering effects, can be written as:

$$Z = Z_{Ray} f_{Mie}(D_n) \tag{4.18}$$

It is noteworthy that this correction is usually very small. Applying the integral property of the gamma distribution given by Equation 4.12, radar reflectivity can then be expressed as:

$$Z = \frac{\Gamma(6+\nu)}{\Gamma(\nu)} \overline{N}_t D_n^{\ 6} f_{Mie}(D_n) \tag{4.19}$$

Simple calculations with assumed typical drop size distributions show that the MMCR radar should see even very small ice crystals, on the order of 10 μm, given a

minimum detectable signal on the order of –50 dBZ. This indicates that a bias against ice-crystals of relatively small mass should be minimal.

The visible extinction coefficient is defined by:

$$\begin{aligned}\sigma_{ext} &\equiv \int_0^\infty \pi Q_{ext} r^2 n(r) dr \\ &= \frac{\pi}{4} \int_0^\infty Q_{ext} D^2 n(D) dD\end{aligned} \tag{4.20}$$

where Q_{ext} is the extinction efficiency. For visible wavelengths, the extinction efficiency is known to approach a constant value of two as the size parameter becomes sufficiently large, perhaps on the order of 10 to 100, and this convenient assumption is made in the retrieval (Stephens, 1994). Thus, taking $Q_{ext} = 2$ and applying Equation 4.12, the extinction coefficient is written as the second moment of ice crystal diameter:

$$\sigma_{ext} = \frac{\pi}{2} \frac{\Gamma(2+\nu)}{\Gamma(\nu)} \overline{N}_t D_n^{\,2} \tag{4.21}$$

The next parameter of interest is the visible optical depth, defined as:

$$\tau = \int_{z_b}^{z_t} \sigma_{ext}(z) dz \tag{4.22}$$

where z_b refers to cloud bottom and z_t refers to cloud top. The optical depth can also, of course, be written in terms of gamma distribution using Equation 4.21:

$$\tau = \frac{\pi}{2} \frac{\Gamma(2+\nu)}{\Gamma(\nu)} \int_{z_b}^{z_t} \overline{N}_t D^2 dz \tag{4.23}$$

The integral term of Equation 4.23 must be approximated by a summation. In this case, the trapezoidal approximation is used, leading to the following final expression for visible optical depth:

$$\tau = \frac{\pi}{2}\frac{\Gamma(2+\nu)}{\Gamma(\nu)}\overline{N}_t\left[\frac{1}{2}\left(D_{n,1}^2 + D_{n,m}^2\right)\Delta z + \sum_{j=2}^{m-1} D_{n,j}^2\,\Delta z\right] \tag{4.24}$$

where Δz is 90 m, the constant vertical spacing between radar range gates.

The final parameter of interest, that is calculated after the retrieval is complete, is the ice water content (IWC) of the cloud. The ice water content of a given volume is defined by the integral of the product of the particle mass distribution, m(D), and number concentration, taken over all possible particle sizes. Assuming spherical ice crystals of bulk ice density ρ_i, this can be expanded as:

$$\begin{aligned} IWC &= \int_0^\infty m(D)n(D)dD \\ &= \int_0^\infty \rho_i \frac{4}{3}\pi\left(\frac{D}{2}\right)^3 n(D)dD \\ &= \frac{\pi}{6}\int_0^\infty \rho_i D^3 n(D)dD \end{aligned} \tag{4.25}$$

Thus, ice water content is related to the third moment of ice crystal diameter. Applying the gamma size distribution,

$$IWC = \frac{\pi}{6}\rho_i \frac{\Gamma(3+\nu)}{\Gamma(\nu)}\overline{N}_t D_n^{\,3} \tag{4.26}$$

4.3.2 Processing the Retrieval

The retrieval begins by initializing the vector x_1 with the a priori vector, x_a. The a priori value of characteristic diameter at vertical level j is to set to $D_{a,j}$. The a priori value of mean number concentration is assigned to N_{ta}. The a priori vector is then:

$$x_a = \begin{bmatrix} \log D_{a,1} \\ \log D_{a,2} \\ \vdots \\ \log D_{a,m} \\ \log N_{ta} \end{bmatrix} \tag{4.27}$$

Since no in situ information is available for any of the cases of interest, some average, physically reasonable values are specified as the a priori. In this study, $D_{a,j}$ is given a value of 100 μm for all vertical levels, and N_{ta} is assigned a value of 10^3 m^{-3}. These are known typical values for cirrus clouds.

It is also necessary to specify uncertainties in the a priori assumptions and the measurements. Given an uncertainty in characteristic diameter of $D_{err,j}$ for level j and an uncertainty in mean number concentration of N_{err}, the S_a matrix is given by:

$$S_a = \begin{bmatrix} \log D_{err,1} & 0 & 0 & 0 & 0 \\ 0 & \log D_{err,2} & 0 & 0 & 0 \\ 0 & 0 & \ddots & 0 & 0 \\ 0 & 0 & 0 & \log D_{err,m} & 0 \\ 0 & 0 & 0 & 0 & \log N_{err} \end{bmatrix} \tag{4.28}$$

Note it is assumed that there is no covariance between levels, so the diagonal elements are set to zero. In this study, $D_{err,j}$ is taken to be the same for all vertical levels, and is assigned a value of 100%. The uncertainty in mean number concentration is also taken to be 100%. These values thus reflect the lack of confidence in the a priori knowledge of the problem.

The measurement covariance matrix is defined similarly, assuming an uncertainty in reflectivity of $z_{err,j}$ for level j and an uncertainty in optical depth of τ_{err}:

$$S_y = \begin{bmatrix} Z_{err,1} & 0 & 0 & 0 & 0 \\ 0 & Z_{err,2} & 0 & 0 & 0 \\ 0 & 0 & \ddots & 0 & 0 \\ 0 & 0 & 0 & Z_{err,m} & 0 \\ 0 & 0 & 0 & 0 & \tau_{err} \end{bmatrix} \tag{4.29}$$

Again, is assumed that there is no covariance between levels. The uncertainties in reflectivity optical depth will be discussed in the next chapter.

After specifying this information, the retrieval begins and is set to iterate until convergence is achieved, if convergence is possible. Each iteration requires a calculation of the kernel matrix. The K matrix, defined by Equation 4.4 as the Jacobean of the forward model with respect to the parameters to be retrieved, is expanded as the following m+1 by m+1 matrix:

$$K = \begin{bmatrix} \frac{\partial Z_1}{\partial \log D_{n,1}} & \frac{\partial Z_1}{\partial \log D_{n,2}} & \cdots & \frac{\partial Z_1}{\partial \log D_{n,m}} & \frac{\partial Z_1}{\partial \log \overline{N}_t} \\ \frac{\partial Z_2}{\partial \log D_{n,1}} & \frac{\partial Z_2}{\partial \log D_{n,2}} & \cdots & \frac{\partial Z_2}{\partial \log D_{n,m}} & \frac{\partial Z_2}{\partial \log \overline{N}_t} \\ \vdots & \vdots & \ddots & \vdots & \vdots \\ \frac{\partial Z_m}{\partial \log D_{n,1}} & \frac{\partial Z_m}{\partial \log D_{n,2}} & \cdots & \frac{\partial Z_m}{\partial \log D_{n,m}} & \frac{\partial Z_m}{\partial \log \overline{N}_t} \\ \frac{\partial \tau}{\partial \log D_{n,1}} & \frac{\partial \tau}{\partial \log D_{n,2}} & \cdots & \frac{\partial \tau}{\partial \log D_{n,m}} & \frac{\partial \tau}{\partial \log \overline{N}_t} \end{bmatrix} \tag{4.30}$$

Next, the forward model is calculated according by application of Equation 4.19 and Equation 4.24. This value of F is substituted into Equation 4.6, producing a new estimate of $\hat{x}$, and the solution is checked for convergence. If convergence has not been achieved, the K matrix is calculated once again and the procedure is repeated. A schematic view of this process is shown in Figure 4-2. Generally, convergence is obtained in less than 10 iterations.

4.4 Algorithm Validation

This concept of posing a radar retrieval in terms of an optical estimation problem, and of using radar reflectivity and visible optical depth to retrieve ice water content of ice clouds, is relatively new. Therefore, the opportunity to test this algorithm against in situ data collected during a field campaign is not possible. However, advanced cloud microphysical models present an excellent opportunity to test the performance of the algorithm using realistic data. Sassen et al. (2001) conducted a study of various methods of retrieving ice water content, using as "truth" a cirrus cloud model with explicit microphysics.

A model with explicit microphysics treats processes such as nucleation, growth, aggregation, and radiative effects without the use of bulk parameterizations. The model is described in detail by Khvorostyanov and Sassen (1998). Although previous simulations using this model have produced results very consistent with observed cirrus cloud growth, the validity of the model is not of particular importance here. It is of greater significance to compare the results of the tau-Z algorithm with other algorithms, and to compare these results with the actual drop size distribution and ice water content of the model.

Sassen et al. simulated the growth of an ice cloud using a generic mid-latitude spring or summer sounding with a 1.5 km thick ice-saturated layer overlaying a thick subsaturated layer. A constant vertical velocity of 3 cm s^{-1} was imposed on the domain for the first six hours to initiate cloud growth, and vertical motion was set to zero for the final six hours of the simulation. Additionally, the sounding profiles were adjusted so that at approximately the same cloud top height and pressure, the cloud top temperature

occurred at –50°, –60°, and –70° C. This final adjustment serves to address the variation of microphysical properties of cloud growth and decay that are observed to vary with temperature in real clouds. The model output was then used to simulated vertical profiles of radar reflectivity. The visible extinction coefficient was calculated from the second moment of the size spectra, according to Equation 4.20, using solid ice spheres of equivalent mass and applying a correction of an increase of 20% to account for the effects of ice density and non-spherical crystals (Fu 1996 and Yang et al. 2000).

The performance of various radar algorithms is discussed in more detail in Sassen et al., but here the focus is on the benefit of the algorithm described above over common Z-IWC relationships. Note that slight differences exists between the tau-Z algorithm output presented in Sassen et al. (2001) and the output presented here; this is due to minor changes the algorithm has undergone since the paper was published, and use of different a priori information.

Figure 4-3 shows a comparison of retrieved IWC with modeled IWC for a cloud-top temperature of –60° C. Since the model IWC is derived directly from the model cloud ice crystal distribution, model IWC will be considered "truth." It is clear that the retrieval algorithm performs well in reproducing the actual ice water distribution. The most notable differences are the retrieved IWC is shifted downward relative to the model, and the horizontal features are somewhat washed out. The former is likely due to retrieval assumptions, notably that the drop size distribution width and number concentration are constant with height. The latter is due to the discrete nature of the radar reflectivity and optical depth simulated measurements.

Though the vertical distribution of IWC is somewhat displaced, the vertical integral of this quantity, ice water path (IWP) matches the simulation well (Figure 4-4):

$$IWP = \int_{Cb}^{Ct} IWC \, dz \tag{4.31}$$

Here, the integral is over the vertical extent of the cloud from cloud bottom (C_b) to cloud top (C_t). The retrieval estimate of IWP is within a few percent of model-truth for all retrievals. In contrast, eight common Z-IWC relationships have also been plotted in Figure 4-4. Clearly, no single power-law relation does particularly well during all times in the simulation. Though some perform well during initial stages of cloud growth, they exhibit large errors cloud decay. This is not surprising, since Z-IWC relations are derived for particular cloud regimes, and are not expected to work well in cloud with rapidly changing microphysics. The tau-Z retrieval, however, performs well during all stages of cloud growth and decay.

Figure 4-5 shows a scatter plot of retrieved ice water content versus modeled ice water content. Again, a fair spread in retrieved IWC is evident, although a linear regression yields a correlation coefficient of 0.91840. As is also evident from both the previous figures, the scatter plot suggests an underprediction of IWC for larger values of IWC, particularly larger than about 0.006 g m^{-3}. Similar comparisons for –50° C are presented in Figure 4-6 and Figure 4-7. The results are very similar, with the retrieval displaying some errors in vertical ice water distribution, but excellent agreement in ice water path. IWC is again underpredicted for larger values, but the retrieved IWP shows considerably better agreement. Again, the tau-Z retrieval performs much more reliably than any of the various IWC-Z relations.

The algorithm performance is summarized in

Table 4-1 and Figure 4-8. The mean absolute error in the IWC retrieved by the tau-Z algorithm is least at –60° C, but never exceeds 1.023 mg cm^{-3}. The correlation coefficient, which is the percentage variance explained, exceeds 0.8 for all cases. Ice water path, as shown in Figure 4-8, is consistently retrieved with great accuracy. Correlation coefficients here exceed 0.99.

Table 4-1: Values of correlation coefficient (r^2), mean absolute error (Mean Err), and standard deviation (σ) of IWC predicted by the tau-Z algorithm for three different cloud-top temperatures.

T (°C)	r^2	Mean Err (mg cm^{-3})	σ (mg cm^{-3})
-50	0.92585	0.727	1.181
-60	0.91844	0.560	0.872
-70	0.82303	1.023	1.318

Finally, to test the robustness of the algorithm to errors in the measurements, a simple sensitivity study was performed using the –60° C case. Random noise was added to the model output reflectivity and optical depth fields to simulate uncertainties in the actual measurements from the MMCR and optical depth estimation techniques. The retrieval was run for 40 iterations, each with an added random noise of up to ±1 dBZ on the reflectivity field and up to ±35% on the optical depth field. These are the same uncertainties that were used for the case study retrievals. Statistics on the retrieved ice water path were collected for each of these runs.

The average and standard deviation of the retrieved ice water path taken over all forty iterations is shown in Figure 4-9. The average retrieved values demonstrate the

same general pattern of Figure 4-4, with underestimation of column-integrated ice content when this parameter is near a peak value. The standard deviations are shown as error bars centered on the averaged retrieved values. These uncertainties are largest in the peaks but small elsewhere. The largest standard deviation in IWP is 3.5 g m^{-2}. This demonstrates that the retrieval reasonably simulates the verification even when realistic uncertainties are introduced into the measurements.

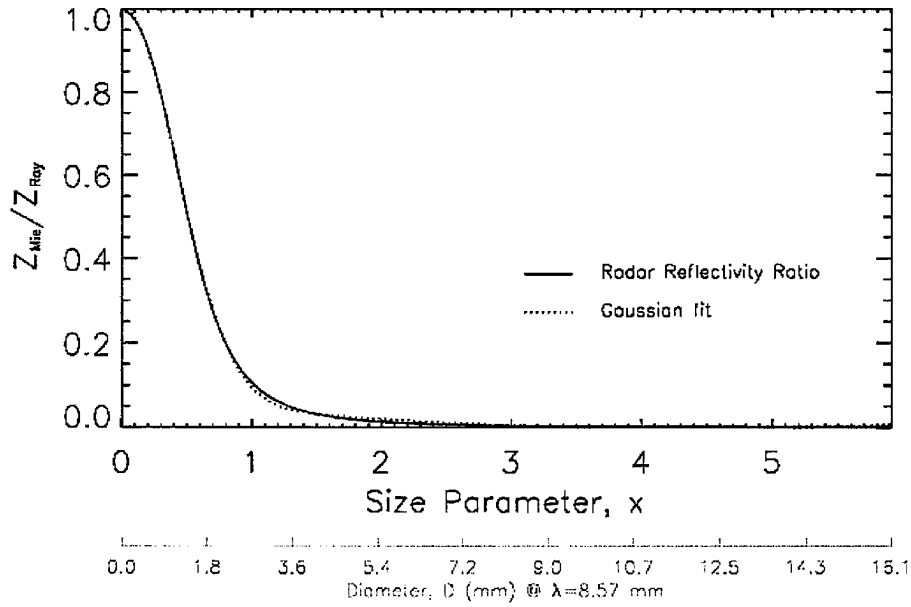

Figure 4-1: Ratio of Mie to Rayleigh reflectivities (Z_{Mie}/Z_{Ray}) as a function of size parameter (and characteristic diameter).

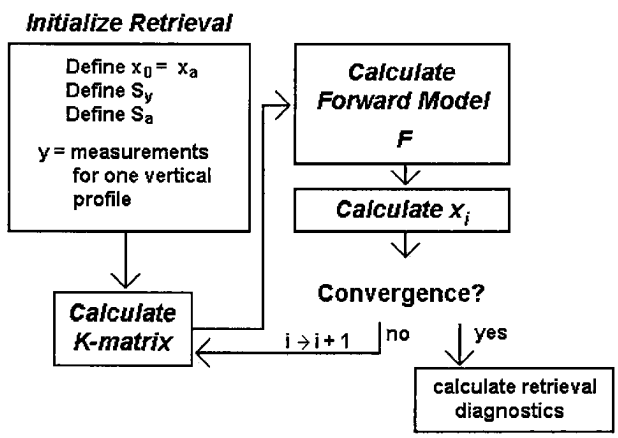

Figure 4-2: Schematic diagram of the retrieval process.

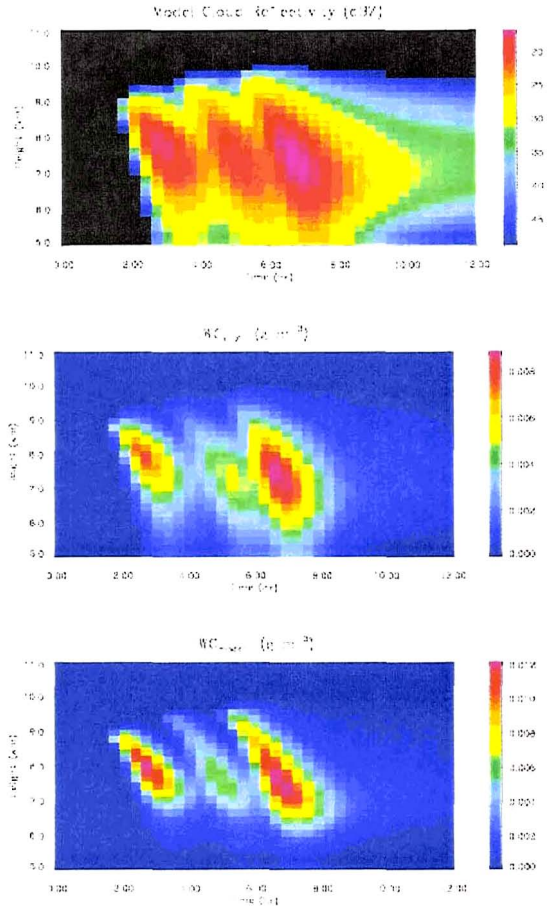

Figure 4-3: Comparison of tau-Z retrieval results with the cirrus model (truth) for a cloud top temperature of –60 °C. Shown are simulated cloud radar reflectivity (top panel), retrieved IWC (middle panel), and simulated IWC (bottom panel).

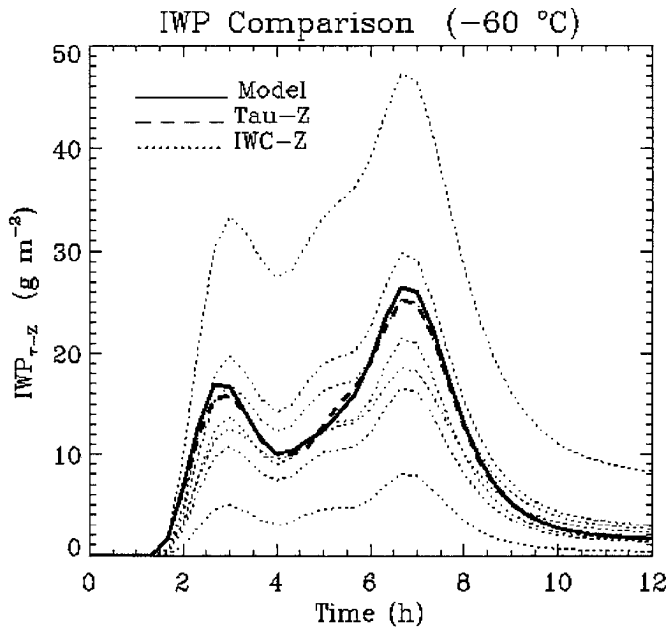

Figure 4-4: Comparison of retrieved ice water path (IWP) with the cirrus model (truth) and various IWC-Z relations for a cloud top temperature of -60 °C. A spread of eight common IWC-Z relations, the same as used in Sassen et al. (2001), are also shown.

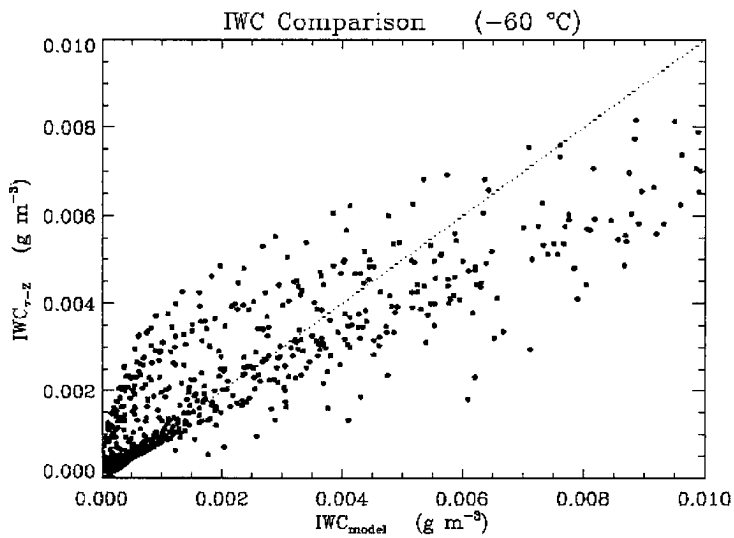

Figure 4-5: Scatter plot of retrieved IWC versus model IWC (truth) for a cloud top temperature of -60 °C.

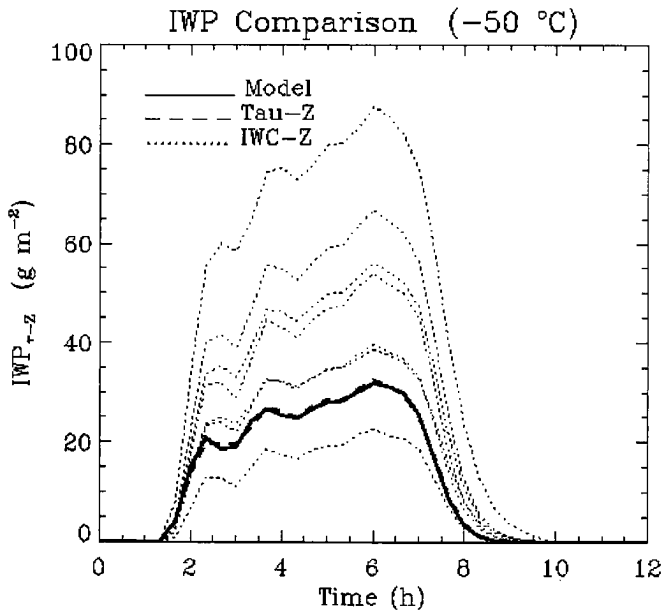

Figure 4-6: As in Figure 4-4, but for a cloud top temperature of –50° C.

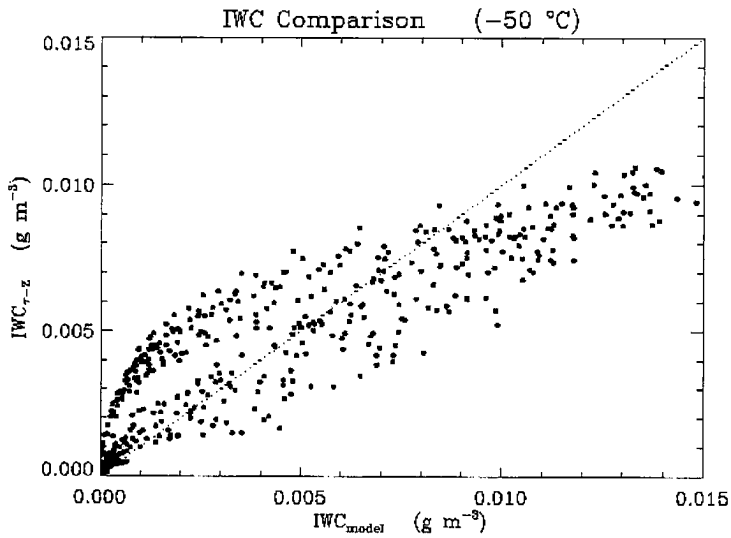

Figure 4-7: As in Figure 4-5, but for a cloud top temperature of –50° C.

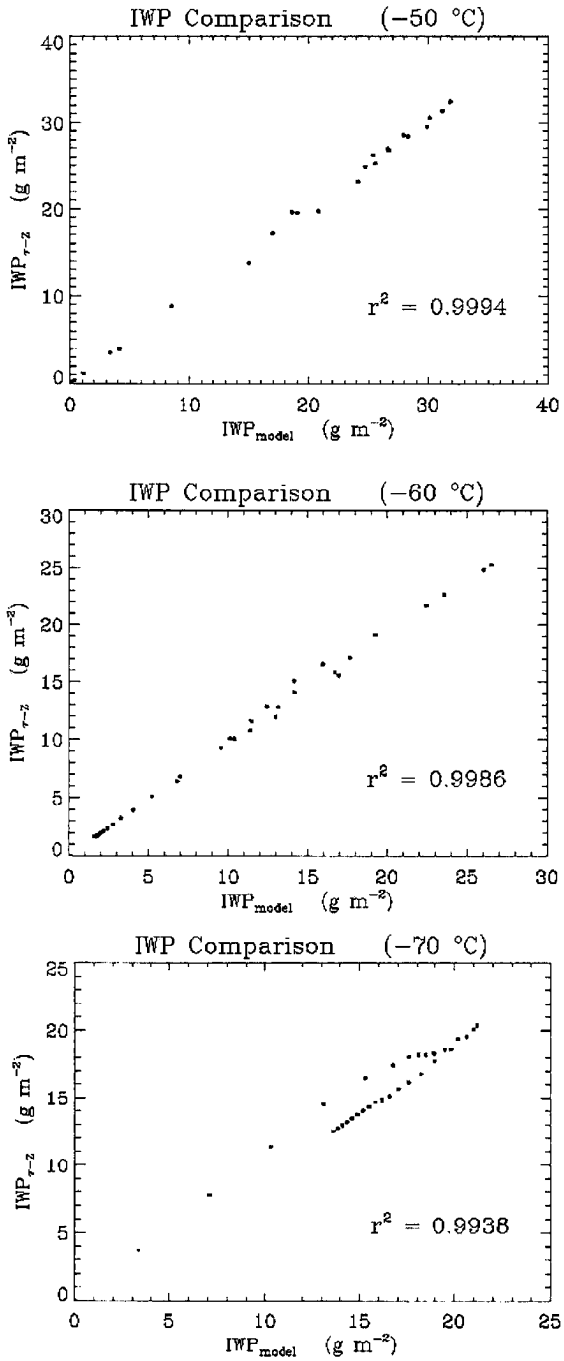

Figure 4-8: Scatter plots of tau-Z retrieved IWP versus model (truth) IWP for –50, –60, and –70° C cases. Correlation coefficients of the fit are 0.9994, 0.9986, and 0.9938, respectively.

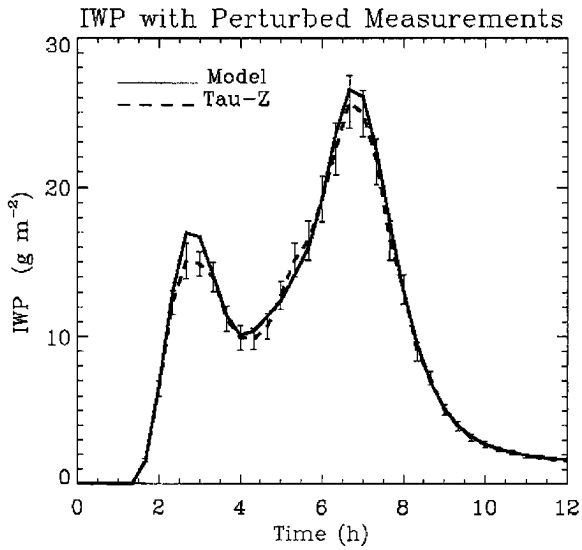

Figure 4-9: Comparison of averaged retrieved ice water path (IWP) for 40 runs with random noise added to the measurements, with the cirrus model (truth) for a cloud top temperature of -60 °C. Up to ±1 dBZ was added to the reflectivity measurements, and up to ±35% was added to the optical depth estimate. Error bars show the standard deviation of mean IWP for each time step over the 40 runs.

Chapter 5

5. APPLICATION OF ALGORITHM TO JET STREAM CIRRUS CASES

5.1 Introduction

The previous chapter introduced a cloud radar algorithm that can be used to estimate key microphysical parameters of ice clouds, and the uncertainties in these estimates. Given vertical profiles of radar reflectivity (Z) and an estimate of cloud column optical depth (τ), the tau-Z algorithm can be used to retrieve vertical profiles of characteristic diameter (D_n) and ice water content (IWC), as well as the mean vertical ice crystal number concentration (N_t). Performance of the algorithm was demonstrated using a simulated cirrus cloud, and it was shown that the algorithm was, for this simulated case, capable of reproducing a time-series of ice water path to within a few percent for a range of cloud-top temperatures. This seems to be the case even when significant noise was added to the measurements of reflectivity and optical depth. It has also been shown that this algorithm is far superior to simple power law relations which relate IWC to radar reflectivity.

The tau-Z retrieval algorithm is the principle investigative tool in this case study of jet stream cirrus. Unlike the composite study that focused on the mean characteristics of

several events, this part of the research will focus on the properties of jet stream cirrus clouds during individually selected cases that occurred over the Southern Great Plains (SGP) ARM Site. The MMCR has been more-or-less continuously operational since 1997, so all these cases were selected from the years since. The recent nature of these data is somewhat of a limitation because of the limited availability of dynamical reanalysis datasets, as will be discussed shortly.

5.2 Data Sources and Case Selection

Cases were selected on a more subjective basis than was the case in the composite study. This was a necessary consequence of the shorter time period of study and nature of the input data. Gaps in these data sets forced the rejection of several of the favorable cases (for example, those with a "cleaner" radar signature) in favor of those with more temporally consistent and reliable measurements of radar reflectivity and estimates of cloud optical depth.

Table 5-1 lists the events selected for the study. Cases were limited to 1997 through 1999, bounded by the operational start of the MMCR and the end of data availability. The case selection process involved a survey of infrared satellite data during the winter of these two years to locate cloud patterns consistent with strong jet streams, and thus the potential occurrences of jet-forced cirrus. Independence of cases was not deemed so important as it was during the composite study, and in fact one day (13 November 1998) is separated into two separate cases that describe both the growth and decay of the cirrus cloud layer.

Table 5-1: Dates of case studies. Shows availability of MMCR reflectivity data, source of column optical depth estimates, and availability of ETA/EDAS model data. X = full data availability, P = partial data availability.

Case Date	MMCR Reflectivity	Column Optical Depth Estimate		ETA/EDAS Model Data
		MFRSR Derived	Lidar Derived	
25 Feb 1998	X	X		X
13 Nov 1998 (I)	X		X	X
13 Nov 1998 (II)	X	X		X
20 Nov 1998	X	X		P
22 Dec 1998	X		X	X
7 Feb 1999	X	X		X

The case selection was, again, somewhat subjective and based largely on the quality of the reflectivity and optical depth data. Cases were selected that minimized the number of missing data points, and still presented a relatively uncluttered radar signal featuring a cirrus cloud layer or layers that was not obstructed by underlying lower clouds or precipitation. Availability of model data, to enhance the dynamical portion of the study, was not a requirement for case selection, although these data were available in most cases.

The cloud reflectivity, optical depth, and dynamical data sets used in the case studies, and the quality of the datasets, will now be presented.

5.2.1 Cloud Reflectivity

Radar reflectivity from the MMCR, described and mathematically defined in Section 4, is one of two inputs for this retrieval. Reflectivity data was cleaned to eliminate clutter and non-cirrus returns from the data set. Since cirrus clouds occur only at high altitudes within the troposphere; any radar returns that occurred below a height of 4.5 km or that were obviously above the tropopause were eliminated from the dataset. Returns flagged as clutter, as described in Section 3.3 and by Clothiaux et al. (2001), were also removed. Clutter removal is especially important in the study of thin cirrus since typical cloud returns can be in the –20 to –40 dBZ range, comparable with non-meteorological targets that are detected by the radar. The resulting data set is considered a fairly pure representation of actual meteorological returns, although not necessarily only from cirrus clouds.

To determine returns that are associated with clouds, each radar time interval was scanned from bottom to top for vertical gates that contains two consecutive occurrences of reflectivity above some reflectivity threshold (generally taken to be –40 dBZ). Such locations were assigned as the cloud base boundary. Similarly, a cloud return with two consecutive returns above it that do not meet the reflectivity threshold was assigned as cloud top boundary. This simple and intuitive method of determining cloud boundaries can still accommodate multi-layered cloud systems. This is essential for the case of jet stream cirrus since cloud fragments can frequently be found below the main cloud deck.

Since cirrus clouds typically do not precipitate, with the exception of fallstreaks that are sometimes observed as ice crystals detrain from the cloud, this resulting data set should, ideally, consist entirely of cloud particle returns. The final processing performed

on the reflectivity data is temporal averaging; the data must be "averaged-down" to the time resolution of the optical depth estimates described below.

5.2.2 Estimation of Cirrus Optical Depth

Estimates of cirrus cloud optical depth are derived from two instruments, the Multi-Filter Rotating Shadowband Radiometer (MFRSR) and the Raman lidar. Both of these are located at the ARM SGP central facility, nearby to the MMCR cloud radar.

The MFRSR estimates of cirrus cloud optical depth are provided by Dr. Qilong Min of the State University of New York at Albany. The MFRSR makes spectral measurements of direct normal, diffuse horizontal, and total normal solar irradiances at wavelengths ranging from 415 to 940 nm.

The optical depth is derived by first estimating atmospheric transmittance. Langley regression of the diffuse-normal irradiance on a clear day is used to extrapolate the response function of the instrument. The transmittance is then calculated on cloudy days as the ratio of the uncalibrated output to the extrapolated value for the top of the atmosphere (Qilong Min, personal communication). This allows derivation of the total spectral optical depth, τ_{total}, from Beer's Law:

$$T_\lambda = \exp(-\tau_{total} / \mu) \tag{5.1}$$

where T_λ is spectral transmittance and μ is the solar zenith angle. The total optical depth is given by:

$$\tau_{total} = \tau_{ray} + \tau_{o3} + \tau_{h2o} + \tau_{aer} + \tau_{cloud} \tag{5.2}$$

and is assumed to include contributions from Rayleigh scattering, ozone, water vapor, aerosol, and cloud, respectively. The optical depth τ_{cloud} is simply calculated as a residual

of the other components which are known or estimated. The Rayleigh contribution can be isolated by knowledge of surface pressure. Well-chosen passbands allow the ozone and water vapor contributions to be isolated as well. This leaves aerosol and cloud contributions to be separated.

Because these two contributions are wavelength dependent, they can be separately determined using measurements at 415 and 862 nm. However, since the MFRSR has a finite field of view, irradiance from forward scattering of clouds and aerosols is received in addition to the attenuated direct radiance. Two measurements of shadowband side-blocking attempt to remove some of this forward scattering, and this is especially effective in the case of aerosol where forward scattering is not particularly significant. For cirrus clouds, however, it should be noted that the optical depth may sometimes be underestimated because of this effect.

A potential source of error with the MFRSR is the mismatch between what the radar observes and what the radiometer observes. The radar is always pointed at nadar, but the MFRSR observes radiation that originates along a slant path. This is less of a problem when the overhead scene is more homogeneous, and is not deemed to be a serious problem in the case of the fairly uniform cirrus layers that are observed in this study. However, this is a factor that is accounted for in the measurement uncertainty vector, using uncertainties provided with the data.

A smaller selection of cases use optical depth data obtained from the Raman lidar, a device that measures laser backscatter from cloud and aerosol particles. A simple attenuation technique is used, whereby backscattered power at the top of the cloud is compared to backscattered power at the bottom of the cloud (David Turner, personal

communication). The difference is due to the two-way attenuation by molecules and the cloud itself. Molecular extinction is calculated by a radiative transfer model using a measurement or estimation of the vertical temperature profile. In this case, the vertical temperature profiles are obtained from the University of Wisconsin AERI+GOES product, introducing a source of error into the calculations. These errors, however, are quantifiable and specified by the data providers.

These optical depth estimates have a time resolution of approximately five minutes, where available. The period of the optical depth data is considerably less than that of the radar data, so the radar data must be temporally averaged to the approximate resolution of the optical depth data. The averaging is only performed over two or three vertical profiles surrounding each optical depth time step, such that the cirrus reflectivity data is more representative of the moment in time when the optical depth measurements were made.

Finally, the retrieval requires error estimates of all elements that contribute to the measurement vector. The uncertainty in optical depth is taken to be 35%, and for consistence this value is used for both MFRSR and lidar-derived data. The uncertainty in radar reflectivity is taken to be 1dBZ.

5.2.3 Dynamical Data: NCEP Analyses and ETA/EDAS Forecasts

Large-scale dynamical data were used to view radar-based cloud observations in a synoptic scale context. NCEP analyses of upper-air data, based on the national rawinsonde network, are used when available. Similarly, NCEP surface analyses have been obtained for use in this study.

Regional dynamical data are produced by the so-called Early ETA model, an operational forecasting model run by the National Centers for Environmental Prediction (NCEP). The Eta Data Assimilation System (EDAS) is an integral part of the Early ETA model. EDAS is a sequential three-dimensional regional variational data assimilation system. It generates eight "initial states" during every 24-hour period. EDAS assimilates a set of high frequency observations, including data from geostationary satellite-based atmospheric retrievals, wind profilers, NEXRAD radar, aircraft, and various other marine and land-based observations (Rogers et al., 1996).

EDAS data were obtained for a location that is within 5.5 km of the ARM SGP site. Time and height series of fields like temperature, pressure, specific humidity, vertical velocity, cloud fraction, and cloud water content were available for most of the period of interest. Radiative fields like longwave and shortwave heating rate were also obtained.

There are a few drawbacks to use of the ETA/EDAS data set, but perhaps the greatest motivation for its use is a lack of alternatives. Two significant problems that are immediately apparent are related to time resolution and continuity. The ETA/EDAS model produces hourly vertical profiles of the dynamical variables that have been described. However, the timescale of the cirrus clouds of interest is often considerably shorter; significant changes in cloud radar reflectivity, indicative of significant microphysical changes, are observed to occur with a period of only a few minutes.

Another potential drawback to this data set is related to the data assimilation process, and the associated reliance on model forecasts as pseudo-data. Assimilation schemes seek to minimize the difference between model forecasts and observations, so the observations are blended with model output in such a way that the continuity of the

model is maximized. Put another way, the initial states are based on observations, but are not themselves observations; they are also a function of the previous model forecasts. For example, the EDAS system seeks to minimize a cost function of the form:

$$J = J_b + J_o + J_{bal} \tag{5.3}$$

Where J_b represents the model forecast or background estimate, J_o represents real observations, and J_{bal} represents a weak constraint between mass and velocity variables (Zapotocny et al., 2000).

Models have proven very useful for filling in gaps in our observations and providing data where no observations are available. For this study, it will be shown that the EDAS initializations and forecasts generally do a fair job of predicting the location of jet stream cirrus layers, and these model estimates will be utilized while keeping the aforementioned limitation in mind.

5.2.4 Environmental Temperature

Environmental temperature data are obtained from radiosonde observations, launched from the ARM SGP central facility several times daily. A vertical temperature profile is obtained once for each case, from a launch that is close in time to the time cirrus were present. The temperature data are used to examine the relationship, if any, between ice water content and temperature within these cirrus.

5.3 Microphysical Processes in Cirrus Clouds

Before examining the case studies, it is worthwhile to briefly review known microphysical processes that are at work within mid-latitude cirrus clouds that are not

directly associated with convection. Cirrus are the highest clouds in the troposphere, and frequently occur at temperatures less than –40° C. It is believed that vertical motions in the upper troposphere lead to the lifting of cloud condensation nuclei to the point of deliquescence when they form small drops of solution. As condensation occurs on the nuclei, decreasing the solution concentration, and temperature continues to decrease, homogeneous freezing of water becomes more and more likely (Young, 1993). This process frequently occurs in so-called generating cells where the environment is supersaturated with respect to ice (Heymsfield, 1975).

Ice particles continue to grow under conditions of ice supersaturation and fall toward the bottom of the cloud or are carried away by the wind. Within the cloud or just below cloud level, conditions become subsaturated with respect to ice and ice crystals begin to sublimate, sometimes creating fall streaks. Sublimation can be a slow process and ice crystals may fall through several kilometers of the atmosphere before ceasing to exists as ice (Stephens, 1983).

Maintenance and growth of particles after nucleation seems to be directly tied to the radiative properties of the crystals. In particular, the larger ice particles are colder than the smaller particles under conditions of net radiative loss (Young, 1993) since they have a greater radiating surface area. Cooling of ice crystals increases the gradient of vapor density between the particles and the environment, causing deposition to occur on the particles and thereby decreasing the environmental vapor density. The larger, colder particles would therefore continue to undergo deposition even when the environmental vapor density decreased to a value that would no longer support deposition on the smaller particles. This process is believed to lead to the preferential growth of larger ice crystals

at the expense of smaller ice crystals. By similar reasoning, under conditions of net radiative warming, the larger crystals sublime, thus narrowing the crystal spectra (Wu et al., 1999).

5.4 Case Study Analysis

The cases selected according to the guidelines described above will now be presented. Each case analysis will include the following:

- Radar observations of cirrus during the event,
- The large-scale dynamical context,
- Regional-scale dynamics that may govern cloud development and dissipation,
- Retrieved vertical profiles of ice crystal effective radius and ice water content (with associated uncertainties),
- Column-averaged ice crystal number concentration, effective radius, and ice water path.

Following the presentation of individual cases, Section 5.5 summarizes the findings from these cases and present some bulk statistics and conclusions that may be drawn about properties of the observed cirrus clouds, and their relation to the large-scale dynamics, based on these findings.

5.4.1 Case Study: 1998 December 22

On 1998 December 22, a broad upper jet was oriented from the southwest to the northeast across the central United States, with 300 hPa winds exceeding 72 m s^{-1} (140 kts) over Missouri and central Illinois (Figure 5-1). Interpolation of this wind speed to

the SGP site at 00 UTC leads to an estimate of approximately 67 m s^{-1} (130 kts), placing the ARM site just to the south and on the anti-cyclonic side of the jet core. The surface analysis shows the surface front associated with the jet stretched from western New York through western Kentucky and eastern Texas. A 1039 hPa high pressure ridge was propagating southeastward into Kansas and Oklahoma behind the front. Note the clear skies were reported over most of western Kansas and Oklahoma, while to the east many surface stations still reported cloud cover in the north to northwesterly flow behind the front.

Radar observations of the conditions at the SGP site are shown in Figure 5-2. A high but relatively thin cloud, at times up to 2 km thick, was present from 00 UTC until approximately 12 UTC. The average height of the cloud was approximately 9 km, or 200 hPa. Typical radar reflectivities were in the range of –15 to –25 dBZ toward the center of the cloud, with reflectivities of –30 dBZ at the cloud edge. The cirrus layer underwent rather rapid vertical development at approximately 02 UTC, and then the cloud base height gradually increased from approximately 8.6 km to 10.5 km throughout the lifecycle of the cloud. There were times, such as at 06 UTC, when the cloud became very tenuous, only to thicken during the next hour. As a side note, most of the radar returns that were presents near the surface in the first two hours of the day were flagged by the algorithm as clutter, and thus removed.

Doppler-derived vertical velocities were all downward over the life cycle of the layer, ranging from about 0.5 to 1.0 m s^{-1}. This observation will now be examined in the context of the large scale vertical motion in the sections to follow.

Figure 5-2 also shows the estimated column optical depth derived from the Raman lidar. Three distinct regimes were present. Between 00 and 01 UTC, the optical depth oscillated between 0.1 and 1.5; this corresponded to the cirrus layer at its lowest altitude during the day. Then, between 01 and 02 UTC, the amplitude of these oscillations decreased and the optical depth settled to an average value of about 0.3, simultaneous with the observed reflectivity minimum. At 02 UTC, the optical depth increased suddenly, and remains at an average of about 1.5 through 03 UTC. This corresponded with the time of rapid vertical development noted above.

Results of the retrieval are shown in Figure 5-3 and Figure 5-4. The influence of the optical depth regimes noted above is clearly evident. During the first hour of the day, the characteristic ice crystal diameter maximized at approximately 100 μm, then relaxed to 30-50 μm over the second hour, and peaked again at about 80 μm in the third hour. This corresponded to ice water content maxima of about 0.08, 0.02, and 0.07 g m^{-3} over the first, second, and third hours, respectively.

The uncertainties in these quantities are characteristic of the retrieval. The ratio of ice water content uncertainty to ice water content varies from 0.20 to 0.42. Uncertainties of this magnitude are expected given the problems noted in the simulations of the previous chapter. The uncertainties in the characteristic diameter are somewhat less, with the ratio of characteristic diameter uncertainty to retrieved diameter ranging from 0.07 to 0.14.

These large uncertainties in IWC more than likely originate in the assumption that ice crystal number concentration (N_t) is constant with height. The retrieved column mean number concentration is shown in Figure 5-4. It varied from 10^3 to 10^5 particles per

cubic meter, and had an average value of 1.7×10^4. Although the errors in the column mean number concentration are fairly small, indicated by the error bars that are centered on the retrieved value, this is of little consequence if the built-in assumption that N_t is constant with height is itself poor. One microphysical process that may alter the vertical profile of number concentration is the preferential growth of larger ice crystals over smaller ones through the process described in Chapter 5.3.

The retrieved column ice water path, for reasons described earlier, is likely to be a more reliable estimate than any individual retrieved value of ice water content. During the first hour, the IWP varied between about 20 and 80 g m^{-2}, dropped to less than 10 g m^{-2} over the next hour, and increased to a maximum of 92.3 g m^{-2} during the third hour as the period of rapid development occurred.

The IWC is plotted against radar reflectivity in Figure 5-5. The points are color-sorted according to radiosonde-derived environmental temperature. No clear relationship between temperature and the scatter of the points is evident. It is interesting to note, however, that most of the returns from particles in the warmer –37.7 to –44.1 °C range are associated with the higher reflectivities in the –10 to 5 dBZ range.

The thin solid lines in Figure 5-5 are the overlay of several common IWC-Z power law relationships. Note that the retrieved ice water contents lie within the range of several of these power-law relations. Using these data, it is possible to derive an IWC-Z relation specific to this cirrus cloud, using the assumed form

$$IWC = a\, Z^b \tag{5.4}$$

where Z is the reflectivity in $mm^6\ m^{-3}$ and the IWC is expressed in g m^{-3}. Applying a linear regression to the data, the following coefficients were found:

$$a = 0.028728$$

$$b = 0.505501$$

The power-law relationship using these coefficients is plotted as a thick solid line. The correlation coefficient of this fit is $r^2 = 0.944$. The significance of this new relation, if there is any, will be further examined after all the case studies have been presented.

Now the quality of the retrieval will be examined. The averaging kernel, A, is given by Equation 4.5. Recall that when the A matrix equals the identity matrix, I, the final term in Equation 4.6 goes to zero, thus indicating that the a priori information x_a does not contribute to the estimate of x. For every retrieval performed by this algorithm, the A matrix is, in fact, nearly unity. This simply indicates that the retrieval is quite insensitive to the a priori assumptions. It also means that the A matrix is not a particularly useful diagnostic of the retrieval performance. Note that this does not mean that the a priori information plays no role in the retrieval; in fact, the a priori information serves as the initial estimate and increases the stability of the retrieval.

The most useful diagnostic, perhaps, is the chi-squared statistic:

$$\chi^2 = (y - F)^T S_y^{-1} (y - F) + (x_a - \hat{x})^T S_a^{-1} (x_a - \hat{x}) \tag{5.5}$$

where chi-squared follow the chi-squared distribution with degrees of freedom equal to one less than the number of cloud pixels in the retrieval. According to Equation 5.5, a tight constraint imposed by specifying small uncertainties in the measurements (S_y) or a priori (S_a) leads to a small values of χ^2. Conversely specifying a loose constraint increases the value of χ^2.

Application of a chi-squared significance test at the 0.1% level is used to define minimum and maximum values of χ^2 that define a "quality" retrieval. If the chi-squared

statistic for any retrieval lies outside these bounds, the retrieval is discarded. Results of the chi-squared test for this case are shown in Figure 5-6. Note that all the retrievals fell within the required bounds, and none were discarded.

The dynamical context surrounding the growth of the cirrus that have been examined can be explored through the EDAS model (Figure 5-7). The 300 hPa EDAS wind speed agrees quite well with the analysis data, showing a wind speed of 57.4 m s^{-1} (111.4 kts) at 00 UTC. The jet stream became more and more shallow as the day progressed. The cloud fraction field shows upper-level cloud cover centered at about 200 hPa throughout the entire day, although the highest cloud fractions occur between 00 and 14 UTC, coincident with the radar-detected cirrus deck. Large scale subsidence, on the order of 0.5 Pa s^{-1}, was evident through most of the troposphere during the first half of the day. This is consistent with the intrusion of high pressure noted on the surface analysis. This broad sinking layer was capped by a region of weak or neutral upward motion that was present in the cloudy region. Thus, the region of observed cirrus was accompanied by a weak but large scale lift on the order of 0.0 to 0.2 Pa s^{-1}. Also note that EDAS detected a lower cloud layer earlier in the day, in the relatively moist later between 700 and 850 hPa, although the presence of this cloud is not supported by the radar observations.

Vertical profiles of several other EDAS parameters for 03 UTC are shown in Figure 5-8. Note that the model diagnosed ascending large-scale motion on the order of –0.2 Pa s^{-1} at or just below the cloud level. This was accompanied by a high specific humidity anomaly of approximately 0.1 g kg^{-1} between 250 and 450 hPa. The diagnosed upward motion for 01 through 04 UTC (Figure 5-9) also shows the general pattern of

strong sinking motion in the lower troposphere, and weak sinking or rising motion in the upper troposphere. At cloud level, neutral or rising motion was diagnosed at 03 UTC, and it is unknown if this is related to the rapid cloud thickening that occurred at about this time.

Bulk environmental statistics for the cirrus layer are presented in Table 5-2. These are EDAS-derived statistics for the cirrus layer between 00 and 12 UTC, where the cloud fraction met or exceeded 5%. The mean vertical motion was nearly zero, with a standard deviation of 0.117. The mean temperature was 211.6 K, which is on the lower end of the radiosonde measurements. The average wind speed over the period was approximately 70 m s^{-1} (136 kts).

Table 5-2: EDAS-derived environmental statistics for cirrus layer between 0 and 12 UTC on 22 Dec 1998, for pixels where cloud fraction met or exceeded 5 %.

	Mean	Standard Deviation
Omega (Pa s^{-1})	0.032	0.117
Specific Humidity (g kg^{-1})	0.047	0.059
Temperature (K)	211.6	31.2
Wind Speed (m s^{-1})	70.3	12.7

5.4.2 Case Study: 1998 November 20

On 1998 November 20, a cirrus cloud deck developed over Oklahoma late in the day. The southwest end of an upper level jet streak was exiting the SGP site at about this time (Figure 5-10), placing the SGP site on the cyclonic side of the jet. The jet extended from southern New Mexico to Nova Scotia. The associated surface front stretched from

off the New England coast to New Orleans by 00 UTC on November 21. Maximum 300 hPa winds were on the order of 67 m s^{-1} (130 kts), while the 00 UTC winds over the Oklahoma-based MMCR were southwesterly at an estimated 52 m s^{-1} (100 kts). At the surface, a closed 1029 hPa high pressure region was centered over central Oklahoma. Between 12 UTC 20 November and 00 UTC 21 November, the number of sites in Oklahoma that reported cloud cover increased, presumably due to the cirrus band moving over the state.

Radar observations from 20 November are shown in Figure 5-11. While there was presumably some convection earlier in the day, the sky cleared after 05 UTC and remained clear until approximately 16 UTC. At 16:30 UTC, several cloud fragments developed and then dissipated at 10.5 km. Then, a more sustained cloud developed just before 19 UTC. Reflectivities were near the minimum detectable signal of the radar, less that –35 dBZ. The cloud extended from approximately 9.0 to 10.5 km until 22 UTC, and then the base quickly deepened to 7.5 km. The cloud continued to exist on radar until after 05 UTC 21 Nov, although optical depth data are not available for this time period.

Doppler velocities were fairly uniformly in a direction away from the radar, averaging about 0.5 m s^{-1} with some embedded regions approaching 1.0 m s^{-1}. The streaks of higher upward velocity were not necessarily aligned with any reflectivity anomaly, and most of these anomalies occur in the middle of the cloud, away from the cloud top and bottom.

Optical depth data from the MFRSR reveals that the optical depth varied between 0.0 and 1.13 between 14 and 22 UTC, when data were available. The optical depth

increased to 0.33 at 17:30 UTC, probably coincident with the first cloud fragments detected by the MMCR. Then, from 18 UTC until 21:45 UTC, optical depth increased to the maximum of 1.13. This matches the time of cloud deepening observed on radar.

Retrievals of IWC and characteristic diameter are shown in Figure 5-12 and Figure 5-13. Prior to 21 UTC, characteristic diameters of 20-30 μm were common, and then these increased rapidly to 35-50 μm. Retrieval uncertainties in D_n were approximately 25-30% of the retrieved values. Ice water contents did not undergo such a sudden change, and were consistently about 0.002 g m^{-3} until 21:45 UTC, and then in the 0.004 to 0.006 g m^{-3} range after this. The maximum IWC of 0.0085 g m^{-3} occurred at 21.0 UTC. Uncertainties on IWC were on the order of 30 to 40%.

The mean number concentration reached its largest value, and the mean diameter its smallest, in the period before 18 UTC. These values represent the cloud fragments that preceded the main cloud. At 17:55 UTC, the mean number concentration reached 7.9 x 104 m^{-3}, and the average diameter was 0.0129 μm. After the development of the main cirrus deck, the average diameter continued to increase from approximately 20 μm at the start to 40 μm by 22 UTC. The number concentration fell during the same period. These observations are consistent with a growth process that preferentially selects large ice crystals over smaller ones. Ice water path varied between 0.4 to 10.4 g m^{-2} over the life cycle of the cloud, showing no particularly rapid increase at the time of cloud deepening.

A scatter plot of IWC versus radar reflectivity is shown in Figure 5-14. A number of outlying points, all of which corresponded to the cloud fragments before 18 UTC, can be seen in the far upper-left corner of the plot. These points all featured reflectivities less

than –30 dBZ, anomalously high ice water contents, and occurred in the coldest temperature regimes. Regression yielded power law coefficients of:

$$a = 0.0152440$$

$$b = 0.386587$$

with a correlation coefficient of 0.70. Looking at the regression line, it is clear that the regression has been affected by the outliers and the observed fact that, in this case, the IWC-Z relation tends to spread for lower reflectivities.

The chi-squared analysis (Figure 5-15) shows that no retrieved profiles were rejected at the 0.1% level. All retrievals met the requirements placed on the a priori and measurement uncertainty.

EDAS model data were available only through 20 UTC. The EDAS cloud fraction (Figure 5-16) showed an upper level cloud present the entire day, which was not supported by the radar data. The mid-and low level cloud cover that occurred between 00 and 05 UTC, however, was fairly well represented. After 05 UTC, EDAS continued to show relatively thick cloud in a region of rather high humidity centered on 700 hPa. This, again, is not supported by radar observations. The 300 hPa wind speed diagnosed by the model at 20 UTC was 59.6 m s^{-1}, comparable to the estimate from the analysis four hours later. The vertical motion fields showed weak upward motion early in the day replaced by stronger subsidence throughout most of the troposphere as the day progressed. The strongest downward motion occurred in the middle troposphere, as shown by the 20 UTC sounding of Figure 5-17. The cloud itself was associated with only a very slight humidity anomaly, no greater than 0.3 g kg^{-1}. The presence of the

cloud also had very little effect on the radiative heating rate of the atmosphere in the model.

Figure 5-18 shows vertical motion profiles for the last four available time steps in the EDAS output, 17 through 20 UTC. Vertical motion at cloud level indicates there was subsidence at 17 UTC, followed by weak lifting on the order of 0.3 Pa s^{-1} at 18 UTC, which is about one hour prior to initiation of the main cloud. Weak subsidence is diagnosed at 19 and 20 UTC.

The environmental statistics at cloud-level are summarized by Table 5-3. Weak subsidence was the predominant mode of vertical motion. The environmental temperature was on the order of –60 °C, sufficient for the heterogeneous nucleation of ice.

Table 5-3: EDAS-derived environmental statistics for cirrus layer between 16 and 20 UTC on 20 Nov 1998, for pixels where cloud fraction met or exceeded 5 % (total of 22).

	Mean	Standard Deviation
Omega (Pa s^{-1})	0.104	0.158
Specific Humidity (g kg^{-1})	0.075	0.047
Temperature (K)	212.8	46.7
Wind Speed (m s^{-1})	62.2	14.8

5.4.3 Case Study: 1998 February 25

The 1998 February 25 case differs from the other case studies in that a strong surface low pressure center was located in the vicinity of the radar. The surface analysis for 00 UTC Feb 26 (Figure 5-19) shows a 980 hPa low pressure centered over South

Dakota, with a cold front leading a pressure trough and another cold front following. The colder northwesterly flow behind the system was located to the west of this second cold front. The upper level flow was south-southwesterly over the SGP site, with the radar located to the north (cyclonic side) of a 55 m s^{-1} (110 kt) jet maximum at 300 hPa. Estimated wind at this level over the SGP site was 46 m s^{-1} (90 kts). Cloud cover from surface reports in the region was sporadic, with a clearing sky reported behind passage of the first front. It is estimated that frontal passage probably occurred at the radar site at 18 UTC.

Observations from the MMCR radar are given in Figure 5-20. High clouds were reported throughout the day, but MFRSR-based optical depth data was available only after 14 UTC. The cloud layer of interest developed after 16 UTC, and lowered and thickened through 00 UTC. Optical depth estimates indicate that the optical depth averaged around two over the lifecycle of the cloud, but exceeded 4.0 just after 21 UTC. The cloud center height started at approximately 8.5 km, but lowered just over 1.5 km over the course of eight hours. Given the relatively low cloud altitude and high optical depth, it can be argued that this was probably not a pure cirrus cloud, but more of a hybrid or perhaps in transition from cirrus to a cloud with more stratiform characteristics. Since radar reflectivity is related to the sixth power of drop diameter, the high reflectivity values present near the cloud base may indicate that that larger ice particles collected here. Also noteworthy are the reflectivity "streaks" that extended above and below the main cloud, from 22 UTC through the end of the day. The origin of these returns is unknown, but they were marked as clutter by the processing algorithm and therefore not considered.

The Doppler velocity in the cloud averaged near zero, although some stronger regions of upward motion, perhaps representing lofting of cloud particles by a strong updraft, were evident in the data and most prominent in the latter stages of study. A few radar gates near cloud base actually show brief ascending motion exceeding 1 m s^{-1}. Whether or not these returns are trustworthy is unclear, given their close connection with the "streaks" below the cloud base. This question will also be examined in terms of the microphysical retrieval.

The retrieved microphysical parameters are shown in Figure 5-21. Ice water content remained a relatively uniform 0.03 g m^{-3} until 21:30 UTC, and then began an upward trend near cloud base. IWC reached a maximum value of 0.14 g m^{-3} over the next two hours, with these large values all concentrated at the cloud base. Characteristic diameter was on the order of 40 μm until this transition, and then eventually reached a maximum value of 107.6 μm at the cloud base. The mean column statistics (Figure 5-22) show that while mean number concentration was steady during the beginning stages of cloud growth, it decreased after 22 UTC. Similarly, the characteristic diameter ranged from 40 to 50 μm until 22 UTC and then increased to a maximum value of 67.7 μm. As has been seen in previous cases, the developing cloud undergoes a transition from many small ice particles to a fewer number of large ice particles. The mean ice water path was 24.6 and 72.2 g m^{-2} between 16 and 20 UTC, and 20 and 23 UTC, respectively.

These figures suggest that a cloud growth process was initiated between 21 and 22 UTC, and may have been dominated by the aggregation of ice crystals or lofting of supercooled water droplets. This is supported by the decrease of N_t and the decrease of D_n during the final hours of the study. The Doppler-derived upward motion that was

observed at this time also supports this theory, both because it would tend to produce a differential fall velocity between variously sized particles, and also because it could potentially encourage the deposition of supercooled water.

A scatter plot of IWC versus radar reflectivity is shown in Figure 5-23. The presence of some supercooled water certainly can not be ruled out, given that a few retrieved points occurred at temperatures as high as –26 °C. The scatter of points, however, is relatively small. The derived coefficients of the power-law relation $IWC = a\,Z^b$ are:

$$a = 0.0460823$$

$$b = 0.484201$$

with a correlation coefficient of 0.95. The slope of the regression line is less than any of the other common IWC-Z relations shown.

The chi-squared analysis (Figure 5-24) shows that no retrieved profiles were rejected at the 0.1% level. All retrievals met the requirements placed on the a priori and measurement uncertainty.

The EDAS model diagnosed high clouds throughout the entire day, not capturing the two cloud-breaks evident in the radar data (Figure 5-25). A deepening jet was evident after 12 UTC, with winds exceeding 40 m s^{-1} occasionally found at altitudes below 500 hPa. The vertical motion profile contrasts sharply with that of most of the cases examined in this study; ascent, rather than subsidence, was maximized in the middle troposphere throughout most of the day. This is more or less expected, however, given the low-level convergence produced by the low pressure trough to the northwest. A

shallow layer of low-level moisture was also apparent, but this was slowly eroded as the boundary layer dried following the 18 UTC frontal passage.

Two soundings are provided, at both 19 and 23 UTC, to describe the more pure cirrus phase before 21 UTC and the more dynamic state after (Figure 5-26). The 19 UTC profile is more typical of the other cases, with weak uplift and a slight positive specific humidity anomaly at cloud-level. Also note the strong radiative heating of 6 K day^{-1} induced by the cirrus layer, a common effect in high, relatively thin clouds, whereby the cloud emits at a lower temperature than the surroundings. The 23 UTC profiles show nearly neural or slightly upward vertical motion at cloud-level, which the model correctly shows at a lower level than 19 UTC. Significant drying of the mid-levels is also indicative of the frontal passage that took place several hours earlier.

Profiles of the vertical motion parameter, omega, are given in Figure 5-27. A transition from synoptic-scale subsidence to rising motion is evident in the troposphere below cloud level, but weak uplift not exceeding –0.3 Pa s^{-1} occurred in the cloud layer itself.

Information on the EDAS-derived environment surrounding the cloud is summarized by Table 5-4. The relatively high average specific humidity is noteworthy; this, again, is something that sets this case apart from the others.

Table 5-4: EDAS-derived environmental statistics for cirrus layer between 16 and 20 UTC on 25 Feb 1998, for pixels where cloud fraction met or exceeded 5 % (total of 25).

	Mean	Standard Deviation
Omega (Pa s^{-1})	-0.212	0.124
Specific Humidity (g kg^{-1})	0.122	0.059
Temperature (K)	217.5	44.7
Wind Speed (m s^{-1})	53.6	12.2

5.4.4 Case Study: 1999 February 7

On 1999 February 7, the SGP site was embedded in westerly upper-level flow, on the southern edge of the polar jet stream, as shown in Figure 5-28. A trough, which had become more and more shallow after passing through Oklahoma the previous day, was now located over the Mississippi valley. A cold/stationary front stretched from the low pressure center off the coast of Virgina, westward across southern Oklahoma. A weak ridge of high pressure (1016 hPa) was located over western Indiana, but the ridge extended southwestward over the SGP site. The 300 hPa wind speed on the southern edge of the jet, above the radar, is estimated to have been 30 m s^{-1} (58 kts).

Observations from the MMCR radar (Figure 5-29) show that convection and low clouds earlier in the day had diminished by 12 UTC, and by 15 UTC high cloud fragments appeared at approximately 9 km. By 17 UTC, a more steady, higher cloud began to develop at about 10 km (roughly 300 hPa). Periodic pulses in radar reflectivity, that extended through the depth of the cloud, were evident during this development period. The cloud grew thicker and higher until 22 UTC, when the cloud base dropped rapidly. Optical depth data were available until only 23:07 UTC. The cloud optical

depth is shown to vary from 0 to 5; the greatest optical thickness occurred rather early in the cloud lifecycle, and was on the order of one when the base lowering described above occurred. Doppler velocities were weakly upward, and on the order of 0.5 m s^{-1}.

Microphysical parameters derived from the tau-Z retrieval are shown in Figure 5-30. Several retrieved profiles at the end of the time period of interest were rejected by the chi-squared significance test (Figure 5-33). These points had chi-squared values that were too low to satisfy the 0.1% significance test. According to Equation 5.5, this probably indicates that the specified uncertainties in the measurements or a priori parameter were too great; although the retrieval did converge at these points, they were rejected by the quality check.

The retrieved characteristic diameters were on the order of 40 to 50 μm until 22 UTC, and then some ice crystals as large as 92 μm were retrieved. During the period of activity after 22 UTC, the average diameter became as large as 64 μm (Figure 5-31). The average ice crystal number concentration over the period of study was 8.475×10^3 m^{-3}. After 22 UTC, the mean number concentration decreased to a minimum and then increased again, while the average ice crystal diameter increased steadily.

Ice water content seldom exceeded 0.2 g m^{-3} until after 22 UTC, when it reached a maximum value of 0.047. The IWP before 22 UTC varied around a mean of 7.5 g m^{-2}, and quickly exceed 80 g m^{-2} as the cloud base lowered and reflectivity increased. This was certainly a time of rapid ice particle generation.

The scatter plot of IWC versus radar reflectivity (Figure 5-32) shows a large clustering of points that represent the lower temperature regimes (less than –40 °C). The highest reflectivity returns, presumably from the after 22 UTC, had the highest ice water

contents and occurred at the highest temperatures. This is consistent with the observed cloud lowering toward the lower troposphere and the higher temperature environment found there.

The coefficients of the power-law relation IWC = a Z^b that are derived from the scatter are:

$$a = 0.0241301$$

$$b = 0.460083$$

with a correlation coefficient of 0.86.

The EDAS model output is shown in Figure 5-34. The convection early in the day was represented in both the cloud fraction and omega fields. Synoptic ascent was replaced by strong subsidence at 05 UTC. This corresponded well with the time of frontal passage. The low cloud visible on radar between 08 and 13 UTC was also represented by the model, although EDAS shows the cloud persisted considerably longer than it actually did. The high cloud, which is our primary interest, was also present in the EDAS output. The 300 hPa EDAS wind at 23 UTC was 28.7 m s^{-1} (54.5 kts), comparable to the estimate from the analysis (30 m s^{-1}).

A vertical sounding from 18 UTC, about the time the main cloud feature began to take shape, is shown in Figure 5-35. Ascending vertical motion was diagnosed at and just below cloud level at this time, equal in magnitude to the sinking in the lower and middle troposphere. A slight specific humidity anomaly, on the order of 0.1 g kg^{-1}, was apparent in the humidity profile at cloud level. The cloud itself was associated with a radiative heating of just over 2.5 K day^{-1}.

Further quantification of vertical motion is given by profiles of vertical motion at 16, 18, 21, and 23 UTC (Figure 5-36). While subsidence dominated the lower troposphere at all times, rising on the order of 0.1 Pa s^{-1} was diagnosed during the formative hours of the cloud deck (16 and 18 UTC). Cloud level vertical motion was neutral at 21 UTC and upward at 23 UTC. The double maxima of upward motion are noteworthy at three of the four times; one maximum occurred at or near cloud level, and the other just below the tropopause.

Information on the EDAS-derived environment surrounding the cloud is summarized by Table 5-5. Cloud-level vertical motion was, on average, slightly upward, although very nearly neutral.

Table 5-5: EDAS-derived environmental statistics for cirrus layer between 13 and 23 UTC on 25 Feb 1998, for pixels where cloud fraction met or exceeded 5 % (total of 37).

	Mean	Standard Deviation
Omega (Pa s^{-1})	-0.003	0.079
Specific Humidity (g kg^{-1})	0.052	0.048
Temperature (K)	212.2	36.6
Wind Speed (m s^{-1})	32.9	6.6

5.4.5 Case Studies: 13 November 1998 – Parts I and II

These cases are two samples taken from the same day. The division is based on the availability of optical depth data, being divided into an early case and a late case. Part I, the early case, is defined as the period between 02:50 and 06:14 UTC; the optical thicknesses for this case are lidar-derived. Part II, the late case, occurred between 14:11

UTC and 18:36 UTC. This includes both the dissipation of this earlier cloud structure and the development of a new cirrus cloud. Optical thickness estimates from this later case are derived from MFRSR data. Radar data for the entire day are shown in Figure 5-37.

Since this case is divided into two parts, there will be a small departure from the format of the previous cases. The dynamical analyses for the entire day will be presented first. This will be followed by separate analyses of the radar and microphysical properties of the cirrus layer during the early and late cases (parts I and II). Finally, a treatment of the environmental conditions from the EDAS model will be presented jointly for both portions of this case.

Dynamical Analysis – Parts I and II

A broad southwesterly jet stretched from the Mexican plateau through New England on 13 November 1998 (Figure 5-38). This jet was actually the southern branch of a dual-jet system, and was confluent with the northern jet along the east coast of the United States. The horizontal location of the jet remained fairly stationary throughout the day, and the SGP site remained very close the to accelerating region of the jet axis. The 300 hPa wind speed over the SGP site is estimated to have been 45 m s^{-1} (87 kts) at 00 UTC and 40 m s^{-1} (80 kts) at 12 UTC. The wind direction remained southwesterly during the entire day, but shifted slightly more southerly by 12 UTC.

The surfaces analyses at 00 and 12 UTC show a relatively stationary pressure trough remained over western Oklahoma for most of the day. This trough was the focus of a wind shift line, with southeasterly winds to the east of the trough and generally

lighter, more northerly winds to the west of the trough. Pressure troughs such as this are often responsible for enhancing surface convergence resulting in the generation of uplift in the region of the trough.

Radar and Microphysical Analysis – Part I

For the early case, the time-height radar cross section is shown in Figure 5-39. This is in the formative stages of cloud growth. Over the course of just over three hours, the cloud lowered and the cirrus later thickened. Cloud base dropped from about 10.5 km to 9.0 km, while cloud top remained at a nearly constant 11.5 km throughout this portion of the case. Cloud reflectivity varied from –37.3 dBZ to –13.6 dBZ. Doppler velocities were slightly positive (upward) or neutral.

Results of the retrieval or IWC and characteristic diameter are given in Figure 5-40. Breaks in the cloud represent retrievals that did not converge to a solution. Characteristic diameter was on the order of 20-30 μm until just after 05 UTC, when it increased to 35-45 μm. This increase in ice crystal diameter was simultaneous with a surge in radar reflectivity, and then, shortly thereafter, an increase in optical depth. Ice water content in the cloud rarely exceeded 0.003 g m^{-3} until after 05 UTC, during which time it maximized at 0.0063 g m^{-3}.

The mean number concentration (Figure 5-41) showed an overall decrease from cloud formation until before 05 UTC, when it reached a minimum, peaked again just after 05 UTC, and then slowly decreased. This 05 UTC peak is also visible in the retrieved IWC profile; both maximized simultaneously at this time. The mean characteristic diameter showed a generally opposite trend to the number concentration, and maximized

at roughly the same time that the mean characteristic diameter was minimized. Ice water path averaged 1.72 g m^{-2} prior to 05 UTC, and 3.46 g m^{-2} after.

The resulting IWC-Z relation is given in Figure 5-42. Although many of the highest temperature radar returns occur at higher reflectivities, there is no apparent relation between temperature and IWC. The coefficients of the power-law relation $IWC = a Z^b$ that are derived from the scatter are:

$$a = 0.0115250$$

$$b = 0.343549$$

with a correlation coefficient of 0.51.

The chi-squared quality check rejected no retrieved profiles, although not all profiles converged.

Radar and Microphysical Analysis – Part II

The radar data for the later case is shown in Figure 5-43. The dissipating stage of the cloud examined in Part I was still present at 15 UTC. Another cloud deck developed at about 16:30 UTC and persisted for about three hours. Cloud tops were uniformly on the order of 10.5 km, with cloud base averaging approximately 9.0 km. The only noteworthy exception was the dissipating cloud early in the period, which had a rapid increase in cloud base height and then quickly dissipated. Radar reflectivity was highest near cloud base, probably indicating the largest ice particles were located here. Dopper-derived particle velocities within the clouds were, on average, upwards at approximately 0.5 m s^{-1}. Downward or neutral velocities (less than 0.25 m s^{-1}) were most likely to be

found near cloud top, and a few regions of stronger upward velocity (around 1.0 m s^{-1}) were evident near cloud base.

Unfortunately, the temporal resolution of the optical depth data were highly non-uniform and at times behaved sporadically. For example, during the cloudless period between 15 and 16:30 UTC, the MFRSR reported non-zero values of optical depth, which is non-physical and as such a curiosity, but this was non-detrimental to the retrieval since there were no radar returns during this time period; the retrieval simply did not converge and nothing was retrieved. Optical depth information was missing for the beginning stages of development of the longer-lived cloud at 16:30 UTC, so the retrieval produced its first output for this cloud at 17:11.

The ice water content maximum just after 17:30 UTC (Figure 5-44) occurred during a sudden upward spike of radar reflectivity extending from cloud base. This was simultaneous with an optical depth maximum of 4.86. During this maximum, IWC reached 0.028 g m^{-2}, well above the more typical values of 0.005 to 0.015. Ice crystals with the greatest characteristic diameter were consistently located near cloud base, as suggested by the radar reflectivity. Mean number concentration and mean characteristic diameter tended to vary inversely with one another (Figure 5-45) showing a tendency toward a greater number of small drops as the cloud dissipated, presumably as ice saturation within the cloud decreased and ice particles began to sublimate. The mean value of D_n in the developing cloud was a relatively large 42.0 μm. Ice water path was 15-16 g m^{-2} during the early stages of cloud development, jumped to 40.2, and then decreased to 2.1 for the last profile.

The resulting IWC-Z relation is given in Figure 5-46. A relatively tight fit of the regression line is noted. The coefficients of the power-law relation IWC = a Z^b that are derived from the scatter are:

$$a = 0.0274351$$

$$b = 0.475786$$

with a correlation coefficient of 0.95.

The chi-squared quality check rejected no retrieved profiles.

EDAS-derived Environment

The EDAS model did a poor job in positioning the cirrus cloud layers of interest, and also showed multiple lower cloud layers where they did not exist, as determined by radar observations (Figure 5-47). For example, EDAS diagnosed three distinct cloud layers that persisted through the entire day. Although the radar observed a few cloud fragments that appeared periodically at about 4.5 km, only one primary cloud layer developed at any one time. It appears that EDAS placed the main cirrus layer higher than it actually occurred, at least until after 15 UTC, and overestimated its vertical extent. For this reason, no attempt has been made to derive the statistical average quantities, such as those found in Table 5-2, for part I of this case.

EDAS diagnosed neutral or weakly upward vertical motion throughout most of the troposphere after 9 UTC. However, a general synoptic scale uplift was present above 300 hPa the entire day. A vertical sounding though the cirrus layer is shown in Figure 5-48. The strong uplift discussed above is evident, maximizing at 200 hPa (near but above the cirrus layer) at –0.5 Pa s^{-1}. Later in the day, the 17 UTC vertical profile

showed weaker vertical motion of –0.1 Pa s^{-1}, but this time at an altitude more comparable with the observed cloud height. Strong radiative heating of 6 K day^{-1} is apparent at cloud level, even given that the EDAS-derived cloud fraction was less than 20%. The vertical pressure velocity at four time intervals is shown in Figure 5-49.

Environmental statistics for part II, where the EDAS cloud placement was more reasonable than earlier in the day, are given in Table 5-6. Note the broad synoptic scale mean uplift.

Table 5-6: EDAS-derived environmental statistics for cirrus layer between 13 and 19 UTC (part II) on 13 Nov 1998, for pixels where cloud fraction met or exceeded 5 % (total of 21).

	Mean	Standard Deviation
Omega (Pa s^{-1})	-0.014	0.117
Specific Humidity (g kg^{-1})	0.407	0.300
Temperature (K)	226.8	51.5
Wind Speed (m s^{-1})	30.3	9.8

5.5 Summary of Case Studies

A summary of the findings from the various case studies is present in the table below, and in a brief summary below the table.

Table 5-7: Summary of the six cases studied. Mean EDAS-derived environmental statistics: vertical pressure velocity (Pa s^{-1}), specific humidity (g kg^{-1}), temperature (K), wind (m s^{-1}). Mean cloud statistics: height (km), ice water path (g m^{-2}) (minimum, maximum, mean), column-average particle number concentration (10^3 m^{-3}) (minimum, maximum, mean). Power-law coefficients of the form $IWC = a Z^b$.

	ω	Sp Hum	Temp	Wind	Mean Height	Min/Max/Mean			$IWC = a Z^b$	
						N_t	D_n	IWP	a	b
	(Pa s^{-1})	(g kg^{-1})	(K)	(m s^{-1})	(km)	(10^3 m^{-3})	(μm)	(g m^{-2})		
1998						1.3	15.2	0.7		
Dec 22	0.032	0.047	211.6	70.3	9.37	55.5	84.3	92.3	0.0428728	0.505501
						16.6	42.5	35.3		
1998						1.5	12.9	0.4		
Nov 20	0.104	0.075	212.8	62.2	10.03	79.1	44.1	10.4	0.0119704	0.336223
						15.3	27.7	3.2		
1998						6.3	17.9	1.0		
Feb 25	–0.212	0.122	217.5	53.6	8.48	54.1	67.7	134.0	0.0460823	0.484201
						19.1	44.3	44.9		
1999						1.8	14.1	0.6		
Feb 07	–0.003	0.052	212.2	32.9	9.90	66.8	64.8	83.8	0.0241301	0.460083
						9.6	36.6	10.5		
1998						1.9	14.7	0.8		
Nov 13 (I)	--	--	--	--	10.03	101.2	42.2	8.3	0.0115250	0.343549
						12.5	28.0	2.7		
1998						4.1	16.5	0.6		
Nov 13 (II)	– 0.014	0.407	226.8	30.3	9.31	41.7	50.9	40.2	0.0274351	0.475786
						8.7	39.7	13.8		

- 22 December 1998: The SGP site was in the right entrance region (but very close to the axis of) a strong jet streak, with 300 hPa winds of about 70 m s^{-1}. The case documented the formation of a cirrus layer which experienced rapid thickening, and reached a peak ice water path of over 90 g m^{-2}. The model-diagnosed dynamics at cloud-level were very weak, although the cloud remained well defined for over 12 hours.
- 20 November 1998: A jet stream with 300 hPa winds of 60 to 65 m s^{-1} was over the SGP site, though the radar was in the left entrance region of the jet core. The formation of a cirrus layer was also documented in this case, although reflectivities and IWC's were, on average, an order of magnitude less than in the previous case.

Weak although non-trivial subsidence was diagnosed by the model, and this may be related to the smaller ice content of the cloud.

- 25 February 1998: The SGP site was nearly aligned with, or slightly to the left of, the axis of the decelerating region of a 50 m s^{-1} jet. A upper level low pressure area and surface front were also located in the vicinity. The cloud of interest started with cirrus-like characteristics, but evolved over several hours into a lower, thicker cloud. It can not be ruled out that the cloud contained non-trivial amounts of liquid water in the later stages. Ice water path exceeded 130 g m^{-2}. Mean characteristic diameter was the largest of all the cases, at approximately 44 μm. Mean upward motion was present over the lifecycle of the cloud, according to the dynamical model, probably enhanced by the upper-level low pressure to the north.
- 1999 February 7: In this case, the SGP site was located in the right-exit region of the jet, well outside the area of maximum winds, which were only about 30 m s^{-1} at 300 hPa. The retrieval captured most of the life-cycle of the cloud. Ice water path remained relatively small, starting at 0.6 g m^{-2} and never exceeding 10.5 g m^{-2}. Very weak mean dynamic lift was diagnosed by the model, although the sign of omega varied from hour to hour.
- 1998 November 13: A moderate jet dropped south over the SGP site during the day, with the site nearly under the jet core at 00 UTC and in the left entrance region at 12 UTC. A surface trough was present over the area for most of the day. In the beginning stages of cloud development (Part I), the cloud was particularly tenuous and had ice water contents from less than 0.002 to 0.006 g m^{-3}. Later (Part II), cloud dissipation was captured and development of a new, rather uniform cirrus layer

began. This cloud had a higher ice water content, exceeding 0.025 g m^{-3} briefly. Weak mean ascent was diagnosed at cloud level. Cloud-level specific humidity in this case was the highest of any of the cases, averaging 0.4 g kg^{-1}.

The results of the regional dynamical analyses clearly demonstrate that the vertical motions that supports jet stream cirrus are weak, and possibility unresolved by the ETA/EDAS model. This is somewhat counterintuitive given the strong dynamical ascent that is associated with the jet streak at lower levels. If the model environmental parameters are to be trusted, these results suggest that other processes, such as horizontal moisture advection, may play a non-trivial role in the formation and maintenance of these clouds.

Finally, the computer values of the power-law coefficients a and b were averaged for all the cases, to obtain new values that may be of some use in studies of jet stream cirrus. These retrieved values are:

$$a = 0.0273360$$

$$b = 0.434224$$

The application of this suggested relationship to each of the six cases is shown in Figure 5-50. The line, on average, represents the data well. The mean absolute error in IWC (relative to the retrieved value) of each of the five power-law relations presented in Table 3.1 is compared with the case-derived relationship and averaged relationship in Figure 5-51. Note that, of course, the relationship derived by the least-square fit specific to the case consistently has the least error. The new, averaged relationship has the next-to-least error in three of the six cases. The spread of ice water contents for each of the

cases is apparent in the figure, but it must be remembered that the errors shown are relative to the retrieved values and not the true values, since the true values are unknown.

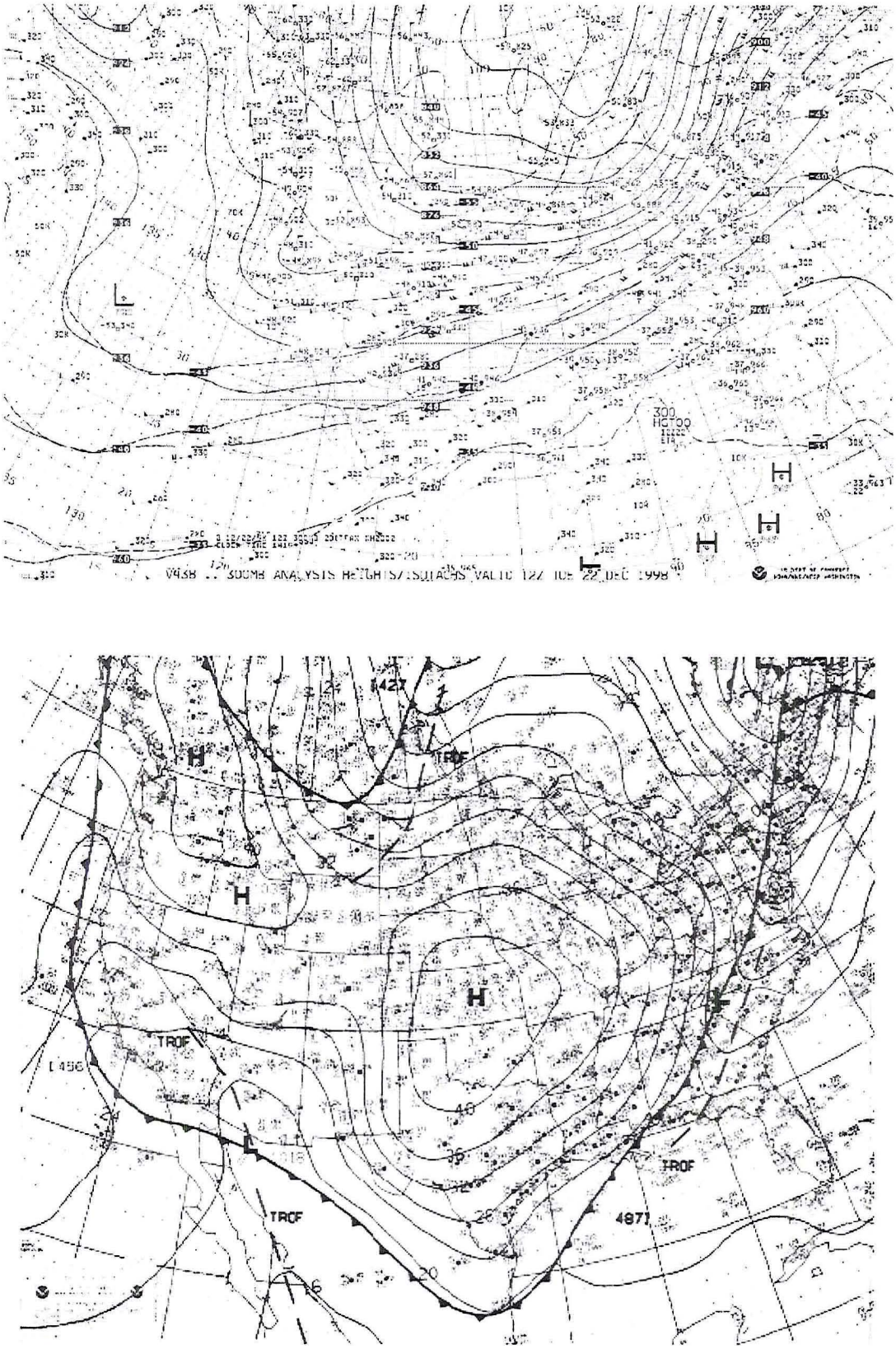

Figure 5-1: (a) Analysis of 300 hPa heights (solid lines) and isotachs (dotted lines) valid 12 UTC 22 Dec 1998. (b) Surface analysis valid 12 UTC 22 Dec 1998.

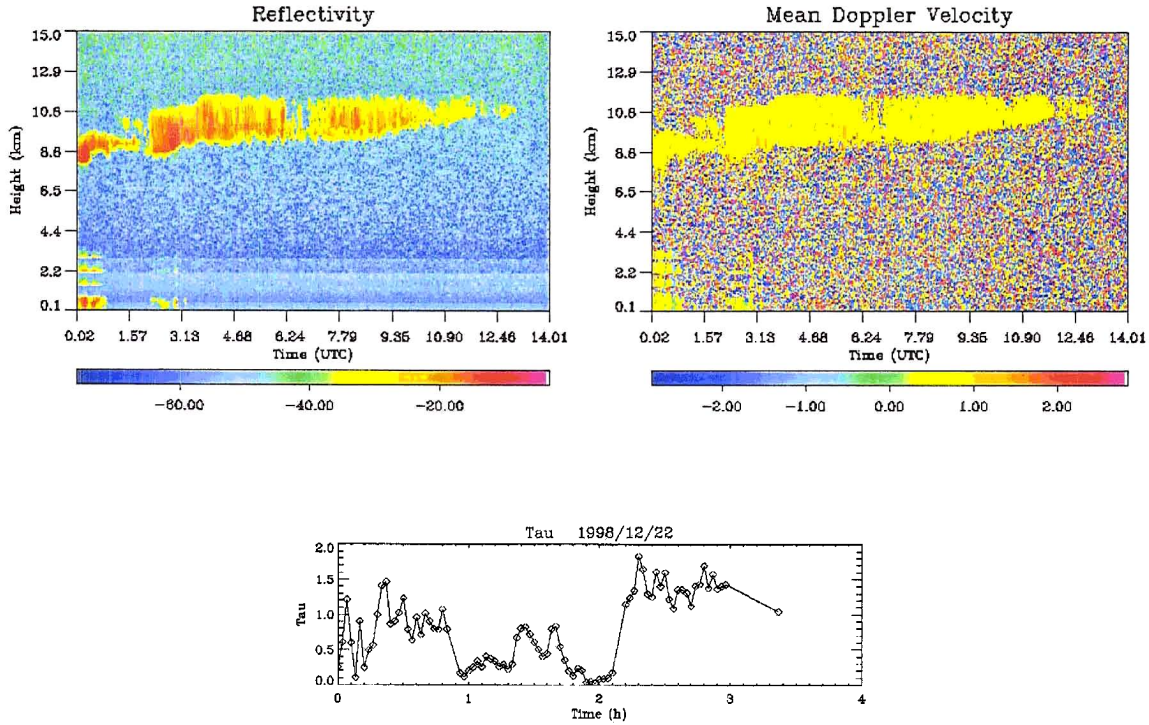

Figure 5-2: Radar reflectivity (dBZ), Doppler velocity (m s^{-1}), and estimated optical depth. Case 22 Dec 1998.

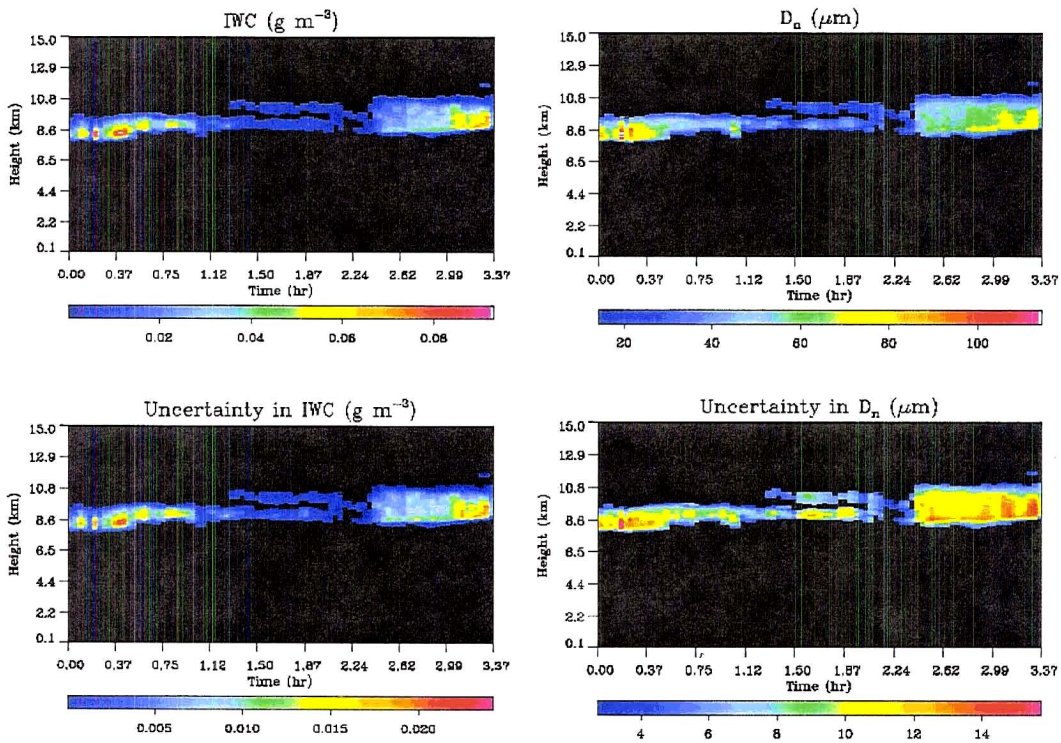

Figure 5-3: Retrieved IWC (g m^{-3}) and characteristic diameter (μm) and the associated uncertainties. Case 22 Dec 1998.

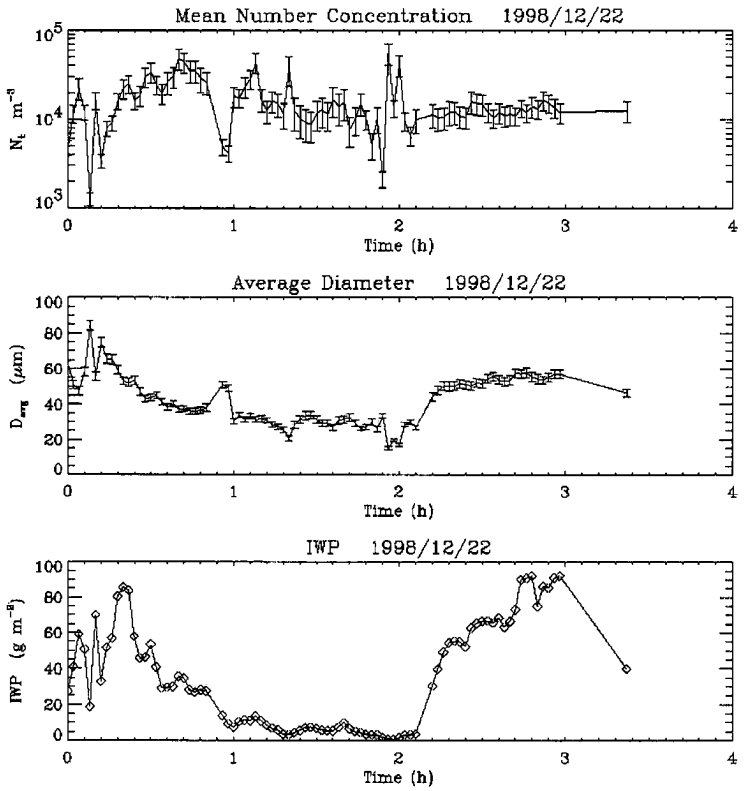

Figure 5-4: Retrieved number concentration N_t (m^{-3}), average characteristic diameter D_{avg} (μm), and column ice water path (g m^{-2}). Case 22 Dec 1998.

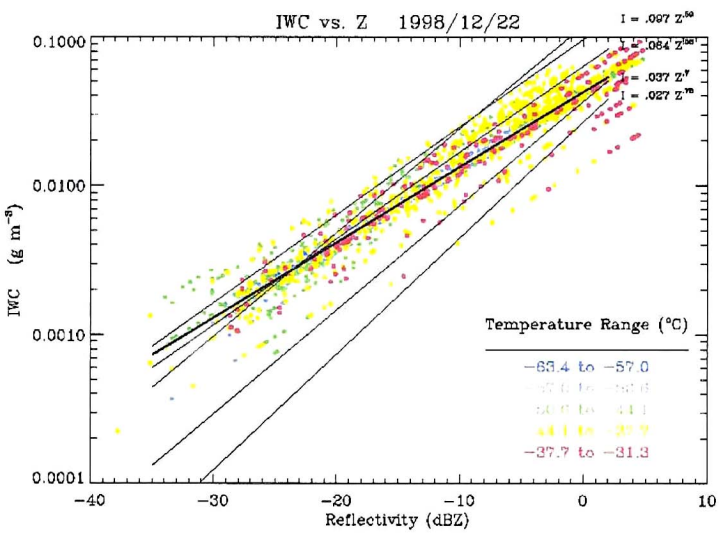

Figure 5-5: Scatter plot of ice water content (g m^{-3}) versus radar reflectivity (dBZ), color coded according to radiosonde observation of environmental temperature. A few common IWC-Z power law relations are provided for reference. Case 22 Dec 1998.

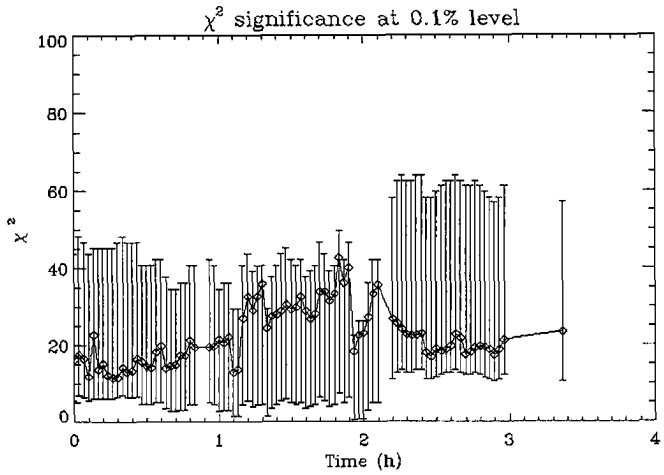

Figure 5-6: Chi-squared value of the retrieval (points and solid line). The bars show the maximum and minimum value of chi-squared that would be allowable for a "quality" retrieval at the 0.1% level given the degrees of freedom of each profile. Points that lie outside the bars are rejected by the retrieval.

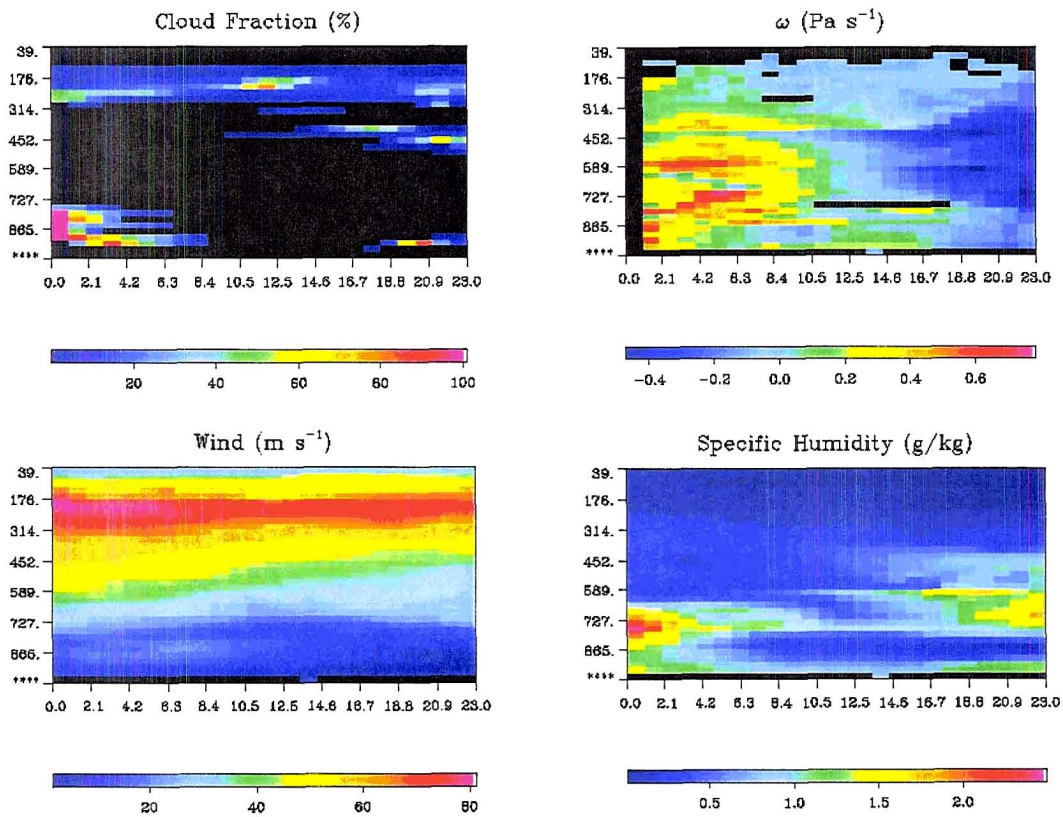

Figure 5-7: EDAS output for 22 Dec 1998. Clockwise from upper left: cloud fraction, omega (Pa s^{-1}), specific humidity (g kg^{-1}), wind speed (m s^{-1}).

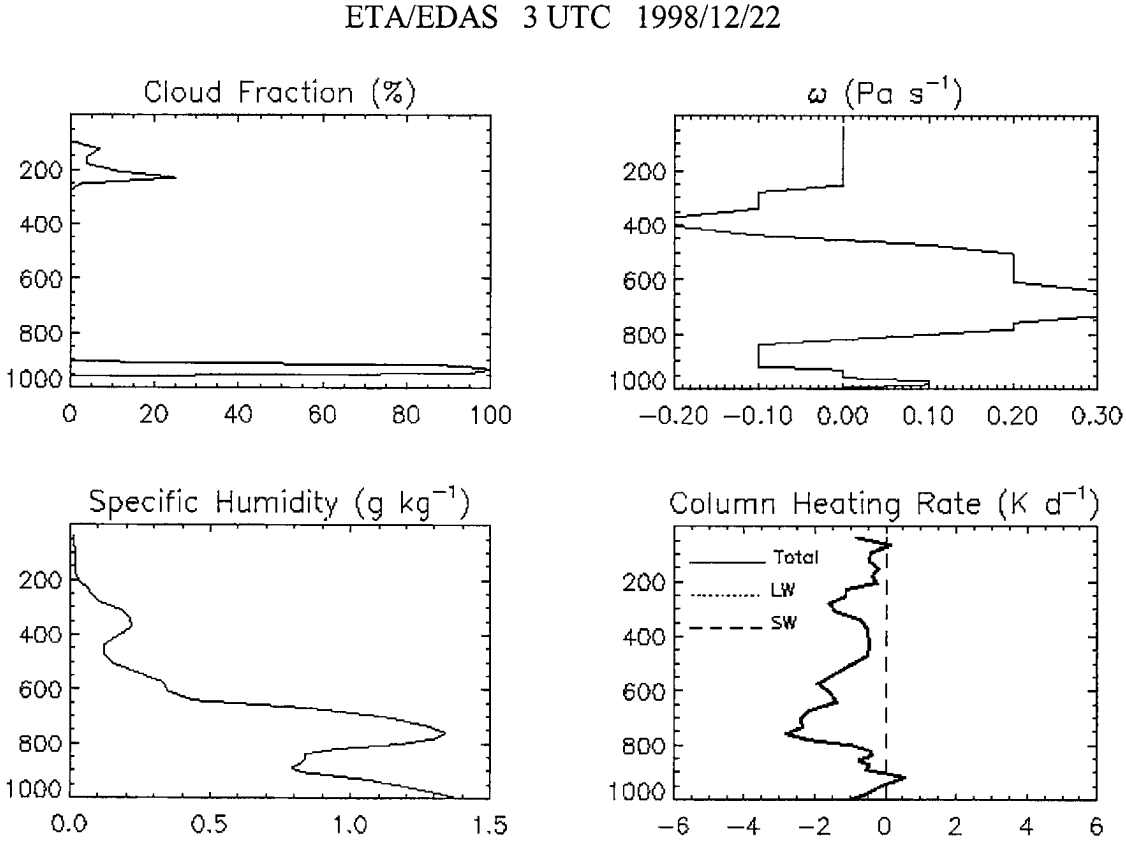

Figure 5-8: EDAS vertical profiles of cloud fraction, omega (Pa s^{-1}), and column radiative heating rate (K day^{-1}), from 03 UTC Case 22 Dec 1998.

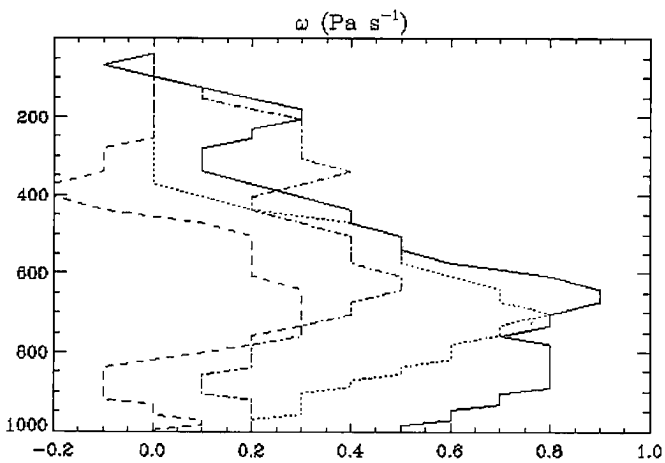

Figure 5-9: EDAS vertical motion profiles for 01 (solid line), 02 (dotted line), 03 (dashed line), and 04 UTC (dot-dash line) on 22 Dec 1998.

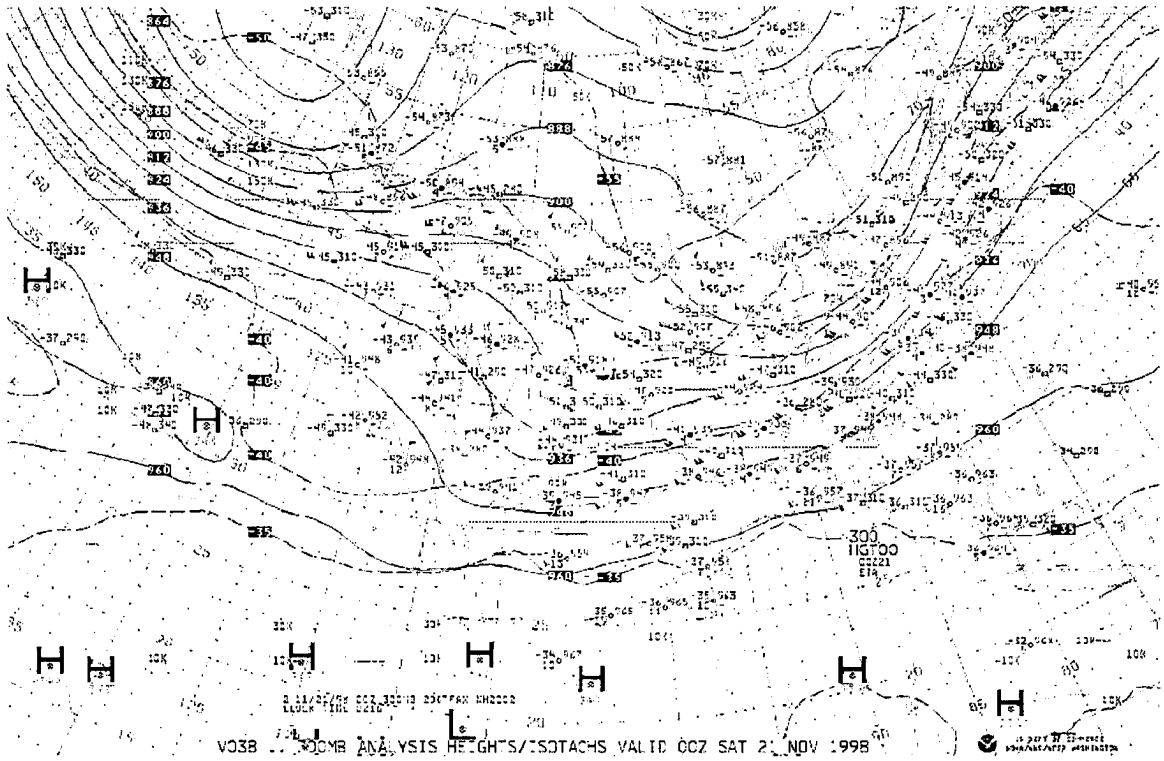

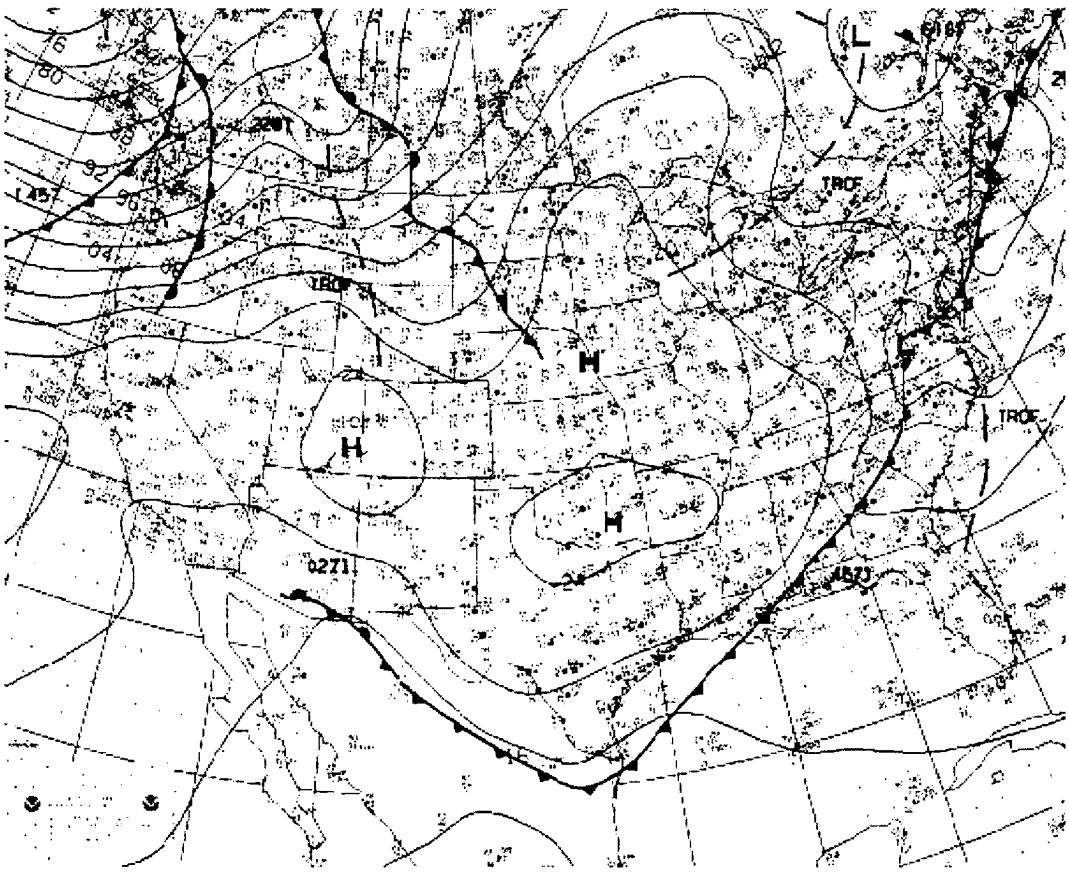

Figure 5-10: (a) Analysis of 300 hPa heights (solid lines) and isotachs (dotted lines) valid 00 UTC 21 Nov 1998. (b) Surface analysis valid 00 UTC 21 Nov 1998.

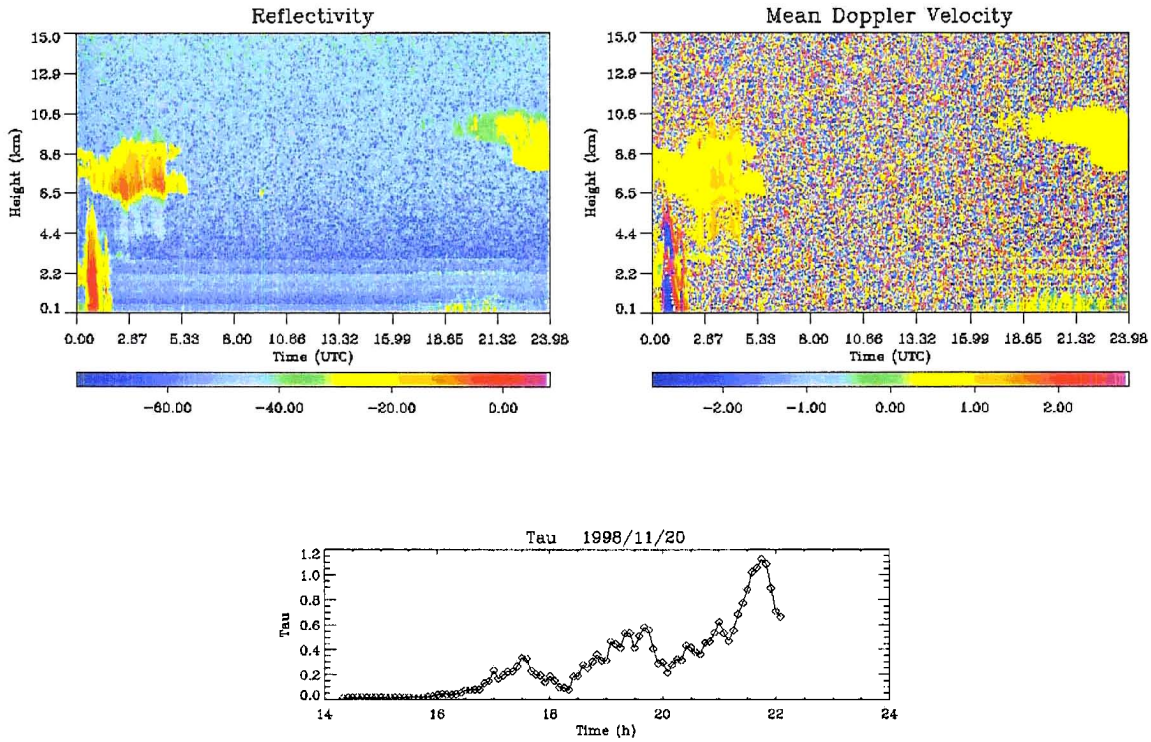

Figure 5-11: Radar reflectivity (dBZ), Doppler velocity (m s^{-1}), and estimated column optical depth. Case 20 Nov 1998.

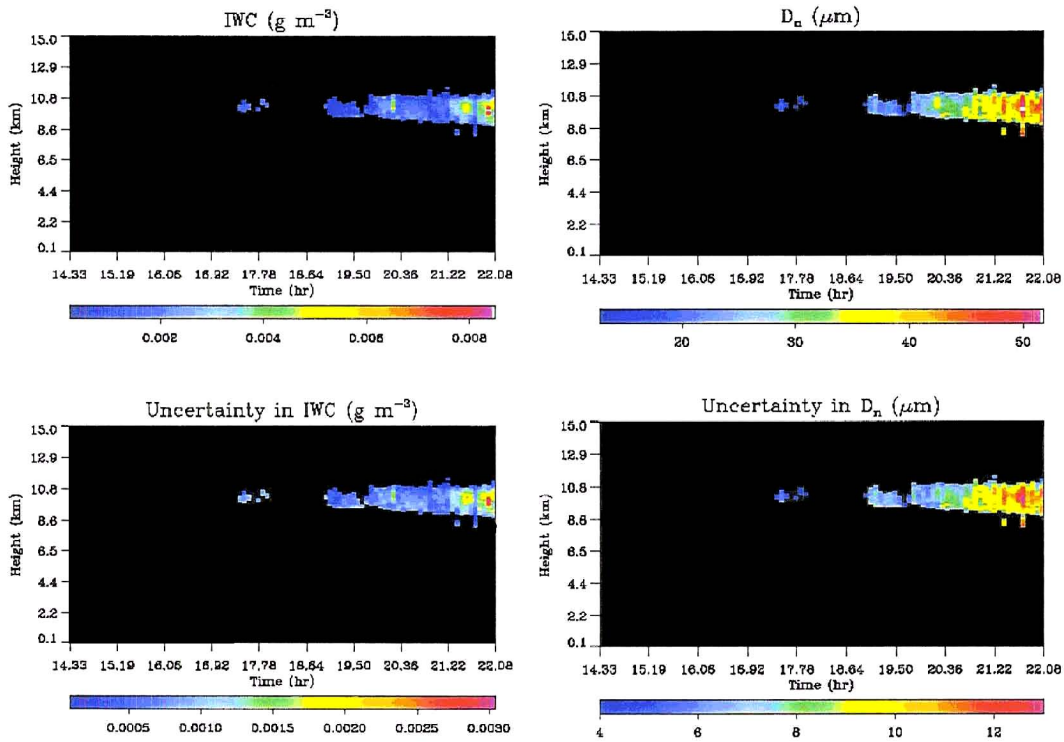

Figure 5-12: Retrieved IWC (g m^{-3}) and characteristic diameter (μm) and the associated uncertainties. Case 20 Nov 1998.

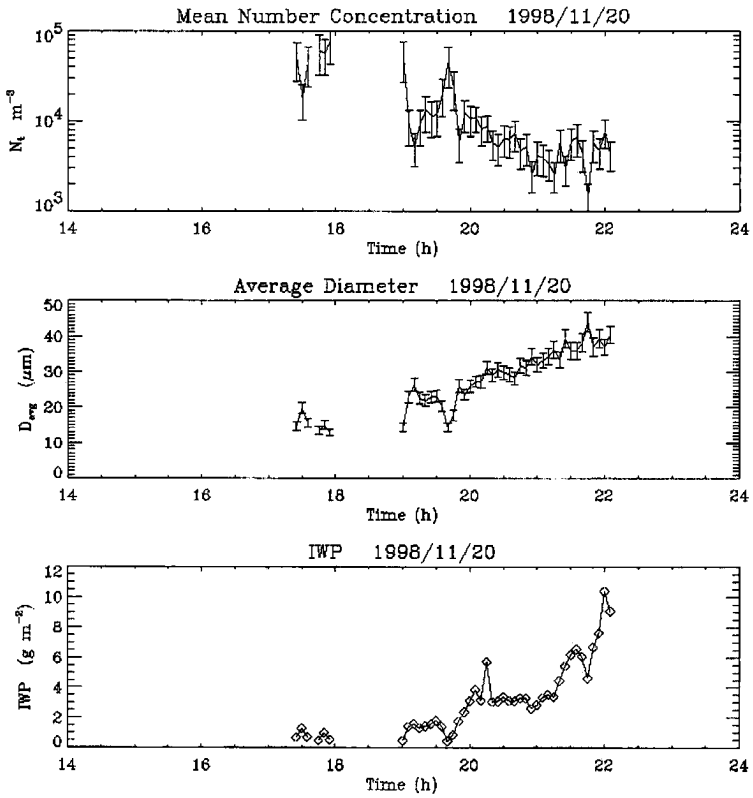

Figure 5-13: Retrieved number concentration N_t (m^{-3}), average characteristic diameter D_{avg} (μm), and column ice water path (g m^{-2}). Case 20 Nov 1998.

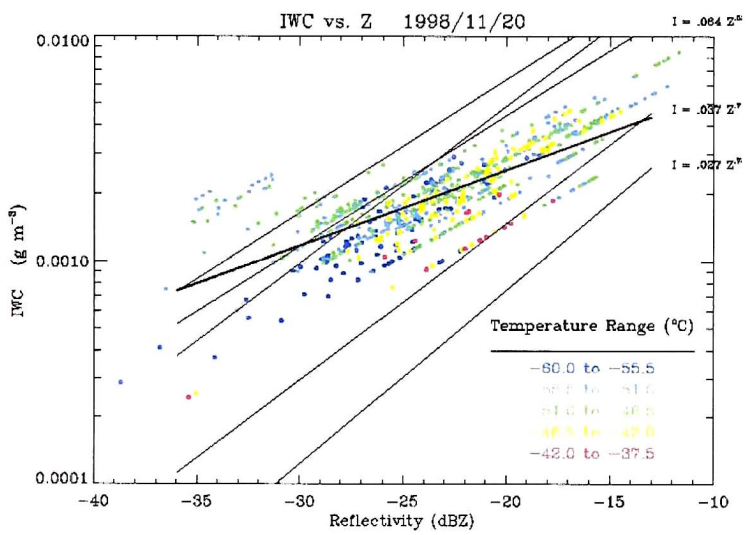

Figure 5-14: Scatter plot of ice water content (g m^{-3}) versus radar reflectivity (dBZ), color coded according to radiosonde observation of environmental temperature. A few common IWC-Z power law relations are provided for reference. Case 20 Nov 1998.

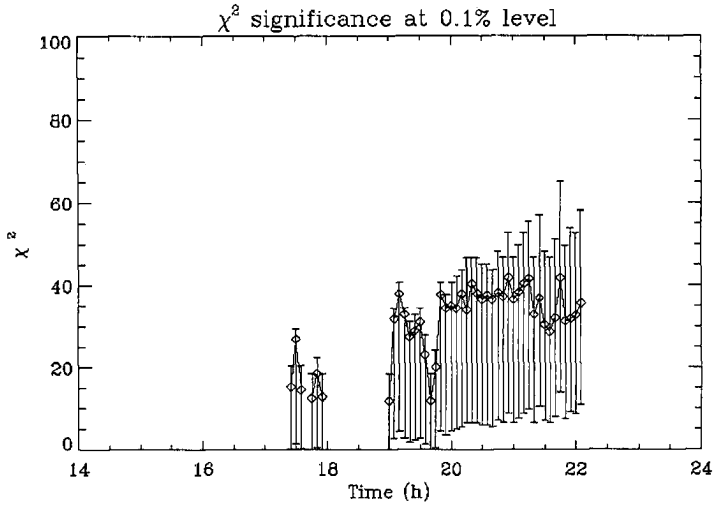

Figure 5-15: Chi-squared value of the retrieval (points and solid line). The bars show the maximum and minimum value of chi-squared that would be allowable for a "quality" retrieval at the 0.1% level given the degrees of freedom of each profile. Points that lie outside the bars are rejected by the retrieval. Case 20 Nov 1998.

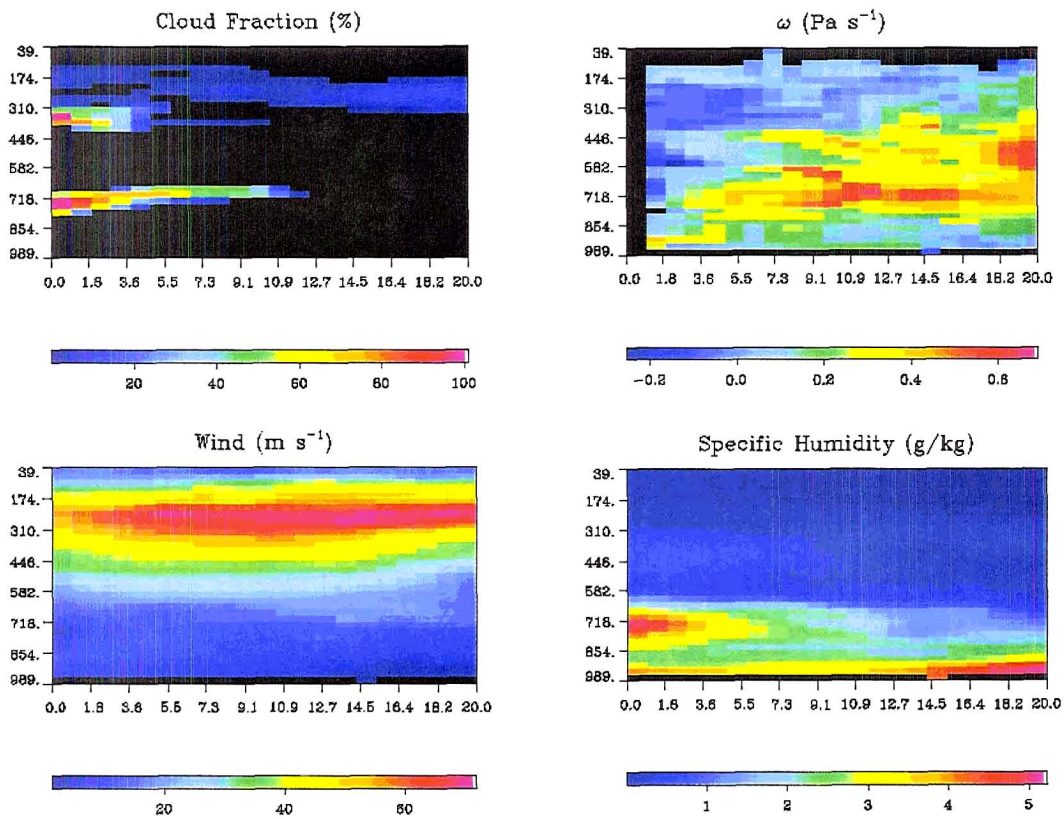

Figure 5-16: EDAS output for 20 Nov 1998. Clockwise from upper left: cloud fraction, omega (Pa s^{-1}), specific humidity (g kg^{-1}), wind speed (m s^{-1}).

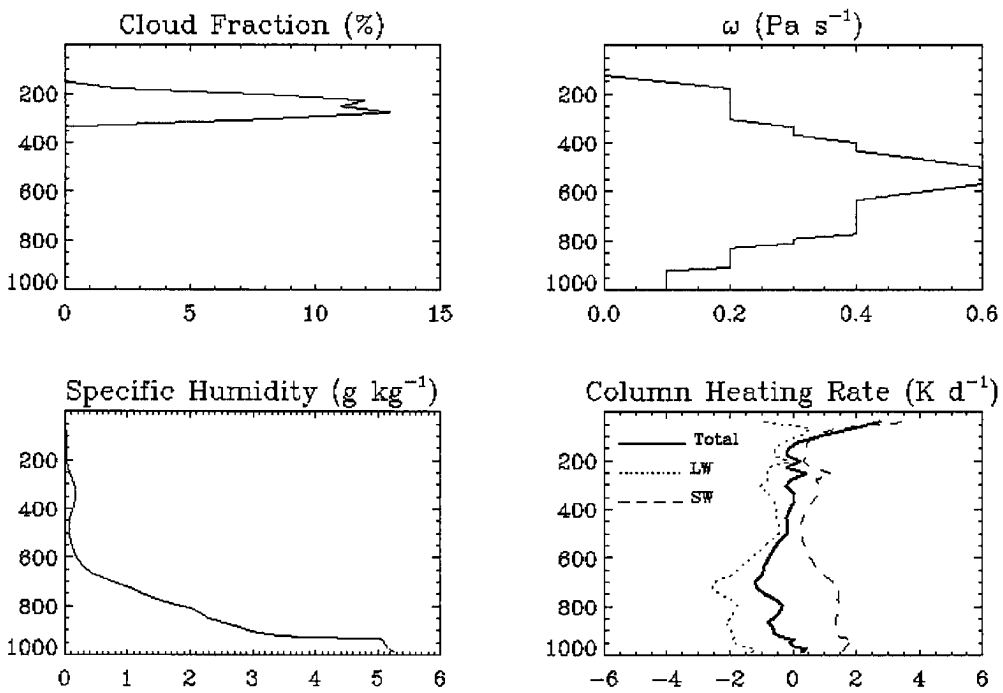

Figure 5-17: EDAS vertical profiles of cloud fraction, omega (Pa s^{-1}), and column radiative heating rate (K day^{-1}), from 20 UTC. Case 20 Nov 1998.

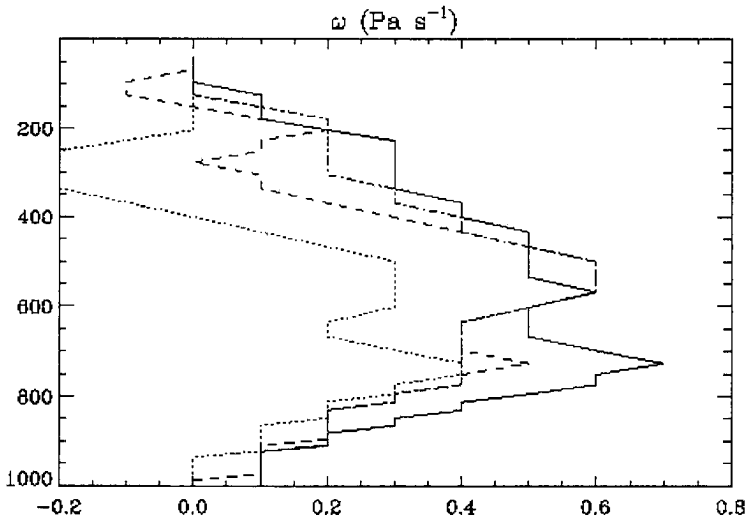

Figure 5-18: EDAS vertical motion profiles for 17 (solid line), 18 (dotted line), 19 (dashed line), and 20 UTC (dot-dash line) on 20 Nov 1998.

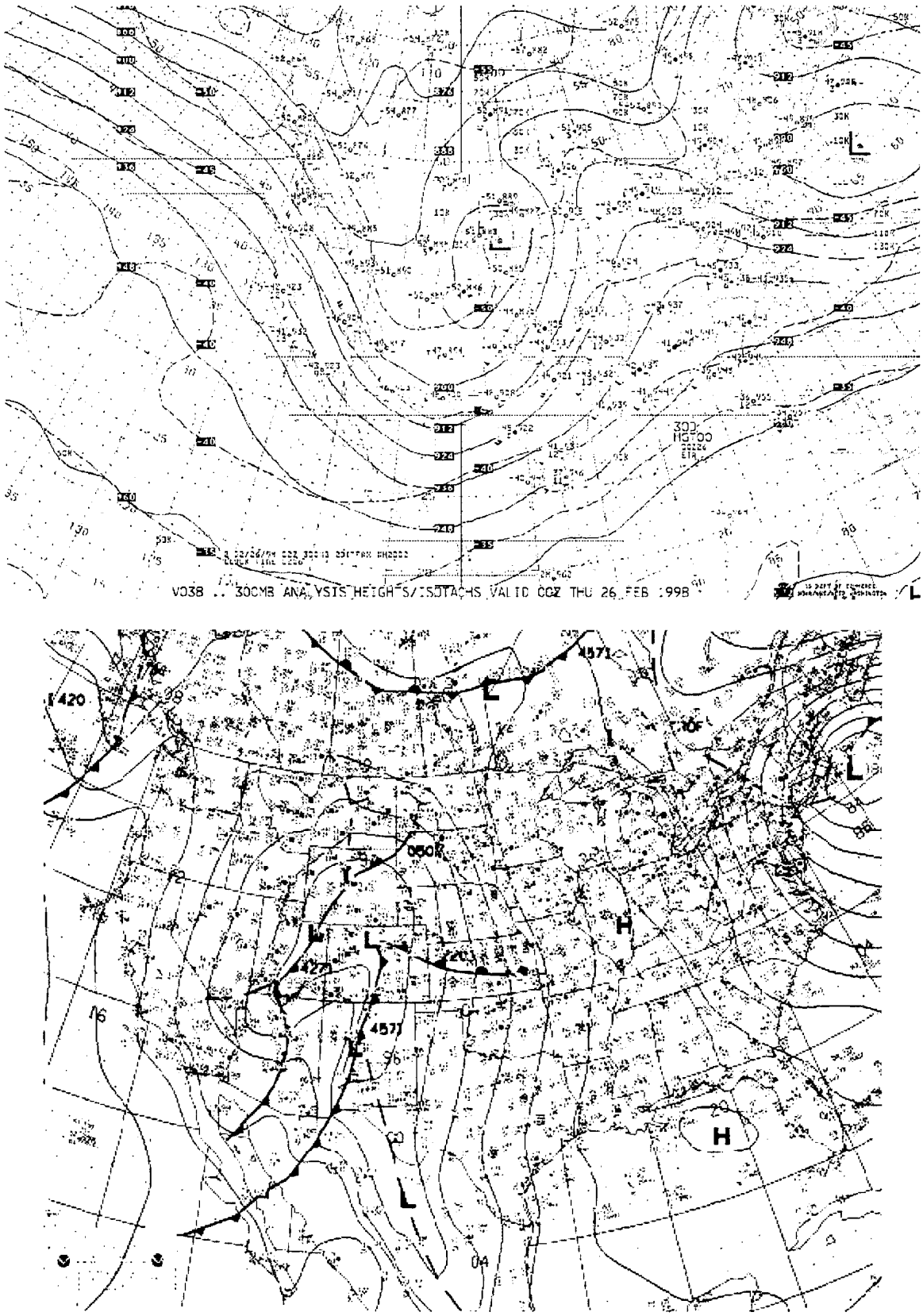

Figure 5-19: (a) Analysis of 300 hPa heights (solid lines) and isotachs (dotted lines) valid 00 UTC 26 Feb 1998. (b) Surface analysis valid 00 UTC 26 Feb 1998.

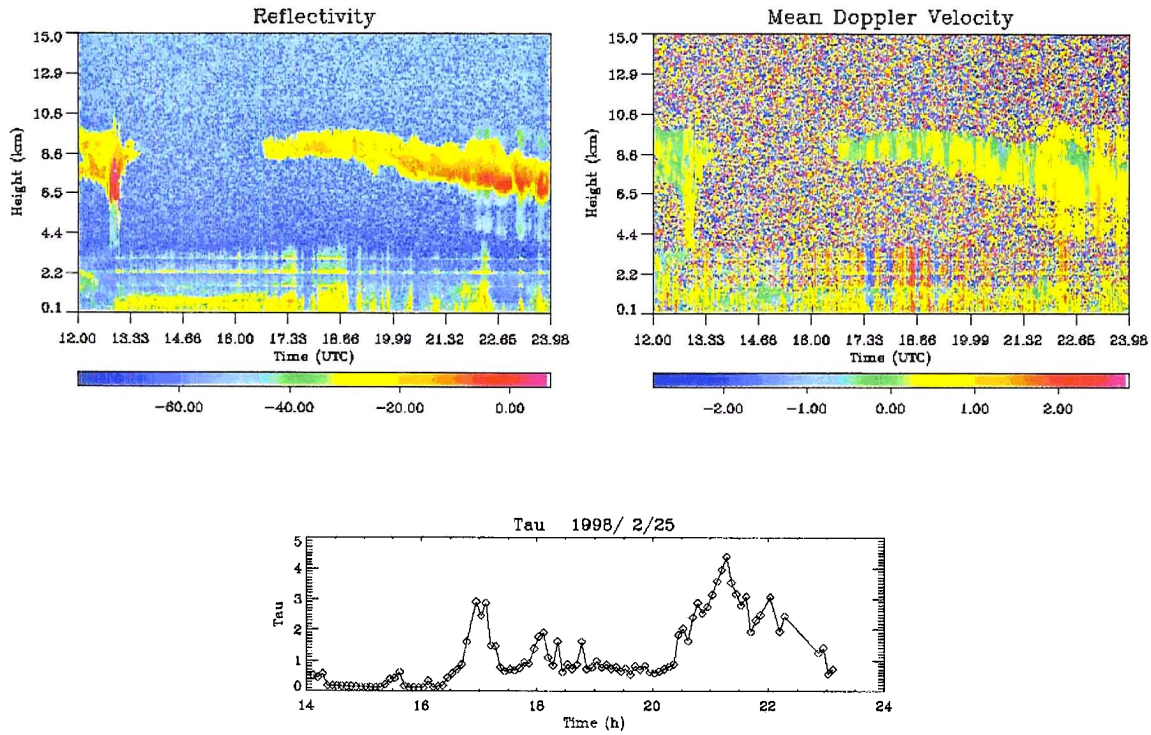

Figure 5-20: Radar reflectivity (dBZ), Doppler velocity (m s^{-1}), and estimated column optical depth. Case 25 Feb 1998.

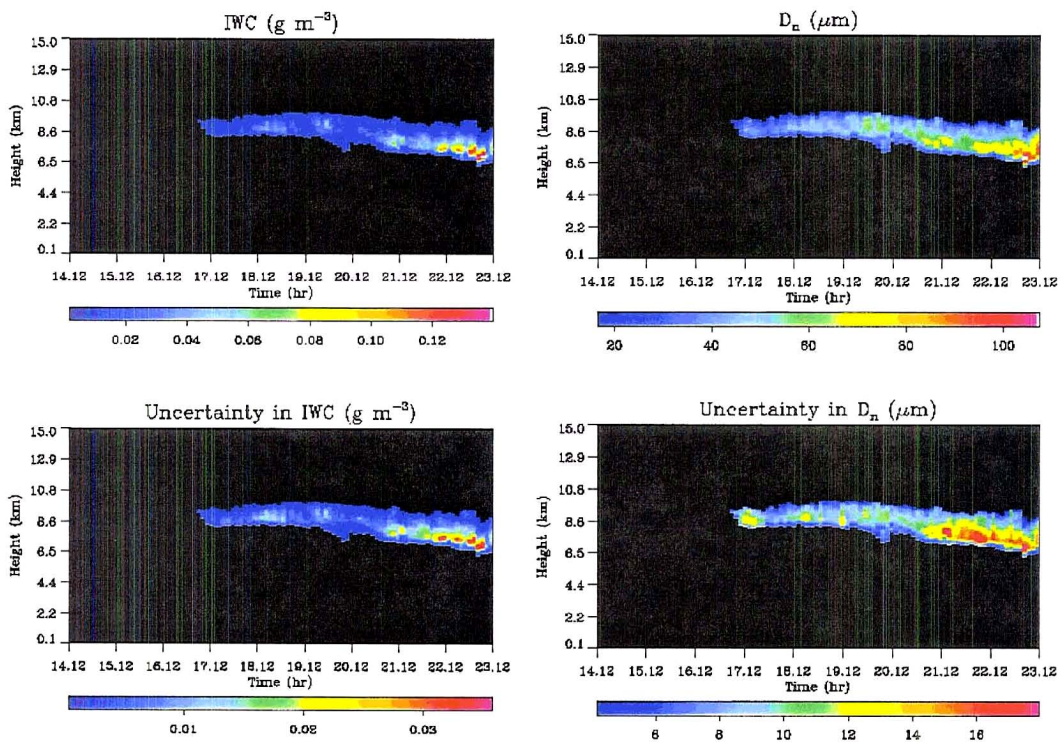

Figure 5-21: Retrieved IWC (g m^{-3}) and characteristic diameter (μm) and the associated uncertainties. Case 25 Feb 1998.

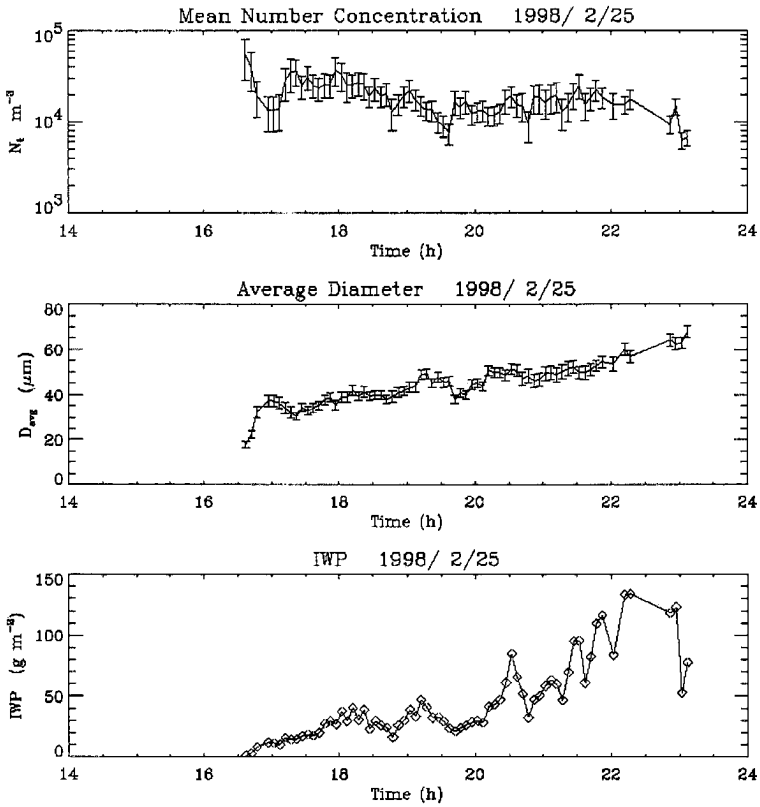

Figure 5-22: Retrieved number concentration N_t (m^{-3}), average characteristic diameter D_{avg} (μm), and column ice water path (g m^{-2}). Case 25 Feb 1998.

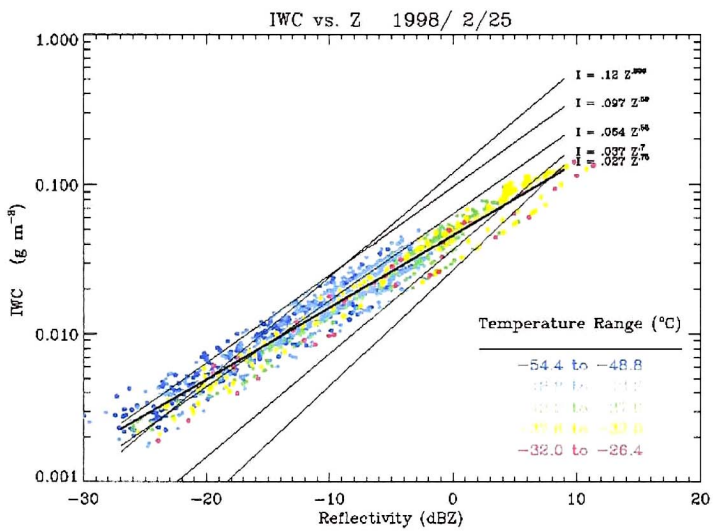

Figure 5-23: Scatter plot of ice water content (g m^{-3}) versus radar reflectivity (dBZ), color coded according to radiosonde observation of environmental temperature. A few common IWC-Z power law relations are provided for reference. Case 25 Feb 1998.

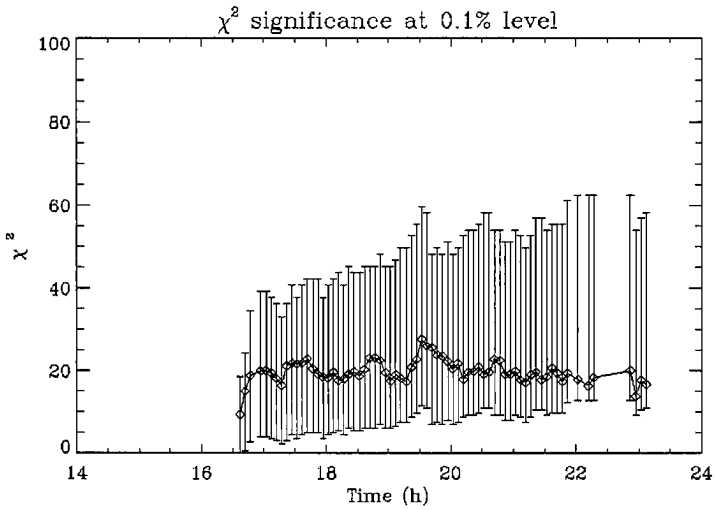

Figure 5-24: Chi-squared value of the retrieval (points and solid line). The bars show the maximum and minimum value of chi-squared that would be allowable for a "quality" retrieval at the 0.1% level given the degrees of freedom of each profile. Points that lie outside the bars are rejected by the retrieval. Case 25 Feb 1998.

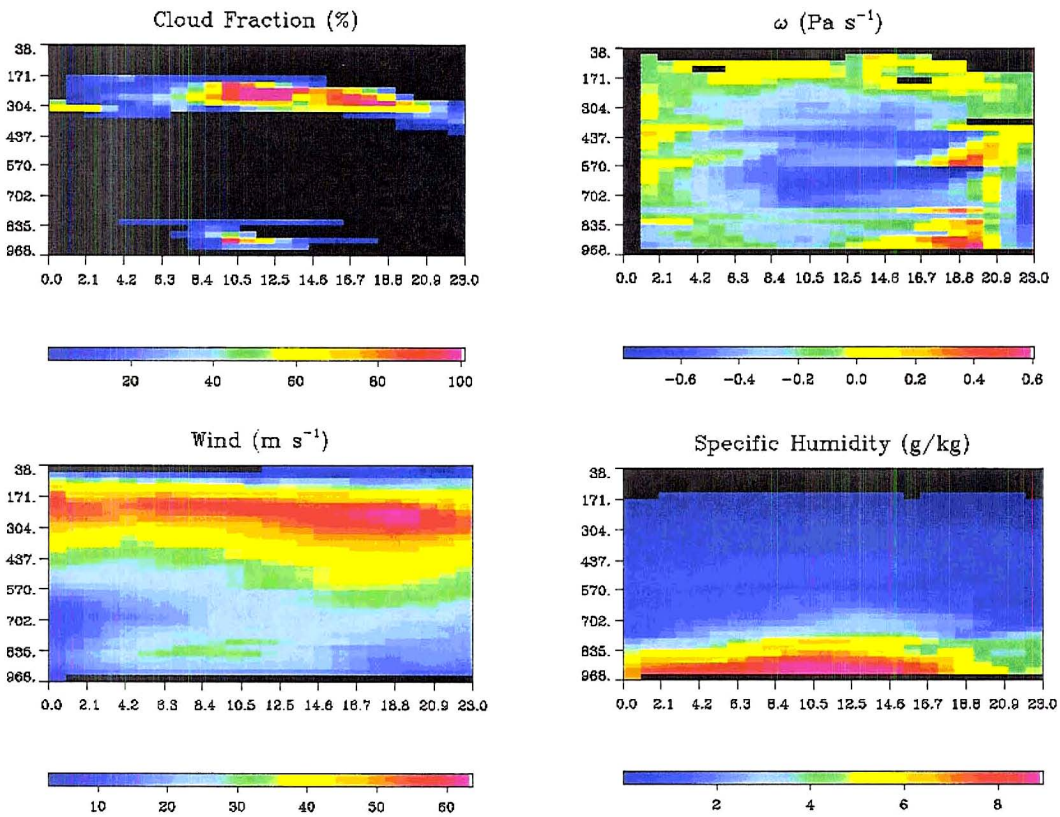

Figure 5-25: EDAS output for 25 Feb 1998. Clockwise from upper left: cloud fraction, omega (Pa s^{-1}), specific humidity (g kg^{-1}), wind speed (m s^{-1}).

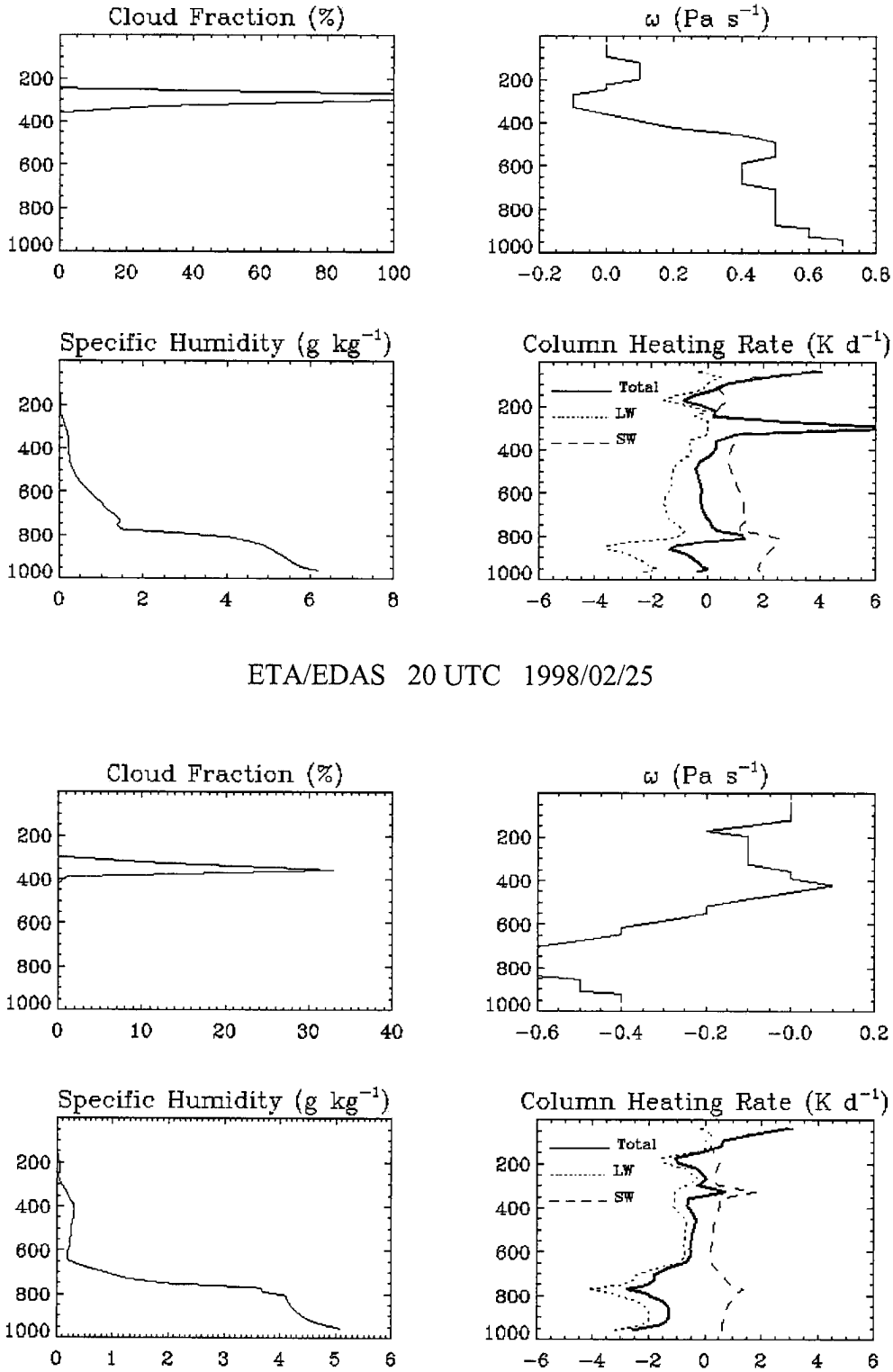

Figure 5-26: EDAS vertical profiles of cloud fraction, omega (Pa s^{-1}), and column radiative heating rate (K day^{-1}), for 19 and 23 UTC. Case 25 Feb 1998.

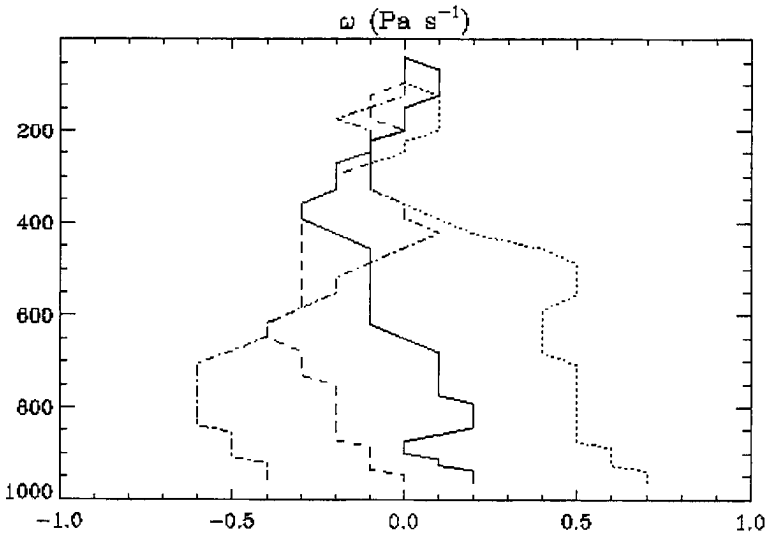

Figure 5-27: EDAS vertical motion profiles for 17 (solid line), 19 (dotted line), 21 (dashed line), and 23 UTC (dot-dash line) on 25 Feb 1998.

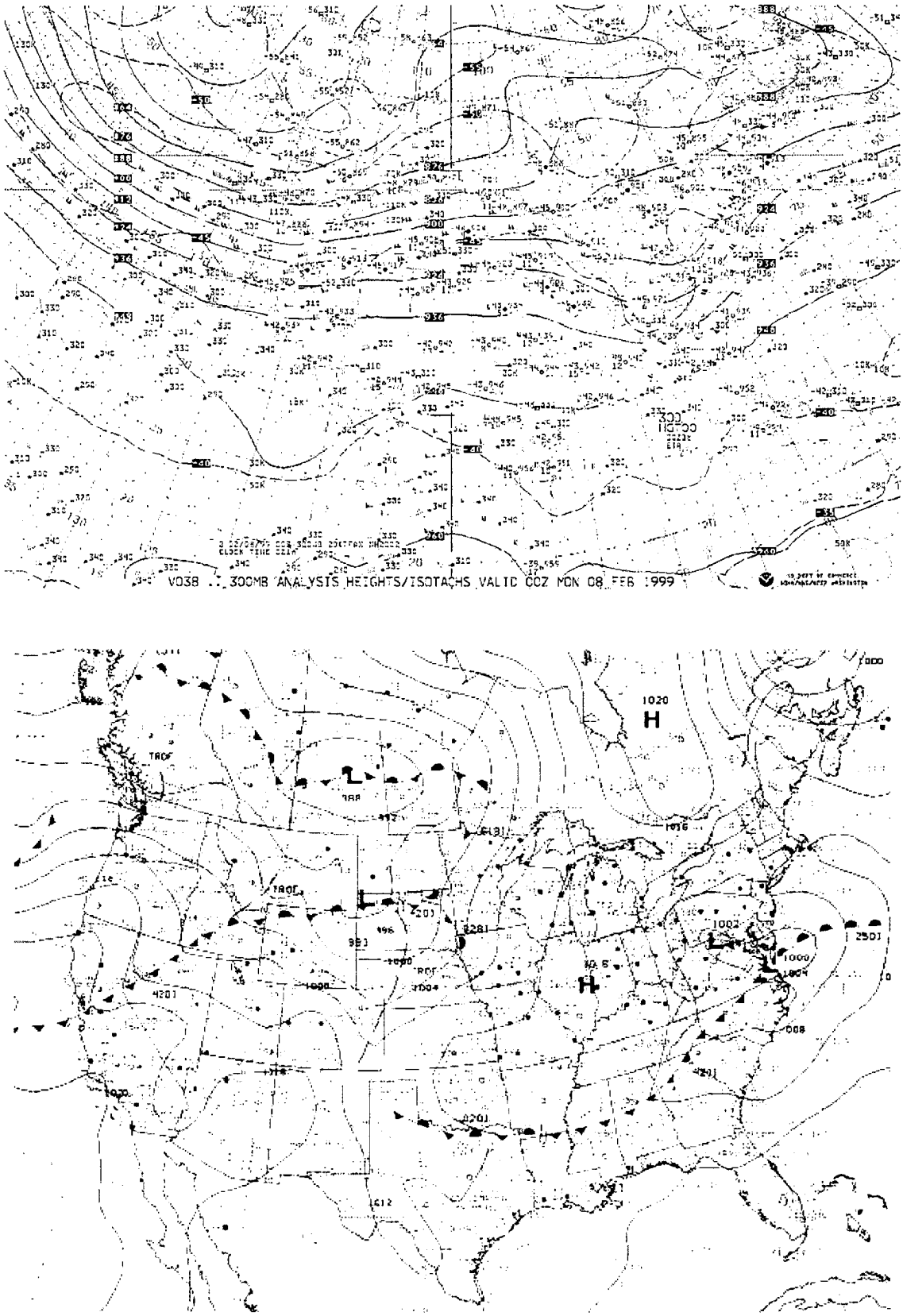

Figure 5-28: (a) Analysis of 300 hPa heights (solid lines) and isotachs (dotted lines) valid 00 UTC 8 Feb 1999. (b) Surface analysis valid 03 UTC 8 Feb 1999.

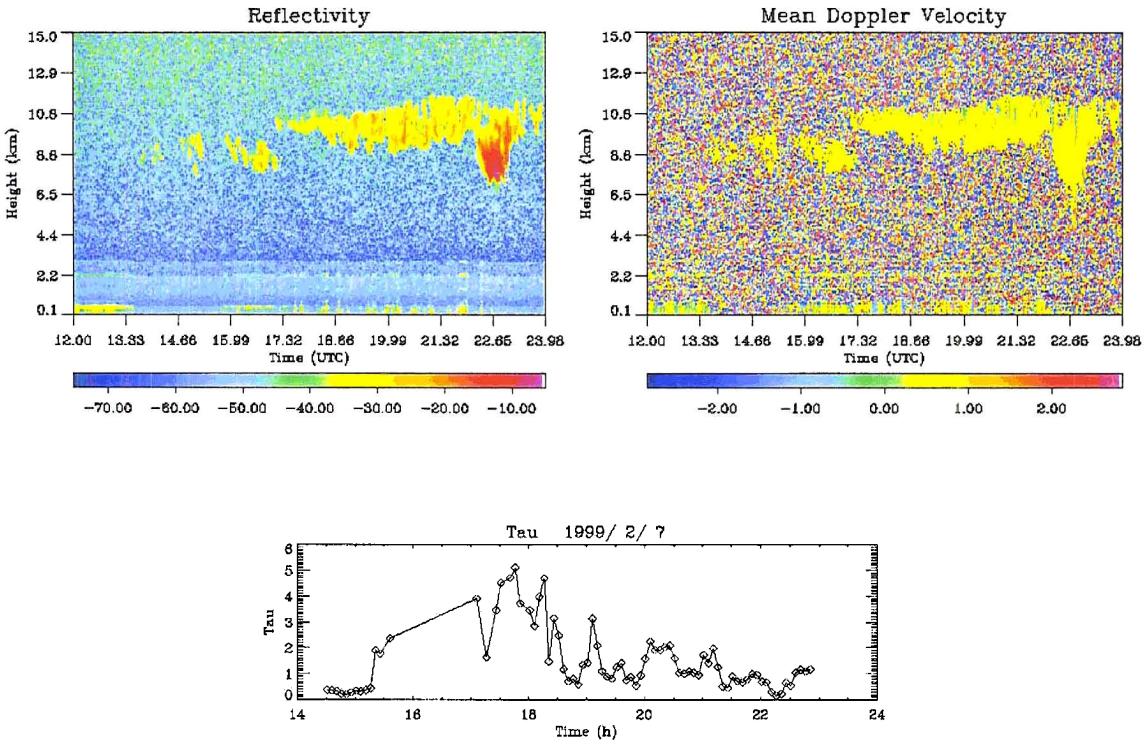

Figure 5-29: Radar reflectivity (dBZ), Doppler velocity (m s^{-1}), and estimated column optical depth. Case 7 Feb 1999.

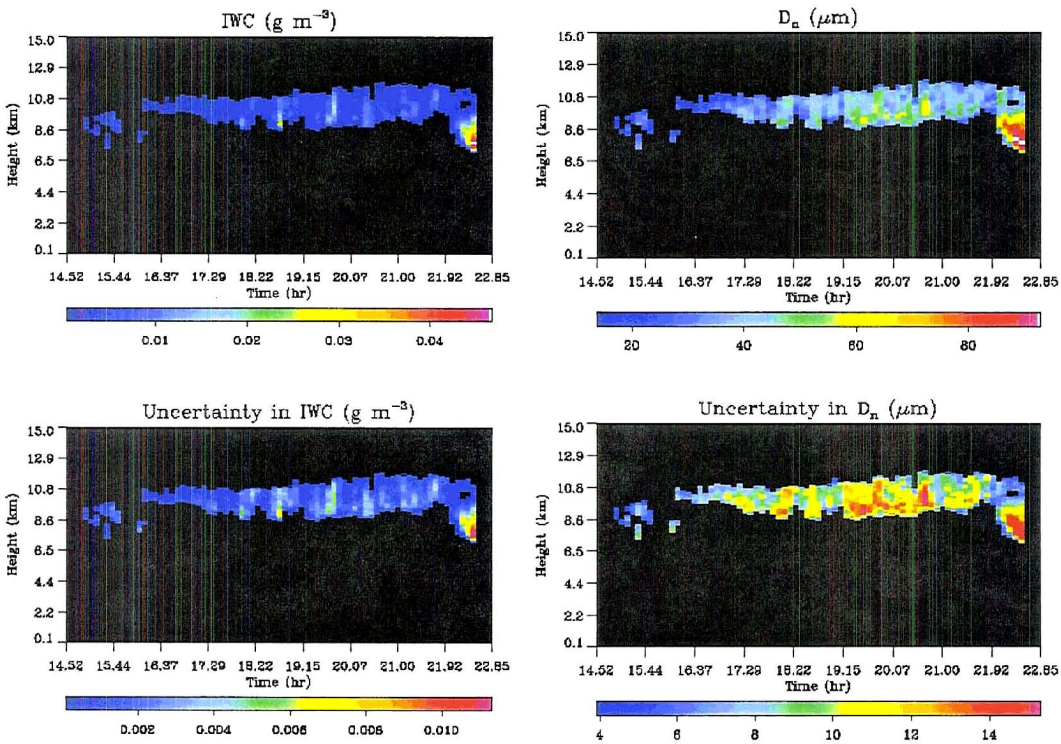

Figure 5-30: Retrieved IWC (g m^{-3}) and characteristic diameter (μm) and the associated uncertainties. Case 7 Feb 1999.

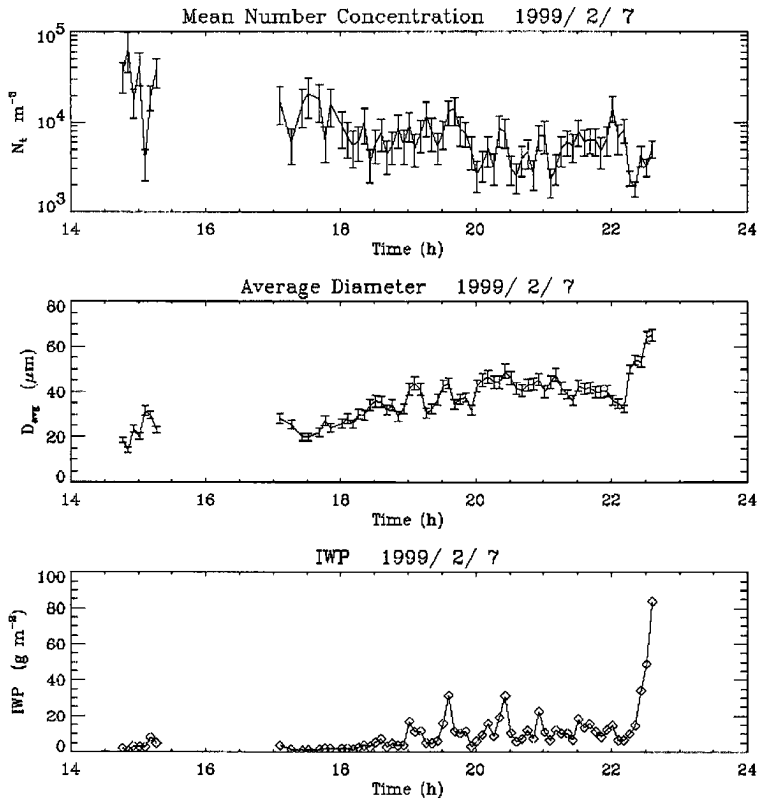

Figure 5-31: Retrieved number concentration N_t (m^{-3}), average characteristic diameter D_{avg} (μm), and column ice water path (g m^{-2}). Case 7 Feb 1999.

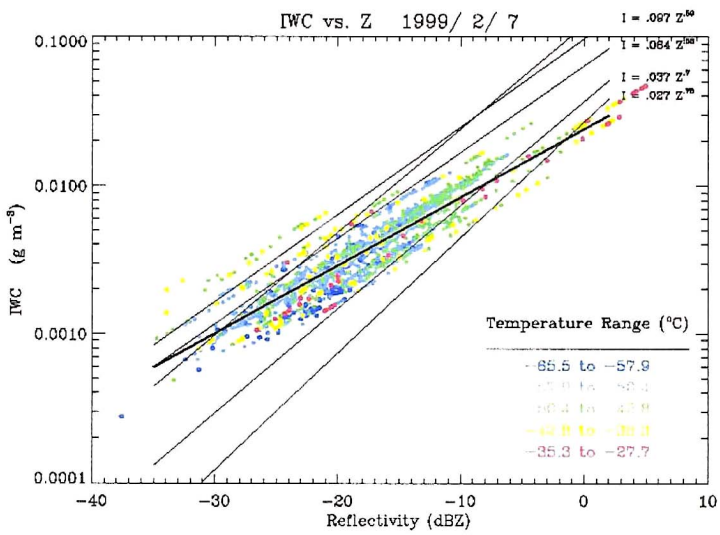

Figure 5-32: Scatter plot of ice water content (g m^{-3}) versus radar reflectivity (dBZ), color coded according to radiosonde observation of environmental temperature. A few common IWC-Z power law relations are provided for reference. Case 7 Feb 1999.

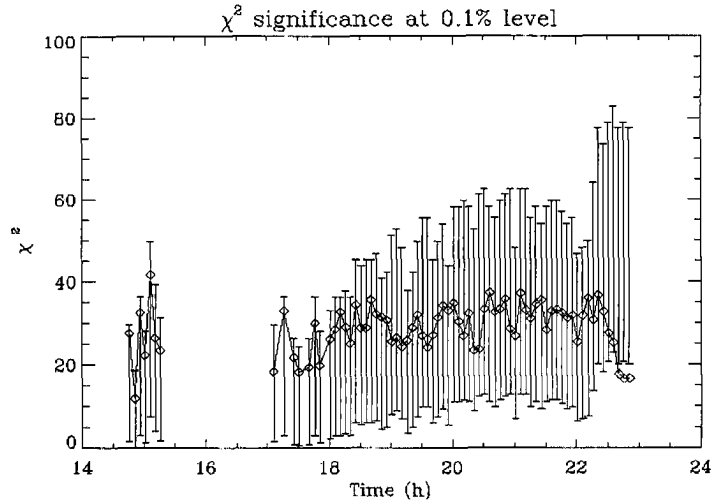

Figure 5-33: Chi-squared value of the retrieval (points and solid line). The bars show the maximum and minimum value of chi-squared that would be allowable for a "quality" retrieval at the 0.1% level given the degrees of freedom of each profile. Points that lie outside the bars are rejected by the retrieval. Case 7 Feb 1999.

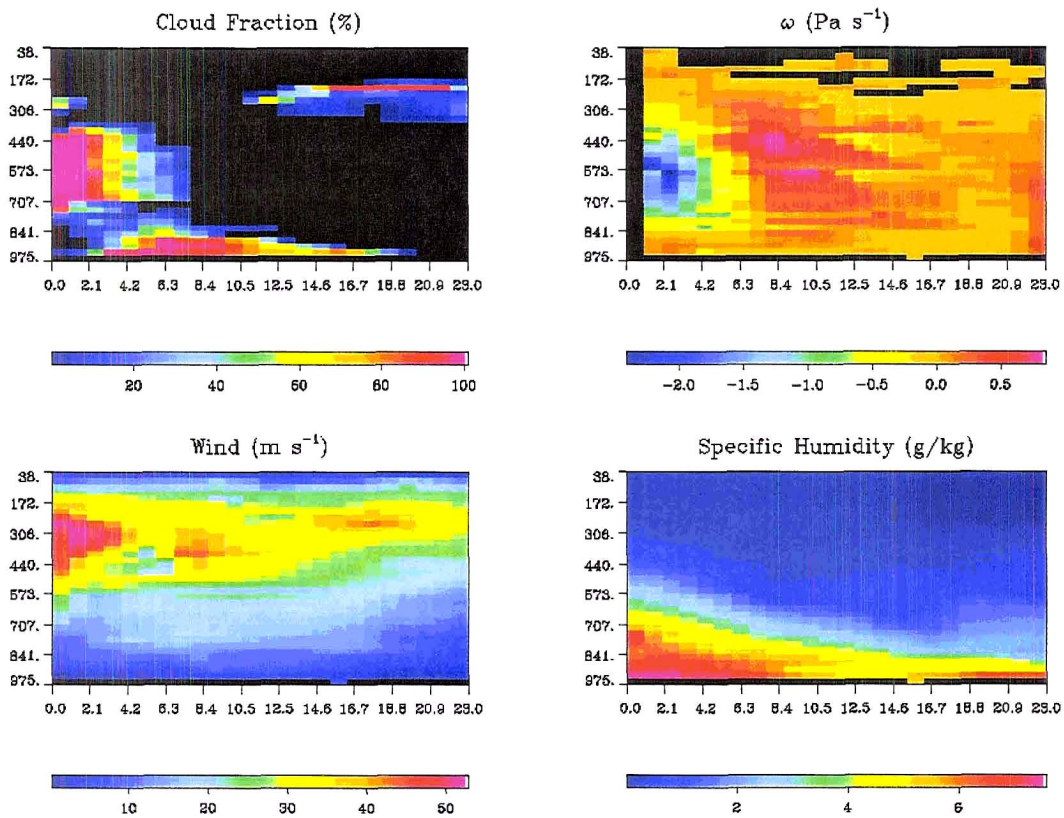

Figure 5-34: EDAS output for 7 Feb 1999. Clockwise from upper left: cloud fraction, omega (Pa s^{-1}), specific humidity (g kg^{-1}), wind speed (m s^{-1}).

ETA/EDAS 18 UTC 1999/02/07

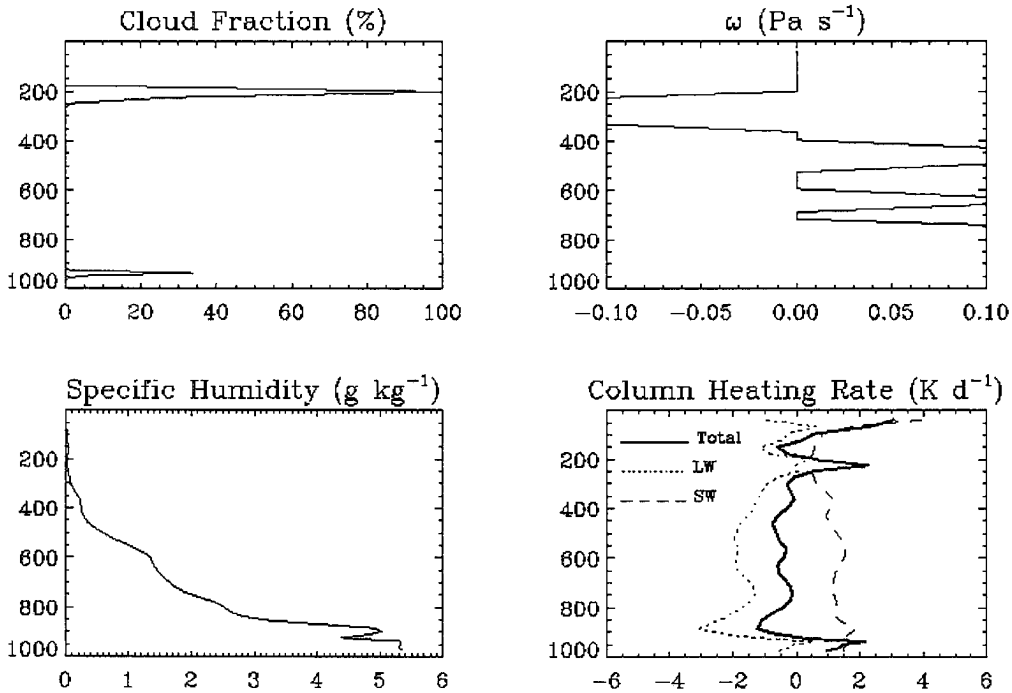

Figure 5-35: EDAS vertical profiles of cloud fraction, omega (Pa s^{-1}), and column radiative heating rate (K day^{-1}), for 18 UTC. Case 7 Feb 1999.

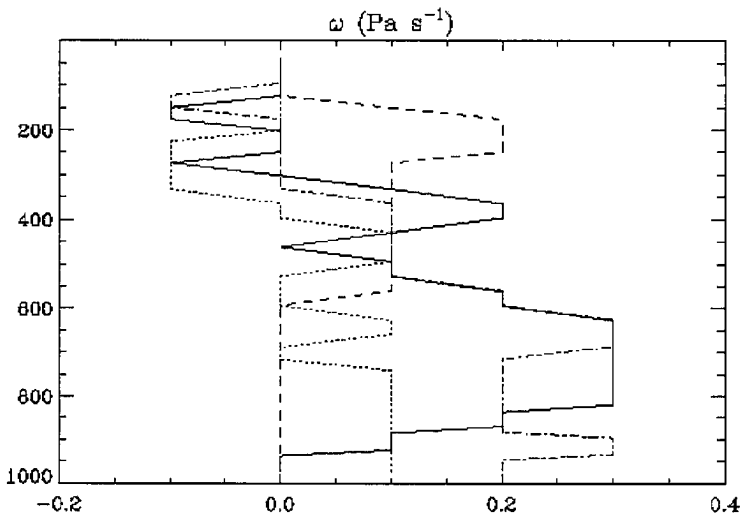

Figure 5-36: EDAS vertical motion profiles for 16 (solid line), 18 (dotted line), 21 (dashed line), and 23 UTC (dot-dash line) on 7 Feb 1999.

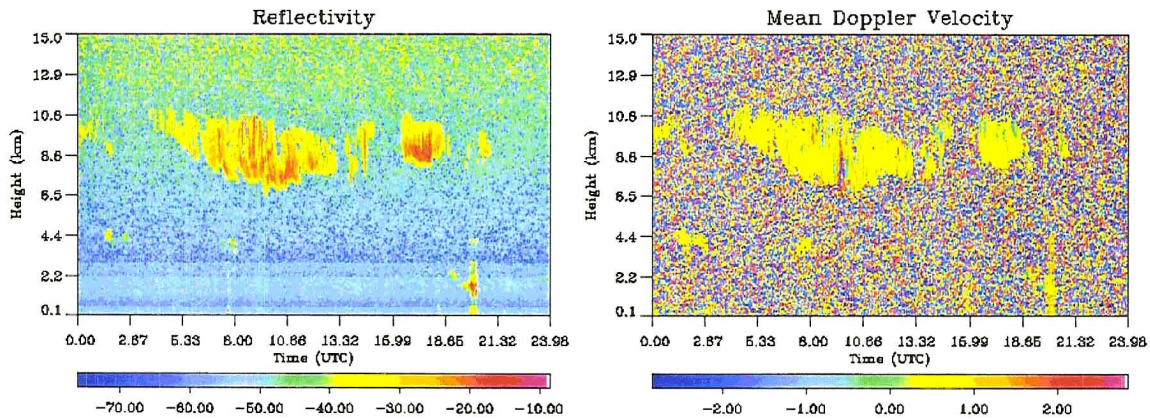

Figure 5-37: Radar reflectivity (dBZ) and Doppler velocity (m s^{-1}). Case 13 Nov 1998.

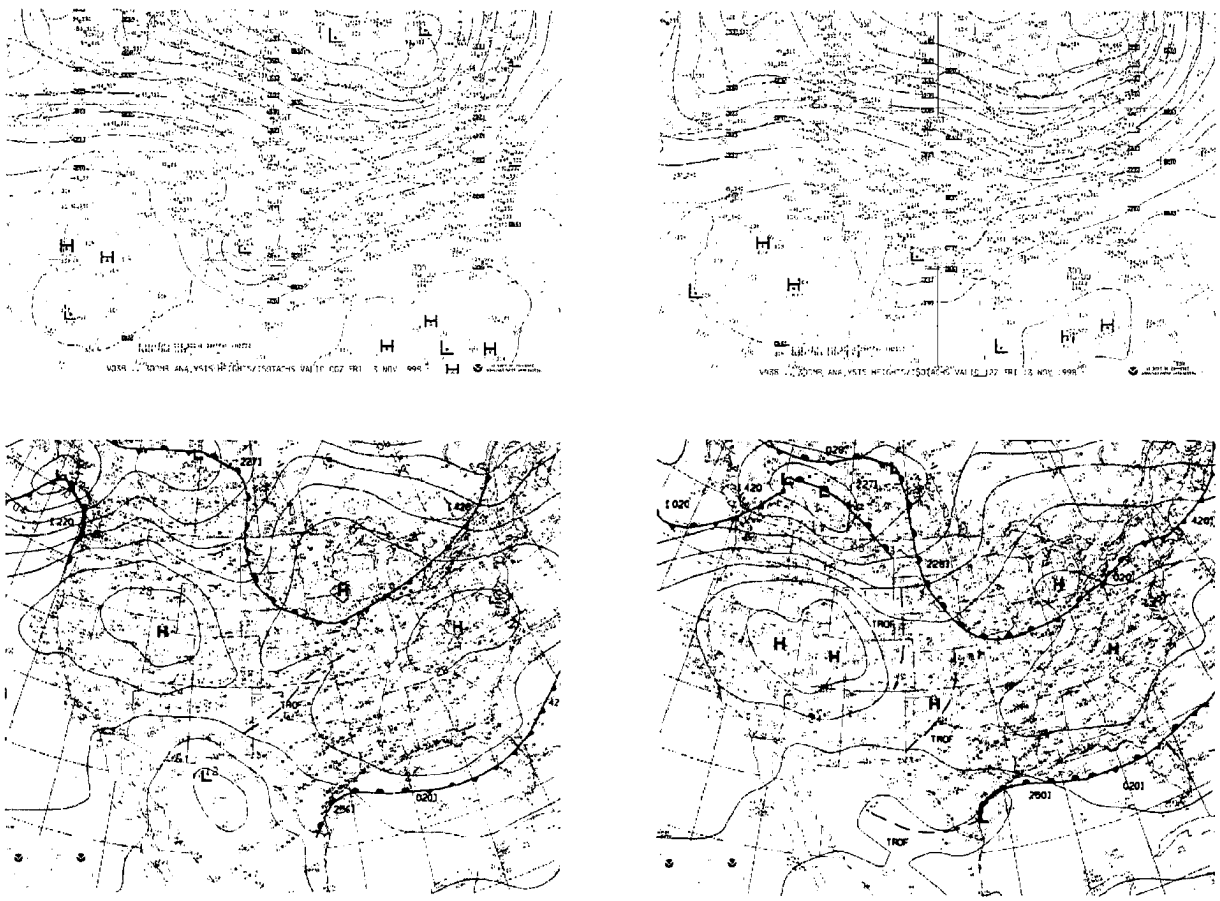

Figure 5-38: TOP: Analysis of 300 hPa heights (solid lines) and isotachs (dotted lines) valid 00 UTC (left), and 12 UTC (right) on 13 Nov 1998. BOTTOM: Surface analysis valid 00 UTC (left), and 12 UTC (right).

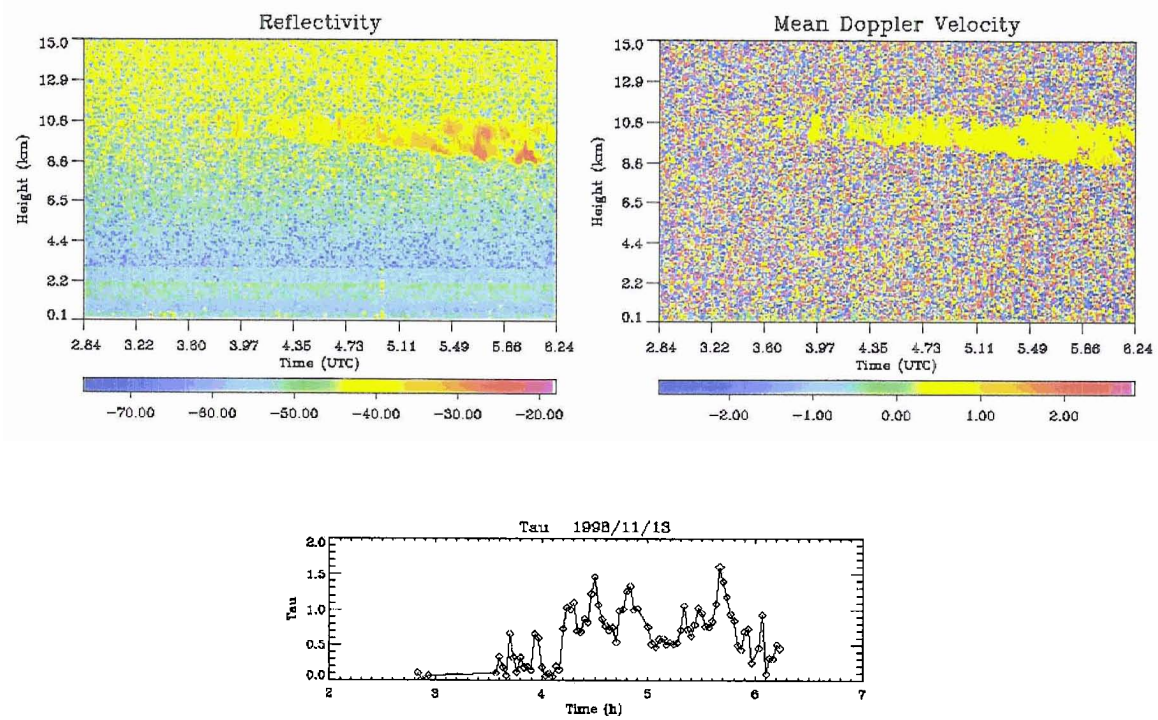

Figure 5-39: Radar reflectivity (dBZ), Doppler velocity (m s^{-1}), and estimated column optical depth. Part I, 13 Nov 1998.

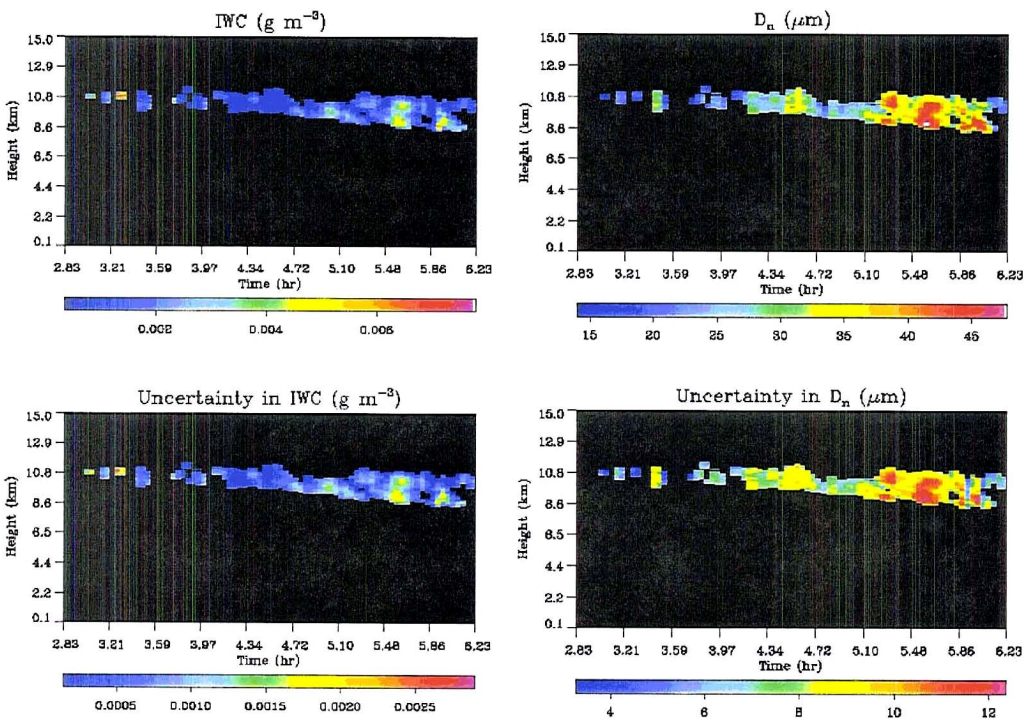

Figure 5-40: Retrieved IWC (g m^{-3}) and characteristic diameter (μm) and the associated uncertainties. Part I, 13 Nov 1998.

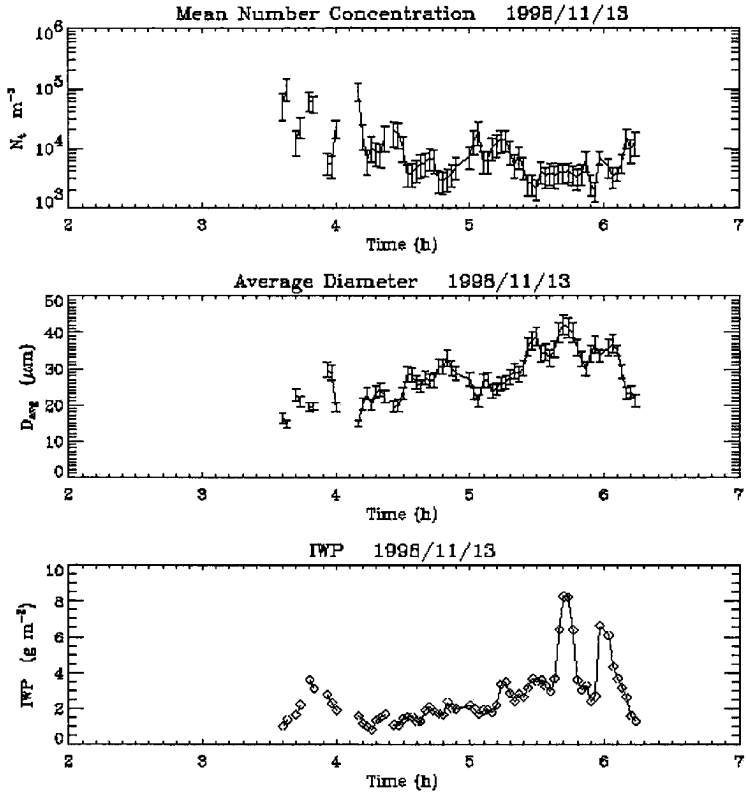

Figure 5-41: Retrieved number concentration N_t (m^{-3}), average characteristic diameter D_{avg} (μm), and column ice water path (g m^{-2}). Part I, 13 Nov 1998.

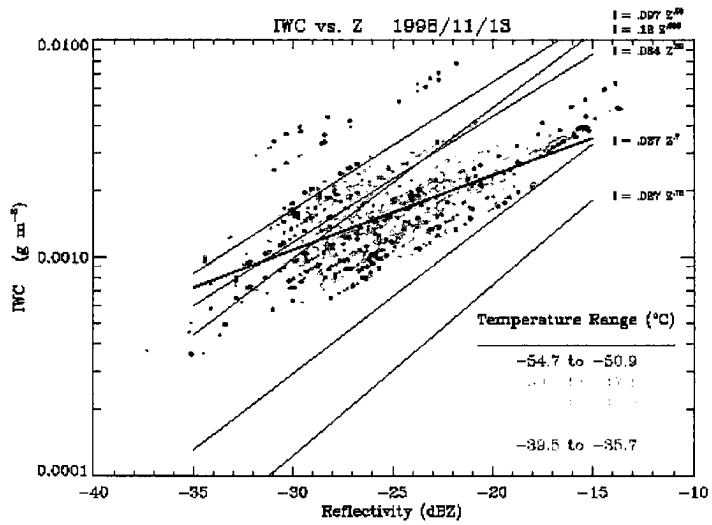

Figure 5-42: Scatter plot of ice water content (g m^{-3}) versus radar reflectivity (dBZ), color coded according to radiosonde observation of environmental temperature. A few common IWC-Z power law relations are provided for reference. Part I, 13 Nov 1998.

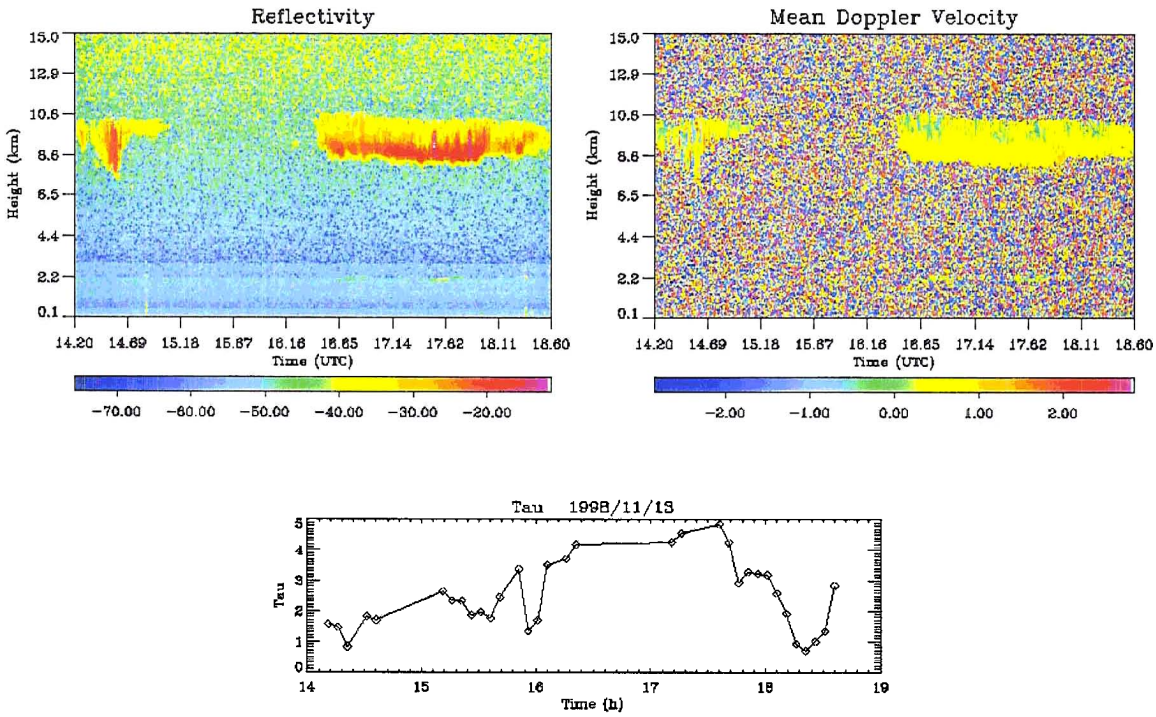

Figure 5-43: As in Figure 5-39, but for Part II, 13 Nov 1998.

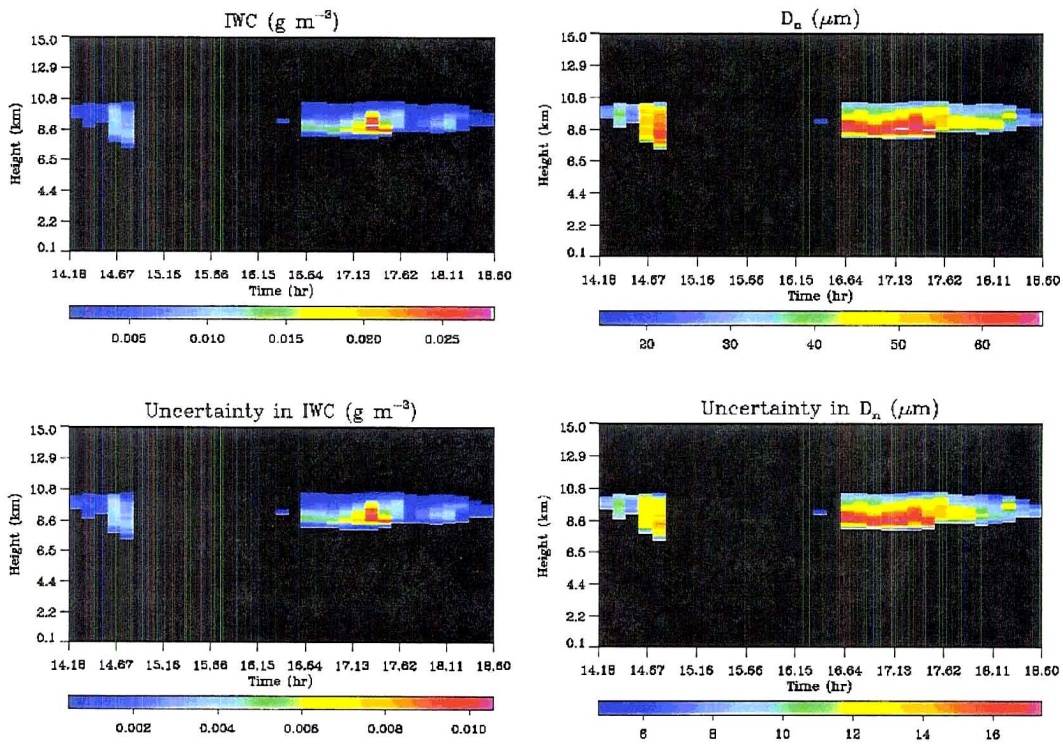

Figure 5-44: As in Figure 5-40, but for Part II, 13 Nov 1998.

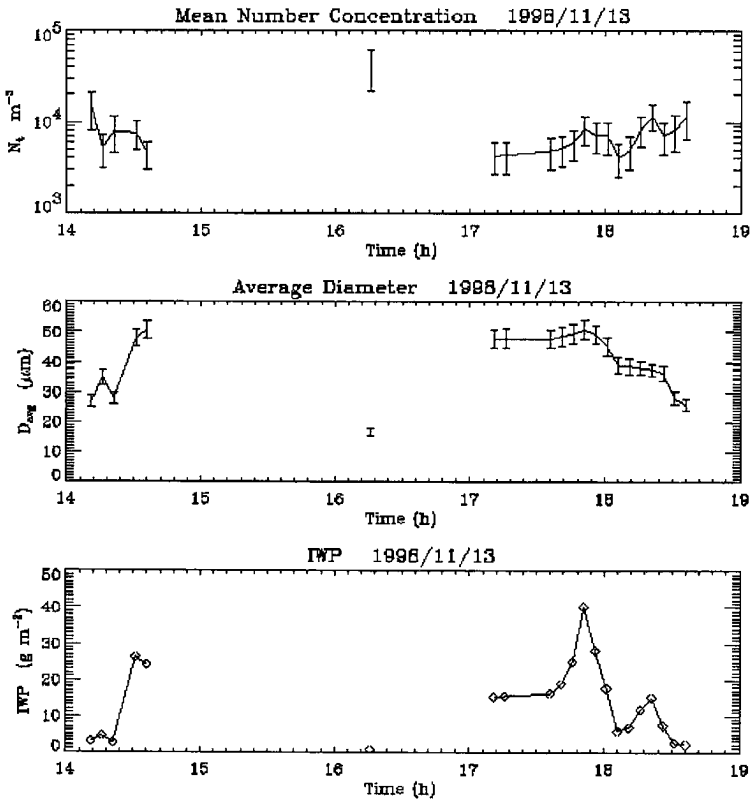

Figure 5-45: As in Figure 5-41, but for Part II, 13 Nov 1998.

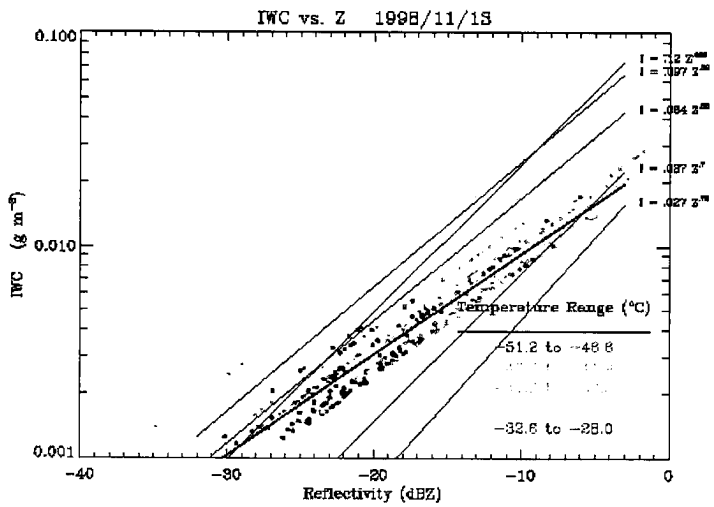

Figure 5-46: As in Figure 5-42, but for Part II, 13 Nov 1998.

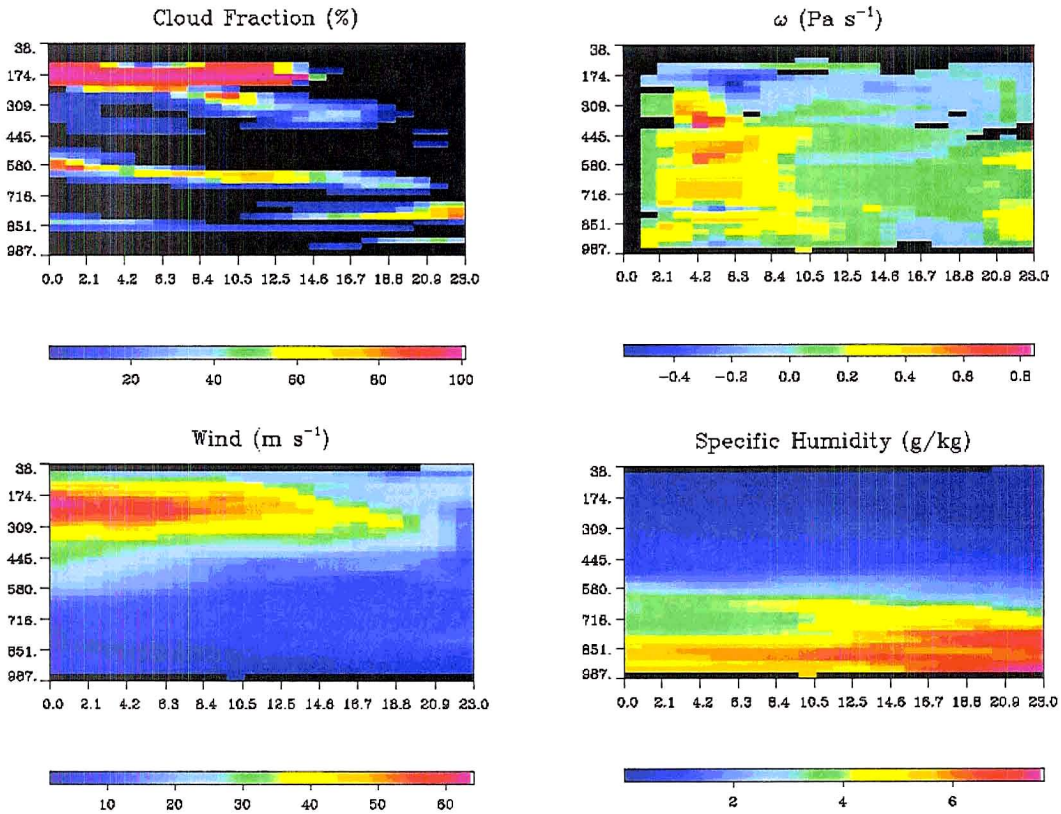

Figure 5-47: EDAS output for 13 Nov 1998. Clockwise from upper left: cloud fraction, omega (Pa s^{-1}), specific humidity (g kg^{-1}), wind speed (m s^{-1}).

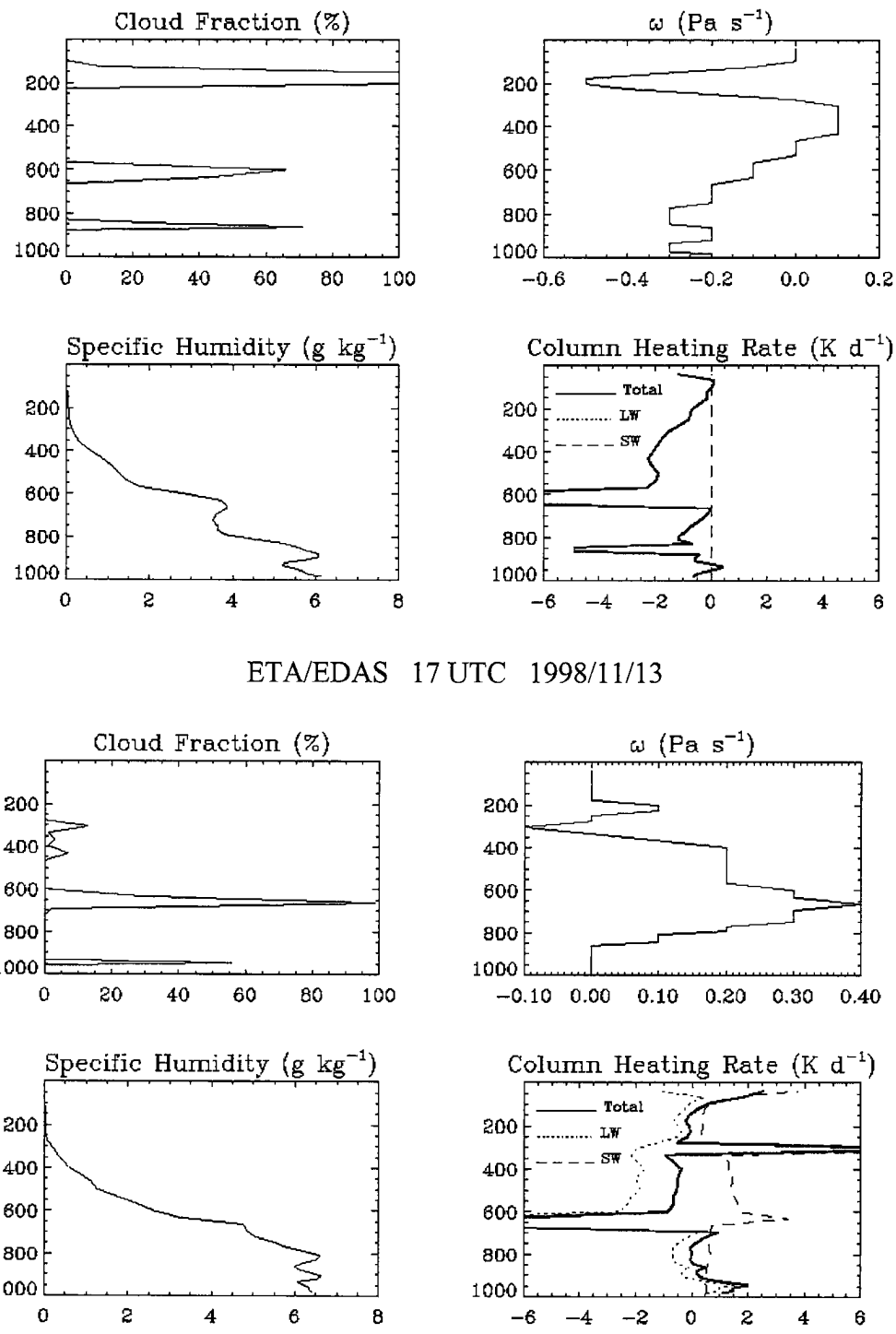

Figure 5-48: EDAS vertical profiles of cloud fraction, omega (Pa s^{-1}), and column radiative heating rate (K day^{-1}), for 05 UTC (top) and 17 UTC (bottom). Case 13 Nov 1998.

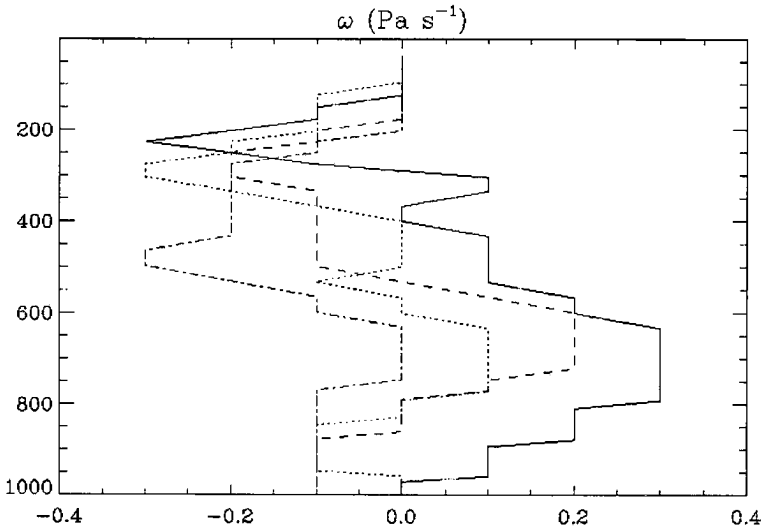

Figure 5-49: EDAS vertical motion profiles for 14 (solid line), 16 (dotted line), 18 (dashed line), and 20 UTC (dot-dash line) on 13 Nov 1998.

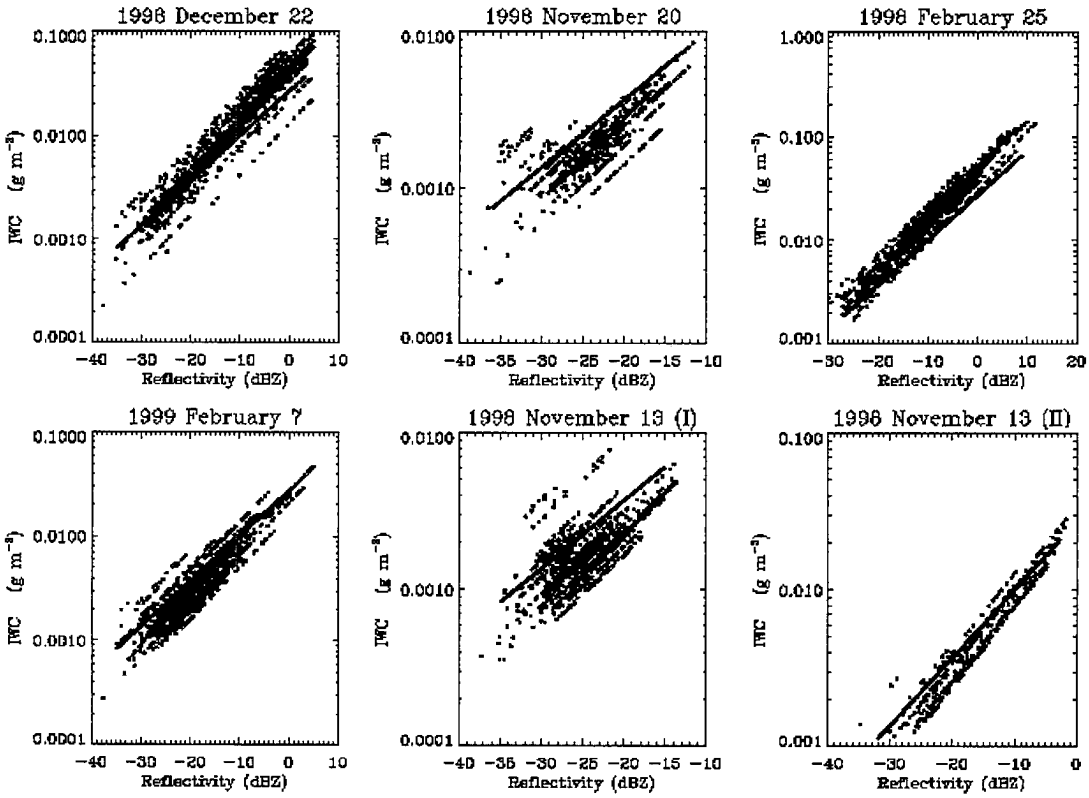

Figure 5-50: Ice water content (g m^{-3}) versus radar reflectivity (dBZ) for all six cases. The new, suggested regression line is plotted over each.

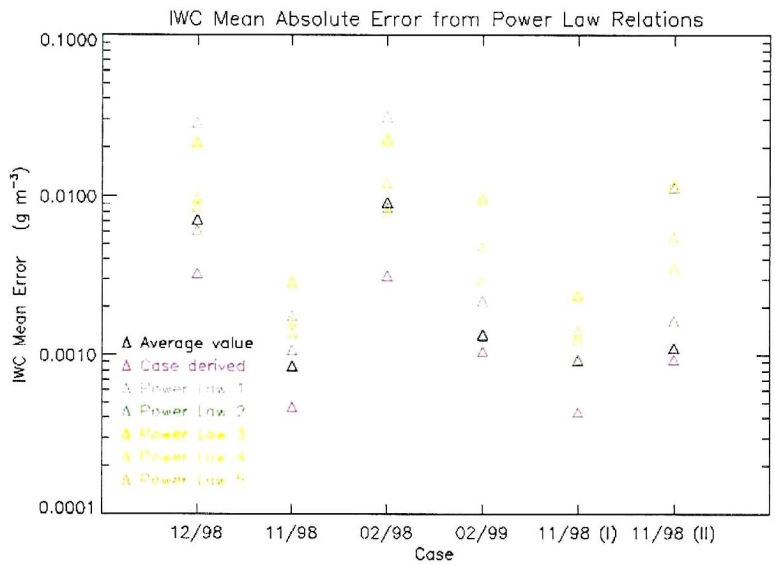

Figure 5-51: Mean absolute departure of power law derived IWC from the retrieved IWC. The five power law relations defined in Table 3-1 are shown in addition to the case-derived and the new, average power law regression.

This page intentionally blank.

Chapter 6

6. SUMMARY AND CONCLUSIONS

6.1 Conclusions

The purpose of this study was to examine the relationship between dynamically forced cirrus clouds and the jet stream structure which led to their existence, as well as to learn something of the microphysical content of these clouds using a relatively new retrieval scheme. This chapter will summarize the key findings of this study, outline the questions that remain unanswered, and look forward to what is needed to gain a better understanding of these clouds.

The composite study is based on fourteen cases with strong southwesterly winter-time jet streams, and was performed with respect to the location of the 300 hPa maximum wind in these cases. The composite dynamical fields have a structure that are, to first order, consistent with the known structure of strong wintertime mid-latitude cyclones. For example, 700 hPa vertical motion is maximized in the right-entrance region and left-exit region of the jet stream, as is observed in real system due to the ageostrophic motions within accelerating and decelerating regions of the jet. Positive vorticity advection at 500 hPa is correctly positioned. A surface front is evident in both the 1000 hPa thermal

advection and height fields. Furthermore, three vertical cross sections through the jet reveal vertical motion in appropriate positions and of realistic magnitudes, and also show the westward tilt of the system with height that is required by hydrostatic balance.

The ISCCP-derived cloud structure of the composite is also reasonable, although there are some discrepancies caused by the different radiative assumptions that were employed to derive fields like cloud-top temperature and pressure. Analysis of the location of the highest, coldest, and thinnest clouds shows a large area of cirrus in the accelerating, or entrance region, of the jet streak. This area was split between the right and left portions of the entrance region, without about one-third to the right and two-thirds to the left. Another concentrated region of cirrus is located in the comma cloud region of the system, and to its southeast are found somewhat thicker clouds very near the axis of the jet. This region of thicker clouds exhibits the often-observed tendency for a sharp boundary to form between the northern extent of the clouds and the axis of maximum wind of the jet stream. More spotty areas of cirrus are located in the warm air in the southeast portion of the system.

In many ways, the composite results are fairly consistent with the findings of Menzel et al. (1992). For example, both studies show the largest cirrus fraction in the accelerating region of the jet. However, the distribution within this region differs from Menzel et al.; in the composite, more cirrus are located in the left-entrance region than the right-entrance region. This in contrary to the composite large-scale vertical motion fields resolved by the model, as is discussed further below.

The microphysical properties of these clouds, as derived from the tau-Z retrieval, are well summarized in Table 5-7, and will not be repeated here. Variability on the order

of two orders of magnitude is evident in parameters like particle number concentration, mean diameter, and ice water content of the cloud. Some of the clouds are particularly tenuous, with optical depths on the order of only one or two, and column ice water path less than 5 g m^{-2}. Others have optical depths as high as four to five, and mean ice water paths on the order of 30 to 50 g m^{-2}. These properties vary greatly over a few hours, often maximizing in short peaks of observed maxima of radar reflectivity.

The uncertainties in these microphysical parameters are characterized by the retrieval algorithm. Uncertainties in ice water content are on the order of 25 to 45%, while uncertainties in ice crystal effective radius are often much less, around 10 to 20%. However, the vertically integrated ice water content, as demonstrated by model cloud simulations, is associated with an uncertainty of only a few percent. These uncertainties are probably strongly related to the assumption that ice crystal number concentration is constant with height, and this explains why height-integrated quantities are more certain than the individual gate-to-gate value of these quantities. Upcoming field campaigns, such as CRYSTAL-FACE to take place in Florida in the summer of 2002, will present a welcome opportunity to validate the retrieval results again in-situ cirrus observations.

The relation of these parameters to the dynamics that support these clouds was of particular interest in the development of this study. As was noted throughout the case studies, the cirrus were associated with relatively small synoptic-scale vertical velocities. The case study absolute mean vertical velocities vary from 0.003 to 0.212 Pa s^{-1}; two of these case mean velocities are descending and three are ascending. The dynamical composite shows the largest area of cirrus, in the entrance region of the jet streak, associated with cloud-level vertical motions on the order of 0 to 0.05 Pa s^{-1}. The zero

vertical motion line lies more or less along the jet stream axis, with a westward extension in the south, and split the area of cirrus into a weak ascending region and a weak descending region. No relationship is noted between the sign of vertical motion and the characteristic drop size or concentration.

These findings, again, confirm the findings of previous studies: jet stream cirrus clouds may be supported by large-scale lift associated with dynamics of the jet, but these motions are very weak and difficult to resolve in numerical weather prediction models. The motions are so weak that they are very similar to the motions that dissipate the clouds (Wylie, 2002). In this respect, the vertical resolution of the EDAS model may be preferential to that of the ECMWF reanalysis; at this time, the vertical resolution of the former is about 30 hPa while the latter is 100 hPa. Indeed, the EDAS often showed weak ascent present at cloud level during at least one of the one-hour time steps when clouds were present in every case, but it seems that the very small changes in vertical velocity (or upper-level humidity) that contribute to observed minima and maxima in cloud properties remain unresolved. The results indicate that processes other than large-scale uplift, such as horizontal moisture advection, may also play a significant role in the development of these clouds.

The importance of capturing these dynamical processes in models is critical; the radiative properties of these cirrus depend on the microphysics, and the microphysics in turn depend on, amongst other things, the strength of the dynamical fields that contribute to their growth. Inability to capture these processes will have an impact on the radiative budgets in numerical weather and climate models, in turn affecting other processes, such as the hydrologic cycle, as well.

Some of the key findings of this study are summarized by the schematic diagram of Figure 6-1. The jet is outlined by the dotted black line, represented by the position of the 35 m s^{-1} isotach in the composite. The jet axis, as well as the accelerating and decelerating regions of the jet, are shown by the solid lines. The hatched areas represent areas where significant cirrus coverage was detected, divided into areas with Method 2 optical depths less than or equal to 15, greater than 15, and regions of sporadic cirrus coverage. The estimated positions of the six cases within this composite structure are shown by the letters, and the sign of mean cloud-level vertical motion for each case study is given by the arrow following each letter.

As the figure shows, four of the six cases were located in the jet streak entrance region, and the remaining two were located in the exit region. The mean vertical velocities indicated by the arrows are not meant to indicate any general pattern of vertical motion relative to the jet, but rather show that the sign of the vertical motion is indeed highly variable and can not be simply characterized according to the synoptic scale vertical motion.

The findings of this study indicate that further work is needed in the field of characterization of cirrus in relation to the dynamical fields, both in the areas of observation and modeling. Better observations of these clouds, particularly in-situ observations of microphysical and dynamics variables, will lead to a better understanding of the dynamics that support them, their radiative properties and impact on other parts of the earth system, and how numerical models can more accurately predict their formation, spatial coverage, and content.

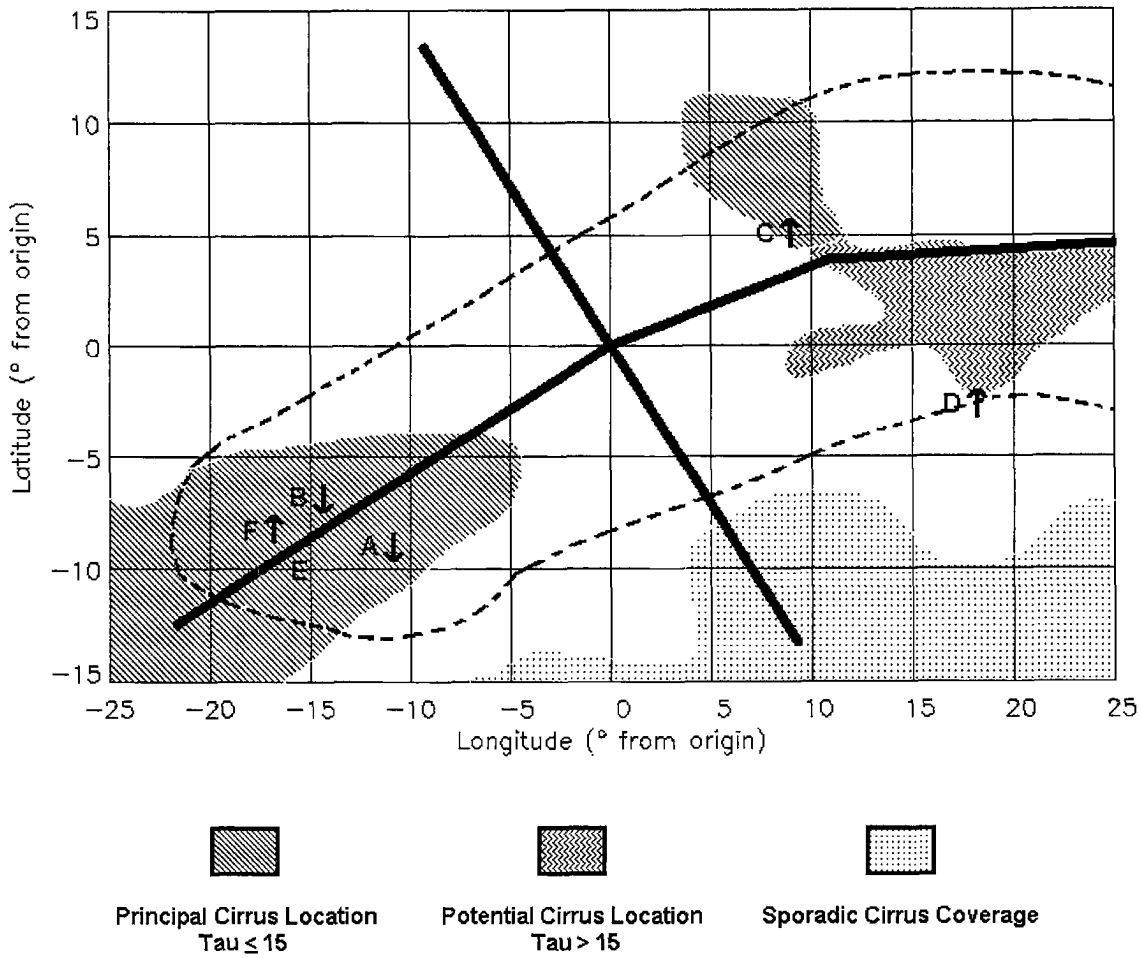

Figure 6-1: Schematic summary of principle findings. Approximate locations of cirrus in the composite are given by hatched areas, as defined by key above. Dotted line represents 35 m s^{-1} isotach in composite. Solid lines show approximate location of jet axis and division between accelerating and decelerating regions. The approximate location of each of the cases in the jet structure is shown by letter, followed by an arrow showing mean cloud-level vertical motion. A – 1998 Dec 22, B – 1998 Nov 20, C – 1998 Feb 25, D – 1999 Feb 27, E – 1998 Nov 13 (I), F – 1998 Nov 13 (II)

REFERENCES

Atlas, D., S.Y. Mastrosov, A.J. Heymsfield, M. Chou, and D.B. Wolff, 1995: Radar and radiation properties of ice clouds. *Journal of Applied Meteorology*, **34**, 2329-2345.

Bohren, C., and D.R. Huffman, 1983: Absorption and scattering of light by small particles. New York: John Wiley & Sons, Inc.

Carlson, T.N., 1980: Airflow through midlatitude cyclones and the comma cloud pattern. *Monthly Weather Review*, **108**, 1498-1509.

Ciesielski, P.E., D.E. Stephens, and R.H. Johnson, 1989: Observational evidence for asymmetric inertial instability. *Journal of the Atmospheric Sciences*, **46**, 817-831.

Clothiaux, E.E., K.P. Moran, B.E. Martner, T.P. Ackerman, G.G. Mace, T. Uttal, J.H. Mather, K.B. Widener, M.A. Miller, and D.J. Rodriguez, 1999: The Atmospheric Radiation Measurement Program cloud radars: Operational modes. *Journal of Atmospheric and Oceanic Technology*, **16**, 819-827.

Clothiaux, E.E., T.P. Ackerman, G.G. Mace, K.P. Moran, R.T. Marchand, M.A. Miller, and B.E. Martner, 2000: Objective determination of cloud heights and radar reflectivities using a combination of active remote sensors at the ARM CART sites. *Journal of Applied Meteorology*, **39**, 645-665.

Clothiaux, E.E., M.A. Miller, R.C. Perez, D.D. Turner, K.P. Moran, B.E. Martner,T.P. Ackerman, G.G. Mace, R.T. Marchand, K.B. Widener, D.J. Rodriguez, T. Uttal, J.H. Mather, C.J. Flynn, K.L. Gaustad, B. Ermold: 2001. The ARM Millimeter-

Wave Cloud Radar (MMCRs) and the Active Remote Sensing of Clouds (ARSCL) value added product (VAP). *DOE Tech. Memo ARM VAP-002 v1.*

Dowling, D.R. and L.F. Radke: 1990. A summary of the physical properties of cirrus clouds, *Journal of Applied Meteorology*, **29**, 970-978.

Durran, D.R. and D.B. Weber: 1988. An investigation of the poleward edges of cirrus clouds associated with midlatitude jet streams. *Monthly Weather Review*, **116**, 702-714.

Fritsch, J.M. and R.A. Maddox: 1981. Convectively driven mesoscale systems aloft, Pt. 1, Observations. *Journal of Applied Meteorology*, **20**, 9-19.

Fu, Q., 1996. An accurate parameterization of the solar radiative properties of cirrus clouds for climate models. *Journal of Applied Climate*, **9**, 2058-2082.

Heymsfield, A.J., 1975: Cirrus uncinus generating cells and the evolution of cirriform clouds, Pt. 2, The structure and circulations of the cirrus uncinus generating cells. *Journal of the Atmospheric Sciences*, **32**, 809-819.

Johnson, R.H. and M.E. Nicholls, 1983. Composite analysis of the boundary layer accompanying a tropical squall line. *Monthly Weather Review*, **111**, 308-319.

Khvorostyanov, V.I. and K. Sassen, 1998. Cirrus cloud simulation using explicit microphysics and radiation. Part I: Model description. *Journal of the Atmospheric Sciences*, **55**, 1808-1821.

Lau, N., and M.W. Crane, 1995. A satellite view of the synoptic-scale organization of cloud properties in midlatitude and tropical circulation systems. *Monthly Weather Review*, **123**, 1984-2006.

Liu, Chun-Lei and A.J. Illingworth: 2000. Toward more accurate retrievals of ice water

content from radar measurements in clouds. *Journal of Applied Meteorology*, **39**, 1130-1146.

Mace, G.G., T.P. Ackerman, P. Minnis, and D.F. Young: 1998. Cirrus layer microphysical properties derived from surface-based millimeter radar and infrared Interferometer data. *Journal of Geophysical Research*, **103**, 23207-23216.

Mace, G.G., E.E. Clothiaux, and T.P. Ackerman: 2001: The composite characterization of cirrus clouds: Bulk properties revealed by one year of continuous cloud radar data. *Journal of Climate*, **14**, 2185-2203.

Marks, C.J. and C.D. Rodgers: 1993. A retrieval method for atmospheric composition from limb emission measurements. *Journal of Geophysical Research*, **98**, 14939-14953.

Matrosov, S.Y., 1999: Retrievals of vertical profiles of ice cloud microphysics from radar and IR measurements using tuned regressions between reflectivity and cloud parameters. *Journal of Geophysical Research*, **104**, 16741-16753.

Menzel, W.P., D.P. Wylie, and K.I. Strabala, 1992. Seasonal and diurnal changes in cirrus clouds as seen in four years of observations with the VAS. *Journal of Applied Meteorology*, **31**, 370-385.

Mudukutore, A.S., V. Chandrasekar, and R.J. Keeler: 1998. Pulse compression for weather radars. *IEEE Transactions on Geoscience and Remote Sensing*, **36**, 125-142.

Newman, M., P.D. Sardeshmukh, and J.W. Bergmen: 2000. An assessment of the NCEP, NASA, and ECMWF reanalyses over the tropical west Pacific warm pool. *Bulletin of the American Meteorological Society*, **81**, 41-48.

Rodgers, C.D.: 1976. Retrieval of atmospheric temperature and composition from remote measurements of thermal radiation. *Reviews of Geophysical and Space Physics*, **14**, 609-624.

Rodgers, C.D.: 1990. Characterization and error analysis of profiles retrieved from remote sounding measurements. *Journal of Geophysical Research*, **95**, 5578-5595.

Rogers, E., T.L. Black, D.G. Deaven, and G.J. DeMego: 1996. Changes to the operational "early" ETA analysis/forecast system at the National Centers for Environmental Prediction. *Weather and Forecasting*, **11**, 391-413.

Rossow, W.B., A.W. Walker, D.E. Beuschel, and M.D. Roiter, International Cloud Climatology Project Project: Documentation of new datasets. 1996.

Sassen, K.: 1987. Ice cloud content from radar reflectivity. *Journal of Climate and Applied Meteorology*, **26**, 1050-1053.

Sassen, K. and L. Liao: 1996. Estimation of cloud content by W-band radar. *Journal of Applied Meteorology*, **35**, 932-938.

Sassen, K., Z. Walker, V.I. Khvorostyanov, G.L. Stephens and A. Bennedetti: 2001. Cirrus cloud ice water content radar algorithm evaluation using an explicit cloud microphysical model. *To be submitted.*

Stephens, G.L., 1983: The influence of radiative transfer on the mass and heat budgets of ice crystals falling in the atmosphere. *Journal of the Atmospheric Sciences*, **40**, 1729-1739.

Stephens, G.L., 1994: Remote sensing of the lower atmosphere. New York: Oxford University Press, 523 pp.

Tripoli, G.J., P.J. Flatau, and W.R. Cotton, 1988: Generalized microphysics scheme for use in mesoscale/cloud models. *Annalen der Meteorologie*, **1**, 109-111.

Uccellini, L.W. and D.R. Johnson, 1979: The coupling of upper and lower tropospheric jet streaks and implications for the development of severe convective systems. *Monthly Weather Review*, **107**, 682-703.

Wu, T., W.R. Cotton, and W.Y.Y. Cheng, 1999: Radiative effects on the diffusional growth of ice particles in cirrus clouds. *Journal of the American Meteorological Society*, **57**, 2892-2904.

Wylie, D., 2002: Cirrus and weather: A satellite prospective, in *Cirrus*. Lynch, D.K., K. Sassen, D. Starr, G. Stephens, 2002 (Eds). New York: Oxford University Press, 480 pp.

Yang, P., K.N. Liou, K.Wyser, and D. Mitchell, 2000: Parameterization of the scattering and absorption properties of individual ice crystals. *Journal of Geophysical Resources*, **105**, 4699-4718.

Young, K.C., 1993: Microphysical processes in clouds. New York: Oxford University Press, 427 pp.

Zapotocny, T.H., S.J. Nieman, W.P. Menzel, J.P. Nelson III, J.A. Jung, E. Rogers, D.F. Parrish, G.J. DiMego, M. Baldwin, and T.J. Schmit: 2000. A case study of the sensitivity of the ETA data assimilation system. *Weather and Forecasting*, **15**, 603-621.